



**Max-Planck-Institut für Metallforschung
Stuttgart**

Wet Chemical Synthesis and Characterization of Organic/TiO₂ Multilayers

Aleksandar Tucić

Dissertation
an der
Universität Stuttgart

Bericht Nr. 212
Januar 2008

Wet Chemical Synthesis and Characterization of Organic/TiO₂ Multilayers

Dissertation

Von der Fakultät Chemie der Universität Stuttgart

zur Erlangung der Würde eines

Doktors der Naturwissenschaften (Dr. rer. nat.)

genehmigte Abhandlung

Vorgelegt von

Aleksandar Tucić

Aus Belgrad, Serbien

Hauptberichter : Prof. Dr. rer. nat. Fritz Aldinger

Mitberichter : Priv.-Doz. Dr. rer. nat. Joachim Bill

Tag der mündlichen Prüfung : 09.01.2008

Institut für Nichtmetallische Anorganische Materialien der Universität Stuttgart

Max-Planck-Institut für Metallforschung, Stuttgart

Pulvermetallurgisches Laboratorium

2008

Acknowledgements

In the following, I would like to thank the people who contributed to the completion of this work:

My supervisor, Prof. Dr. Fritz Aldinger, for giving me the opportunity to work in PML, his guidance and his confidence in the forthcoming of this thesis.

Priv.-Doz. Dr. Joachim Bill, my group-leader and 'Mitberichter', who introduced me to the topic of Bioinspired Materials, for providing me a lot of help during the work and discussion of results, and patience in reading and correcting of the manuscript.

Prof. Dr. Eric J. Mittemeijer for taking over the 'Prüfungsvorsitzender' for my final examination.

I am also grateful to:

Dr. Rudolf Hoffmann for his numerous helpful suggestions during the experimental work, for a lot of scientific discussions which we had and final critical reading of the proof-manuscript.

Dr. Žaklina Burghard for implementing and performing of nanoindentation measurements, discussion of results and reading the manuscript concerning the chapter of mechanical properties.

Dr. Vesna Šrot for STEM and Dr. Paul Bellina for HRTEM investigations, as well the interpretation of results.

Dr. L. Jeurgens and B. Siegle for support in AES investigations.

Dr. L. Pitta-Bauermann for performing QCM measurements and discussion of results.

J. Bartholome and P. Gerstel for precious help in laboratory work.

H. Labitzky and S. Künemann for assistance in SEM investigations.

Dr. P. Lampeter and Dr. U. Wezel for assistance in XRD.

M. Kelsch and U. Eigenthaler for support in FIB preparation of TEM specimens.

All members of PML for providing friendly working atmosphere, many beneficial work and support in solving all kind of problems.

All my friends from MPI and Stuttgart who made my social life in Germany pleasant and enjoyable.

Finally, my special thanks to Dr. Hans-Georg Libuda, not only for organizing and coordinating the IMPRS-AM, but also for his precious help, understanding, support and friendship during my stay in MPI.

Table of contents

Abstract	1
Zusammenfassung	6
1. Introduction	11
2. Literature overview	14
2.1. Biomineralization and bio-inspired processing	14
2.2. Wet chemical processing.....	21
2.3. Deposition of oxide films	22
2.4. Deposition of TiO ₂ thin films	24
2.5. Layer-by-layer deposition of polyelectrolytes.....	25
3. Experimental methods	28
3.1. Film deposition	28
3.1.1. Substrate preparation	28
3.1.2. Deposition of polyelectrolyte layers	28
3.1.3. Deposition of TiO ₂ layers	29
3.1.4. Deposition of PE/TiO ₂ multilayers	31
3.1.5. Thermal treatment.....	31
3.2. Characterization methods	32
3.2.1. Auger electron spectroscopy (AES)	32
3.2.2. Atomic force microscopy (AFM)	32
3.2.3. X-ray diffraction (XRD)	32
3.2.4. Scanning electron microscopy (SEM)	33
3.2.5. Transmission electron spectroscopy (TEM)	33
3.2.5.1. Preparation of cross-sectional TEM specimens.....	34
3.2.5.2. Focused ion beam (FIB) preparation of cross-sectional TEM specimens	36
3.2.6. Quartz crystal microbalance (QCM) measurements	38
3.2.7. Nanoindentation.....	39

4. Results and discussion	43
4.1. Deposition of TiO ₂ films	43
4.1.1. Liquid flow vs. static deposition	43
4.1.2. Influence of the film thickness on the film roughness	45
4.1.3. Influence of the deposition temperature and the composition of the precursor solution on the thickness and morphology of films.....	47
4.1.4. XRD investigations	56
4.2. Synthesis of polyelectrolyte layers obtained via the layer-by-layer deposition technique and their characterization.....	59
4.2.1. Thickness measurements	59
4.2.1.1. QCM measurements.....	59
4.2.1.2. AFM measurements	61
4.2.1.3. TEM cross-section measurements	62
4.2.1.4. UV/VIS spectroscopy measurements	63
4.2.1.5. Thickness of PE films.....	64
4.2.2. Morphological characterization of the PE layers.....	65
4.3. Deposition of TiO ₂ films on modified surfaces	69
4.4. Synthesis and characterization of PE/TiO ₂ multilayers	73
4.4.1. Characterization of the topography of PE/TiO ₂ multilayers by AFM ..	73
4.4.2. Composition of PE/TiO ₂ multilayers	75
4.4.3. Microstructure of PE/TiO ₂ multilayers	77
4.4.4. Crystallinity of PE/TiO ₂ multilayers	87
4.5. Mechanical properties of the PE/TiO ₂ multilayers	93
4.5.1. Influence of residual water on the mechanical properties of the TiO ₂ layers.....	95
4.5.2. Influence of the incorporation of the organic phase on the mechanical properties of the TiO ₂ layers	98
4.5.3. Influence of the organic/inorganic ratio in the multilayer on the mechanical properties of the PE/TiO ₂ multilayer films.....	101
5. Literature	107
Curriculum Vitae	116

Abstract

The low-temperature deposition of oxide-base thin films from solution induced by organic templates is inspired by the process of biomineralization. Biominerals, i.e. inorganic materials synthesized by living organisms, show highly controlled micro- and nanostructures and in many cases physical properties superior to their manmade counterparts. In bio-inspired processes thin oxide films can be deposited from aqueous solutions on organic self-assembled monolayers or polyelectrolytes (PE). Comparing to other thin films synthesis techniques, like vacuum-based methods, besides low equipment costs, the chemical bath deposition (CBD) technique needs much less sophisticated equipments and provides a method for the deposition on complex shaped and temperature-sensitive substrates. Liquid flow deposition (LFD) for the synthesis of TiO_2 is based on the continuous flow of a precursor solution along the substrate. Whereas the concentration of the precipitating species within the reaction solution decreases with increasing deposition time, LFD provides a means to keep the concentration within the solution constant. Consequently, also the growth rate of the film is not affected by such aging effects. The deposition technique for the synthesis of PE layers is based on the electrostatic attraction between oppositely charged polyions layer by layer. The spontaneous sequential adsorption of dissolved anionic and cationic polyelectrolytes leads to the formation of ordered multilayer assemblies on a solid substrate.

In this work, both techniques were combined in order to synthesize composite, multilayer PE/ TiO_2 thin films by wet chemical processing is investigated. The main aim is to mimic the architecture of nacre, which is present for instance in sea-shells in order to achieve ceramic-based system with enhanced mechanical performances.

TiO_2 films were synthesized by the LFD technique from a HCl-containing $\text{Ti}(\text{O}_2)^{2+}$ solution at temperatures close to ambient conditions (40-90°C). The concentration of HCl was varied in the range of 7.5-160 mM, since each reaction temperature demands optimization of the acidity of the solution. Bare Si wafers or Si wafers functionalized by PE were used as substrates. The properties of the deposited films were characterized by means of SEM, XRD, AFM in order to establish the optimum

parameters of the reaction process concerning the film homogeneity, thickness, structure and surface roughness.

It is found that the deposition rate and the surface roughness of the obtained films are strongly influenced by the deposition temperature and the pH of the precursor solution. The dependence between the film thickness and the acid concentration is linear for each deposition temperature. The thickness of the film increases with the temperature and the pH (i.e. with decreasing HCl concentration). Also, SEM investigations reveal the presence of larger particles on the film surface at low acid concentrations. The formation of such particles in the solution and their sedimentation on the film surface cannot be avoided if the acid concentration is insufficient, even if the LFD technique is applied. AFM investigations of the surface roughness showed that the dependence between the surface roughness and acid concentration reaches a minimum. At constant deposition temperature and pH, the films grow linearly with the deposition time, and the surface roughness increases with increase of the film thickness.

XRD investigations showed that the TiO₂ films deposited in the temperature range 60 - 80°C are amorphous. Annealing the films at 500°C induces crystallization and the formation of anatase.

Besides using the LFD technique, TiO₂ films were also deposited applying the static deposition (SD) technique with and without changing the reaction solution. The obtained results show that the SD technique can substitute the LFD procedure, if the reaction solution is renewed in appropriate time intervals.

Polyelectrolyte (PE) films were synthesized applying the layer-by-layer deposition technique. For the deposition of polyelectrolyte films, polystyrenesulfonate (PSS) was used as polyanion, and polyethyleneimine (PEI) and polyallylamine hydrochloride (PAH) as polycations. The deposition was carried out at room temperature for 20 min.

The film thickness was determined applying AFM, TEM cross-sections and the quartz-crystal microbalance (QCM) technique. The film thickness estimated by AFM showed a linear dependence between the thickness and the number of adsorption cycles of PE couples. The thickness of the PE layers measured by AFM is in agreement with TEM cross-section images. A linear dependence between the

adsorbed mass of the layer and the number of adsorption cycles was also shown by QCM measurements.

AFM investigations of the surface morphology of the PE layers showed densely packed globular aggregates of the deposited polymer, which was revealed by STEM cross-section images. The surface roughness of the deposited PE films increases linearly with the number of adsorption cycles, i.e. the film thickness.

In order to investigate the dependence of the morphology and structure of the TiO₂ films on the surface modification, depositions on Si substrates modified with polyelectrolytes (PE) were carried on. Thickness of the deposited TiO₂ films, estimated by SEM cross-sections, is slightly higher than that of films deposited unmodified Si. Homogeneous films with the same microstructure were deposited on unmodified Si substrate and on PE-covered silicon substrates. The AFM surface roughness of the TiO₂ films on PE-coated substrates is comparable to the one of the films on bare silicon indicating a homogeneous character of the PE template.

Composite PE/TiO₂ films were synthesised by applying the layer-by-layer deposition technique for the synthesis of PE layers and the static deposition techniques for synthesis of TiO₂ layers. In order to enable the TEM characterization of the multilayers, films with thicker organic phase ((PEI/PSS)(PAH/PSS)₅) were produced. TiO₂ films were deposited from an aqueous solution of 10 mM Ti(O₂)²⁺ and 30 mM HCl at 60°C for 2h. Multilayer films with one, two, three and five PE/TiO₂ couples were synthesized.

The AFM investigations show that the TiO₂ films deposited on PE are uniform and homogeneous even after deposition of several PE/TiO₂ couples. The surface roughness increases with the number of PE/TiO₂ bilayers.

Auger electron spectroscopy (AES) was used to determine the concentrations of Ti and O (as the main constituent of the inorganic phase), C (as the main constituent of the organic phase) and Si (substrate), as a function of depth below the film surface. The AES profile clearly demonstrates the presence of a multilayered structure of alternating TiO₂-enriched and C-enriched layers; i.e. it provides proof for the existence of an ordered composite structure of well-defined inorganic and organic layers.

SEM, TEM and STEM cross-sections were used for the characterization of the microstructure of the multilayers. Analytical TEM investigations were performed using the energy-dispersive X-ray spectroscopy (EDX) and electron-energy loss spectroscopy (EELS) method. Spectra were recorded in the bulk TiO_2 layers (titanium and oxygen peaks) and in the polymer layers (carbon peaks). EDX spectra recorded in the mixed part of polymer layer showed the presence of titanium and oxygen beside carbon, which is due to the interpenetration of TiO_2 and the PE layer. The EEL spectra that correspond to the TiO_2 layer showed the presence of the Ti-L_{2,3} and O-K edges and the presence of the C-K edge in the dense polymer layer. The spectra that correspond to the part of the PE layer interpenetrated by TiO_2 show the presence of C-K edge and apart from that also the presence of Ti-L_{2,3} and O-K edges which is also in agreement with the EDX results. Additionally the energy loss near edge fine structures (ELNES) studies of the Ti-L_{2,3} and O-K edges were employed for further characterization. The experimental spectra of Ti-L_{2,3} and O-K edges recorded for TiO_2 layers correspond to the spectrum of amorphous TiO_2 , according to literature data.

HRTEM studies were applied to examine possible beam damages or beam induced crystallization when sample is exposed to an electron beam. Before electron-beam irradiation the TiO_2 layers are mainly amorphous. The beam induced crystallization (electrons of 400 keV incident energy) starts after the layers were exposed to the electron beam for approximately 15 minutes, the number of crystallites and their size increase with the irradiation time and after one hour the TiO_2 layers are mainly composed of crystals with an amorphous matrix with the grains about 10 – 20 nm in size.

The nanoindentation technique was employed to determine the mechanical properties of obtained composite films, with the emphasis on their hardness and Young's modulus.

It was found that the increase in hardness varying from ~0.9 GPa to ~1.25 GPa, for as-deposited and aged films, respectively, can be attributed to the removal of chemically and physically bound residual water from the film during the aging.

The comparison of the nanoindentation data obtained from the TiO_2 single layer and the $(\text{PE}/\text{TiO}_2)_2$ and $(\text{PE}/\text{TiO}_2)_3$ multilayer samples, with an organic/inorganic ratio of 25 nm/125 nm, reveals that the incorporation of organic layers improves the

mechanical properties of CBD-derived TiO_2 films. Evaluation of these data yields values of ~ 1.2 GPa for the hardness of TiO_2 single layers and 1.5 - 1.7 GPa for the PE/ TiO_2 multilayer films. This enhanced mechanical performances can be attributed to the hardening by the differences in shear modulus between the organic and the inorganic phase and the interaction between the incorporated TiO_2 particles and the PE, which is stronger than the one between the TiO_2 particles within the oxide layers. Also, the influence of the organic/inorganic ratio of the PE/ TiO_2 multilayer films was investigated. Evaluations of the nanoindentation data give values of ~ 1.7 GPa for the hardness of the $(\text{PE}/\text{TiO}_2)_6$ multilayer film with the organic/inorganic ratio 10 nm/50 nm. These results are comparable to the hardness values of the $(\text{PE}/\text{TiO}_2)_3$ film with an organic/inorganic ratio of 25 nm/125 nm. In contrast, the hardness values of films with an organic/inorganic ratio of 5 nm/50 nm and 2.5 nm/50 nm (~ 1.3 GPa) approach the hardness values of monolithic TiO_2 film. A decrease in the thickness of the organic phase in the composite film from the thickness of 10 to 5 and 2.5 nm also decrease the value of the Young's modulus. The inferior mechanical performances of the composite with thinner organic layer (5 and 2.5 nm) can be explained by an inhomogeneous distribution of the very thin polymer layers along the surface of the TiO_2 layers due to their surface roughness. So, it can be assumed that the polymer layer is discontinuous in some parts of the multilayer and in these areas the behavior of the composite is approaching the one of single layered TiO_2 .

Zusammenfassung

Die Abscheidung oxidischer dünner Schichten bei niedrigen Temperaturen auf organischen Template hat die Prozesse der Biomineralisation zum Vorbild. Biomineralien, d.h. anorganische Materialien, die durch lebende Organismen erzeugt werden, zeigen hoch kontrollierte Gefüge und in vielen Fällen physikalische Eigenschaften, die ihren künstlich hergestellten Pendanten weit überlegen sind. In bioinspirierten Verfahren können so dünne oxidische Schichten aus wässrigen Lösungen auf organischen selbstorganisierten Monolagen (SAMs) oder Polyelektrolyt-Mehrlagenschichten (PEM) synthetisiert werden. Im Vergleich zu anderen Techniken zur Dünnschichtherstellung bieten nasschemische Verfahren (Chemical bath deposition - CBD), vom geringen apparativen Aufwand abgesehen, eine Methode zur Abscheidung auf komplex geformten und temperaturempfindlichen Substraten. Die Erzeugung von PEM durch sukzessive, schichtweise Aufbringung basiert auf der elektrostatischen Anziehung entgegengesetzt geladener Polyionen. Die spontane sequentielle Adsorption gelöster anionischer bzw. kationischer Polyelektrolyte führt zur Bildung geordneter Mehrlagenschichten auf festen Substraten. Die Abscheidung in Flusszellen (Liquid-flow deposition - LFD) zur Erzeugung dünner Schichten von TiO_2 stellt eine interessante Erweiterung des Prozesses CBD dar, bei dem für eine kontinuierliche Erneuerung der Reaktionslösung auf dem Substrat gesorgt wird. Während sich die chemische Zusammensetzung der Lösung bei statischen Methoden mit der Zeit ändert, ermöglicht das LPD-Verfahren bei geeigneter Wahl der Reaktorgeometrie und Flussrate einen stationären Zustand für konstante Zusammensetzung und Reaktivität des Mediums zur Substratbeschichtung. Zudem kann so die Wachstumsrate erhöht und ihre Abnahme bei längeren Abscheidezeiten vermieden werden.

In der vorliegenden Arbeit wurde die Herstellung mehrlagiger PE/ TiO_2 -Komposite, die das Gefüge in Muschelschalen (Kompositstrukturen aus organischen und mineralischen Schichten im Verhältnis von ~5:95 vol%) nachempfinden, durch nasschemische Verfahren untersucht, mit dem Ziel die mechanischen Eigenschaften im Vergleich zu einlagigen TiO_2 -Schichten zu verbessern.

TiO_2 -Schichten wurden mittels des LPD-Verfahrens, bei Verwendung einer 10 mM wässrigen Lösung eines Titan-Peroxokomplexes $[\text{Ti}(\text{O}_2)]^{2+}$ im Temperaturbereich

von 40-90 °C bei Zugabe geeigneter Mengen von HCl im Konzentrationsbereich von 7.5 – 160 mM, erzeugt. Als Substrate kamen dabei sowohl unmodifiziertes als auch mit PEM modifiziertes Silicium zum Einsatz. Die so hergestellten Schichten wurden mittels der Rasterelektronenmikroskopie (REM), Röntgenbeugung (XRD) sowie Rasterkraftmikroskopie (AFM) charakterisiert, um die optimalen Reaktionsparameter in Bezug auf Homogenität, Dicke, Oberflächenrauigkeit und Gefüge zu bestimmen. Dabei wurde gefunden, dass die Wachstumsrate und die Oberflächenrauigkeit stark von der gewählten Reaktionstemperatur sowie der Zusammensetzung der Reaktionslösung, insbesondere der Säurekonzentration, abhängen. Die Dicke der erhaltenen Schichten erhöht sich mit zunehmender Temperatur und mit geringeren Säurekonzentrationen aufgrund kürzerer Induktionszeiten. Weiter zeigen die REM-Abbildungen die Bildung größerer Kolloidpartikel, die sich bei zu gering gewählter Säurekonzentration in der Lösung bilden, und dann auf der Substratoberfläche sedimentieren. Dieses kann auch nicht durch die Verwendung des LPD-Verfahrens umgangen werden.

AFM-Untersuchungen der Oberflächenrauigkeit ergaben, dass diese zunächst bei größeren Säurekonzentrationen abnimmt, dann jedoch ein Minimum durchläuft und wieder steigt. Dieses Verhalten könnte auf einen Wechsel des Abscheidemechanismus von homogener (Partikelwachstum in Lösung) zu heterogener (sukzessive Anlagerung von Ionen am Substrat) Keimbildung oder auch auf einen gemischten Mechanismus hindeuten.

XRD-Untersuchungen zeigten, dass die TiO₂-Filme, die im Temperaturbereich von 60-80 °C hergestellt wurden, amorph waren. Tempern bei 500°C induzierte die Kristallisation der Schichten, wobei die Anatas-Phase gebildet wird.

Weiter wurden auch statische Abscheidung mit und ohne Austausch der Reaktionslösung zur Schichtherstellung eingesetzt. Dabei zeigte sich, dass ausreichend häufige Wechsel der Lösung zu Resultaten führten, die denen bei Einsatz des LPD-Verfahrens vergleichbar waren.

PEM wurden durch schichtweise Abscheidung von Polyelektrolyten aus wässrigen Lösungen hergestellt. Dazu wurden Polystyrolsulfonat (PSS) als anionische und Polyethylenimin (PEI) sowie Polyallylaminhydrochlorid (PAH) als kationische Komponente verwendet. Die Synthese der PEM erfolgte bei Raumtemperatur und Abscheidungszeiten für die einzelnen Polyelektrolyte von jeweils 20 Minuten.

Die Schichtdicke der so erzeugten PEM wurde durch AFM, Transmissionelektronenmikroskopie (TEM) sowie mittels Quartz-Mikrowaage (Quartz crystal microbalance - QCM) bestimmt. Dabei zeigt die Dicke eine lineare Abhängigkeit von der Anzahl der Adsorptionszyklen eines Polyelektrolytpaares. Die AFM- und TEM-Untersuchungen führten dabei zu vergleichbaren Ergebnissen. Die Ergebnisse der QCM-Messungen ergaben ebenfalls einen linearen Verlauf, jedoch hängen die Werte für die Schichtdicke von bei der Auswertung verwendeten Näherungen, insbesondere der Dichte der PEM ($\sim 1.2 \text{ g/cm}^3$) ab.

Die Oberflächentopographie der PEM wurden mittels AFM charakterisiert. Die PEM bestehen aus dicht gepackten globularen Aggregaten der verwendeten Polyelektrolyte. Diese Ergebnisse werden durch Raster transmissionelektronenmikroskopie (RTEM)-Querschnitte bestätigt. Die Oberflächenrauigkeit der PEM wächst annähernd linear mit der Zahl der Adsorptionszyklen, also mit entsprechend wachsender Schichtdicke.

Morphologie und Gefüge der TiO_2 -Schichten wurde auch in Abhängigkeit von organischen Beschichtungen der Siliciumoberflächen untersucht. Dabei wurde die direkte Abscheidungen auf Si-Substrate mit solchen auf PEM-modifizierte substrate verglichen. Abscheidungen wurden auf die bereits beschriebene Weise durchgeführt, d.h. mittels LFD-Verfahren mit einer Lösung von $10 \text{ mM } [\text{Ti}(\text{O}_2)]^{2+}$ und 30 mM HCl bei $60 \text{ }^\circ\text{C}$ über 4 Stunden. Die Dicke der TiO_2 -Filme, die aus REM-Querschnitten ermittelt wurde, war auf organisch modifizierten höher als auf unbehandelten Silicium-Substraten. REM-Untersuchungen zeigten in allen Fällen gleichmäßige Oberflächenbedeckung. Die Rauigkeit von Filmen auf Substraten mit und ohne PEM ist hingegen vergleichbar. Die vergleichsweise dünne PEM-Schicht scheint hier keinen signifikanten Einfluss zu haben.

Komposite von alternierenden PE/ TiO_2 -Schichten wurden durch wechselnden Einsatz der oben beschriebenen Verfahren zur Herstellung der PEM-Schichten sowie der TiO_2 -Schichten durch statische Tauchverfahren hergestellt. Zur einfacheren Charakterisierung wurden organische Mehrlagenschichten der Abfolge $((\text{PEI}/\text{PSS})(\text{PAH}/\text{PSS})_5)$ eingesetzt. TiO_2 -Schichten wurden aus Lösungen von $10 \text{ mM } [\text{Ti}(\text{O}_2)]^{2+}$ und 30 mM HCl bei $60 \text{ }^\circ\text{C}$ in 2 Stunden abgeschieden. Für

Untersuchungen zur Entstehung der Komposite wurden Mehrlagenschichten aus einem, zwei, drei und fünf PE/TiO₂-Paaren synthetisiert.

Untersuchungen mittels AFM der so hergestellten Kompositschichten weisen daraufhin, dass sich Morphologie der Schichten mit steigender Anzahl an PE/TiO₂-Paaren nicht grundlegend ändert. Die Oberflächenrauigkeit nimmt jedoch mit dieser Anzahl zu.

Des Weiteren wurde die Augerelektronen-Spektroskopie (AES) eingesetzt, um die Konzentrationen von Ti und O (als Hauptkomponente der anorganischen Phase), C (als Hauptkomponente der organischen Phase) sowie Si (Substrat) als Funktion der Schichttiefe zu bestimmen. Die AES-Profile weisen mit alternierenden TiO₂- und C-reichen Phasen deutlich auf die Existenz geordneter und gut definierter anorganischer und organischer Schichten hin und bestätigen damit die gewünschte Mehrlagenstruktur der PE/TiO₂-Komposite.

Querschnitte aus REM-, TEM- und STEM-Untersuchungen wurden zur weiteren Charakterisierung des Gefüges der mehrlagigen Komposite verwendet. Analytische TEM-Untersuchungen mit Energiedispersive Röntgenspektroskopie (EDX) und Elektronen-Energieverlustspektroskopie (EELS) wurden durchgeführt. Spektren wurden sowohl von TiO₂-Schichten (Ti- und O-Signale) als auch von den PEM-Schichten (C-Signale) aufgenommen. EDX-Untersuchungen zeigen jedoch auch Bereiche, die neben Kohlenstoff auch deutliche Signale für Ti und O aufweisen. Da die PEM nicht vollständig dicht sind, weist dies auf eine teilweise Durchdringung der organischen Schicht mit TiO₂-Partikeln hin.

Auch die EEL-Spektren lassen sich zur Identifizierung der verschiedenen Bereiche des Kompositmaterials nutzen. Während, wie zu erwarten, die TiO₂-Schicht Ti-L_{2,3} und O-K-Kanten und die PEM-Schicht C-K-Kanten aufweisen, gibt es auch Teile, die alle diese Signale zeigen, was in Übereinstimmung mit den bereits erwähnten EDX-Untersuchungen ist. Weiter wurde die Energie-Verlustnahkantenstruktur (ELNES) der Ti-L_{2,3} und O-K-Kanten zur Bestimmung der Modifikation des TiO₂ angewendet. Hier wurde die beste Übereinstimmung mit Literaturdaten für amorphes TiO₂ gefunden.

Zudem wurden auch HRTEM-Untersuchungen eingesetzt um das Gefüge der TiO₂-Schichten zu untersuchen. Hierbei zeigte sich, dass Kristallisation der Proben durch Bestrahlung mit Elektronen induziert werden kann. Die Kenntnis des Auftretens dieser Artefakte ist für eine sinnvolle Interpretation unbedingt notwendig. Vor der Bestrahlung sind die TiO₂-Schichten hauptsächlich amorph. Die vom

Elektronenstrahl (400 keV Einfallstrahlung) verursachte Kristallisation beginnt nach etwa 15 Minuten. Die Zahl und Größe der Kristallite nehmen dabei mit der Dauer der Bestrahlung zu, so dass die TiO₂-Schichten nach einer Stunde hauptsächlich aus kristallinen Anteilen mit einer Korngröße von 10-20 nm bestehen und nur noch sehr geringe amorphe Teile aufweisen.

Schließlich wurden die mechanischen Eigenschaften, insbesondere Härte und Elastizitätsmodul, der PE/TiO₂-Komposite mittels Nanoindentation bestimmt. Dabei wurde gefunden, dass die Härte von TiO₂-Einlagenschichten im Laufe einiger Tage von ~0.9 GPa auf ~1.25 GPa zunimmt, was vermutlich auf Trocknung der Schichten zurückzuführen ist.

Der Vergleich der so bestimmten Daten von TiO₂-Einlagenschichten mit PE/TiO₂-Mehrlagenschichten machte deutlich, dass der Einbau der organischen Schichten die mechanischen Eigenschaften deutlich verbessert. Die Auswertung ergab, Werte von ~1.2 GPa für TiO₂-Einlagenschichten und ~1.5 bis ~1.7 GPa für die PE/TiO₂-Mehrlagenschichten. Diese Verbesserung kann auf Härtung durch Unterschiede im Schermodul zwischen organischer und anorganischer Phase und eine stärkere Bindung zwischen TiO₂-Partikeln und PEM als zwischen den TiO₂-Partikeln untereinander zurückgeführt werden.

Weiter wurde der Einfluss der Dicke der PEM als auch des Verhältnisses der Schichtdicken von organischer zu anorganischer Schicht im Komposit untersucht. Dabei zeigten sich deutlich geringere Werte für Komposite mit dünneren organischen Schichten (5 bzw. 2.5 nm). Dafür könnte eine inhomogenere Verteilung aus der im Vergleich zur Rauigkeit der TiO₂-Schicht geringeren Dicke der PEM maßgeblich sein.

1. Introduction

The outstanding performance of many biological materials has inspired numerous researchers to transfer the structural design principles found in nature to artificially made materials. Biominerals, i.e. inorganic materials synthesized by living organisms, show highly controlled microstructures and in many cases physical properties superior to their manmade counterparts. Recent experimental and theoretical investigations have evidenced that the outstanding mechanical properties of some biomaterials arise from the high degree of hierarchical organisation from the microscale down to molecular scale. One of the examples is nacre (mother-of-pearl), a biological composite of a ceramic phase and macromolecules, which can be found in many families of mollusk shells. Nacre has a highly regular 'brick-and-mortar' structure composed of alternating mineral layers separated by thin layers of organic material [1995 SAK]. This highly organized structure yields a few thousand times higher toughness in comparison to its constituent material (CaCO_3), and furthermore enables an excellent combination of stiffness, strength and impact resistance [2000 KSB]. The underlying toughening mechanism has been attributed to enhanced crack deflection, through which efficient dissipation of the applied fracture load is achieved [1988 Man].

Up to now, organic/inorganic nanostructured composites have been obtained via sol-gel processes [2003 MTS, 2005 MBR]. Also, there are several investigations which reported the deposition of inorganic phases in the form of exfoliated mineral clays [1997 KHT, 2003 TKM], carbon nanotubes [2003 MKP] or oxide particles [1997 LAO, 1998 RLC, 2001 SET] applying the bio-inspired approach. The organic component is usually deposited via a layer-by-layer deposition of macromolecules or Langmuir-Blodgett films [1995 FMe, 1997 Dec, 2001 Mit]. The mechanical properties of such artificial organic/inorganic composites have been found to be enhanced compared to their constituents, but the outstanding properties of their natural counterparts have not been achieved yet [2005 May].

Bio-inspired synthesis routes for obtaining inorganic layers in organic/inorganic multilayer composites by chemical bath deposition (CBD) technique have also been investigated [2001 NDe, 2005 GKo]. These techniques operate at low temperatures ($30\text{-}100^\circ\text{C}$), similar to the formation of natural organic/inorganic nanocomposites via biomineralization, i.e. at or near ambient temperature in aqueous environments. Using such procedures, good adhesion to the substrate has been achieved with the

aid of organic self-assembled monolayers (SAM) on the substrate serving as templates to promote the formation of the inorganic phase at the interface to the aqueous solution [2005 GKo]. The CBD procedures enable the efficient coating of irregular-shaped and temperature-sensitive substrates and provides access to good-quality oxide films of controllable thickness. The liquid flow deposition (LFD) technique, as a variation of the CBD technique, is based on the continuous flow of the precursor solution along the substrate, which exposes the substrate to a medium of constant composition and reactivity [2002 BHF].

As an alternative to Langmuir-Blodgett films and SAMs, the layer-by-layer deposition technique of polyelectrolytes (PE) found application in the synthesis of organic layers mostly due to its simplicity, versatility and speed [1997 Dec]. This technique is based on the electrostatic attraction between oppositely charged polyions. The spontaneous sequential adsorption of dissolved anionic and cationic polyelectrolytes leads to the formation of ordered multilayer assemblies on a solid substrate. Beside for polyelectrolytes, the layer-by-layer deposition technique is also suitable for charged nanoobjects, such as molecule aggregates, clusters or colloids [1997 Dec, 2000 BJL].

Studies of the mechanical performance of nacre-like thin films produced via bio-inspired routes are still in their infancy due to the fact that the traditional testing methods used for bulk materials are often not applicable. In this context, novel perspectives are opened by the depth-sensing nanoindentation technique [1992 OPh], which employs high resolution sensors and actuators to continuously control and monitor the loads and displacements on a nano-sized indenter relative to the surface of the material to be investigated as they are interacting. Hardness and Young's modulus of the material can be derived from the gained load-displacement data [1997 Nix, 2004 OPh]. However, only few nanoindentation investigations have so far been carried out on thin metal-oxide coatings. In one study thin sol-gel-derived TiO_2 films were considered and elastic modulus and hardness of amorphous and crystalline sub-micron thick films were evaluated [2000 OBJ].

In the present work, the bio-inspired synthesis of nano-composite films composed of alternating layers of TiO_2 as inorganic component and polyelectrolytes as organic component is presented. By this approach, the principles of nacre-like architectures formed in nature via biomineralization are transferred for the first time to the synthesis of oxide materials of technological relevance. For this purpose a CBD-

based procedure is employed to deposit 50-150 nm thick TiO_2 layers from aqueous solutions of inorganic titanium salts. The deposition of such films proceeds by the formation of colloids in the reaction solution (homogeneous nucleation) and their subsequent attachment on the substrate, which can be understood in terms of the DLVO theory (Derjaguin, Landau, Verwey and Overbeck) [1998 SAD]. Such oxide layers then allow the adsorption of polyelectrolytes, thereby constituting the base for the layer-by-layer assembly of organic layers with a thickness of few to few tens of nanometers.

It will be demonstrated that this route combining CBD with electrostatic assembly yields compact composite films in which oxide layers are well-separated from each other by an organic interlayer. Moreover, the mechanical properties of the films obtained in this manner have been elucidated using nanoindentation. It will be shown that the incorporation of organic interlayers improves the mechanical performances of CBD-derived films as compared to monolithic TiO_2 layers.

2. Literature overview

2.1. Biomineralization and bio-inspired processing

There are numerous examples in nature for inorganic functional structures established by biomineralization (Tab. 2.1). Thereby living organisms deposit inorganic materials like calcium carbonates, phosphates and oxalates, iron oxides and silica from aqueous solutions at ambient temperature onto organic matrices, in order to form mineralized tissues such as bones, mollusk shells, teeth or eggshells. The organic phases dictate where the inorganic phase will form, as well as its size, crystallographic orientation, texture and macroscopic shape [1992 HFL, 1995 SAK, 1996 ATM].

Tab. 2.1 Some types and functions of inorganic solids in biological systems [1995 SAK]

Mineral	Formula	Organism/Function
Calcium Carbonate: Calcite Aragonite Vaterite Amorphous	CaCO_3 CaCO_3 CaCO_3 $\text{CaCO}_3 \cdot n\text{H}_2\text{O}$	Algae/exoskeletons, Triobites/eye lens Fish/gravity device, mollusks/exoskeleton Ascidans/spicules Plants/Ca storage
Calcium Phosphate: Hydroxyapatite Octa-calcium phosphate Amorphous	$\text{Ca}_{10}(\text{PO}_4)_6(\text{OH})_2$ $\text{Ca}_8\text{H}_2(\text{PO}_4)_6$?	Vertebrates/endoskeletons, teeth, Ca storage Vertebrates/precursor phase in bone Mussels/Ca storage
Calcium Oxalate: Whewellite Weddelite	$\text{CaC}_2\text{O} \cdot \text{H}_2\text{O}$ $\text{CaC}_2\text{O} \cdot 2\text{H}_2\text{O}$	Plants/Ca storage Plants/Ca storage
Group 11A Metal Sulfates: Gypsum Barite Celestite	CaSO_4 BaSO_4 SrSO_4	Jallyfish larvae/gravity device Algae/gravity device Acantharia/cellular support
Silicon Dioxide: Silica	$\text{SiO}_2 \cdot n\text{H}_2\text{O}$	Algae/exoskeletons
Iron oxide: Magnetite Goethite Lepidocrocite Ferrihydrate	Fe_3O_4 a-FeOOH g-FeOOH $5\text{Fe}_2\text{O}_3 \cdot 9\text{H}_2\text{O}$	Bacteria/magnetotaxis chitons/teeth Limpets/teeth Chitons (Mollusca)/teeth Animals and plants/Fe storage proteins

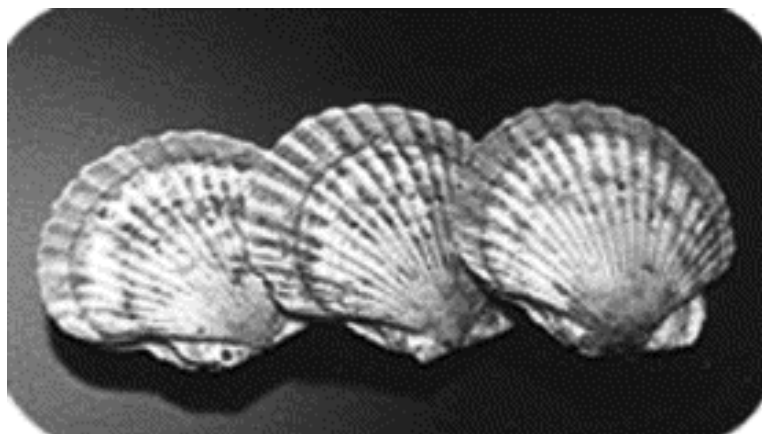
Experimental and theoretical investigations showed that outstanding mechanical properties of biomaterials arise from the high degree of hierarchical organization from microscale down to the molecular scale [1995 SAK]. In this connection, biominerals often show superior physical properties compared to their isolated constituents or to man-made counterparts.

One of the most investigated biominerals is nacre (mother-of-pearl). Nacre is a biological composite of a ceramic phase and organic macromolecules. Its significance as a structural material stems as already mentioned from its excellent mechanical properties, such as fracture toughness and strength (Tab. 2.2), which are comparable or increased compared to advanced structural ceramics [1995 SAK].

Tab. 2.2 Mechanical properties of nacre and its artificial constituents [2004 JGa]

	Volume fraction	Young's modulus	Strength	Fracture toughness
Protein	1–5 %	50–100 MPa	20 MPa	-
CaCO ₃	95-99 %	50–100 GPa	30 MPa	<< 1 MPam ^{1/2}
Nacre		50 GPa	100-300 MPa	3-7 MPam ^{1/2}

The structure of nacre is found in many families of mollusc shells of the gastropod family including abalone, cephalopods such as nautilus, bivalves such as pearl oysters and blue mussels (Fig. 2.1). The structure of a molluscan shell can be divided into three primary sections: periostracum, prismatic and nacreous layer. The sum of the prismatic and nacreous layers occupies the main structural part of the shell, determining the shape, mechanical strength and toughness of the shell. The periostracum is the outer layer, consisting mainly of conchiolins (proteins and polysaccharides). The nacreous layer is the inner layer and is mainly made of oriented aragonite crystals [2004 CPW].



a)



b)

Fig. 2.1 a) The Bivalva shell with fan shape; b) the nacre of Nautilus [2004 CPW]

The nacre is composed of ~95 vol% hexagonal, polygonal or rounded aragonite tablets which have dimensions of ~5–20 μm in length and ~0.15–1.5 μm in thickness and remaining ~5 vol% of organic matrix with ~10–300 nm in thickness as shown in Fig. 2.2 and Fig 2.3. The organic layer has pores for mineral bridges to pass through, and intracrystalline proteins are present within aragonite tablets themselves [2005 BQB]. This highly regular ‘brick-mortar’-type arrangement in nacre made of nano-sized inorganic and organic components ensures an effective combination of the high strength of the mineral particles with the elasticity of the protein layers between them.

This structure results in high toughness by stress-distribution and crack-stopping mechanism [2003 GJJ].

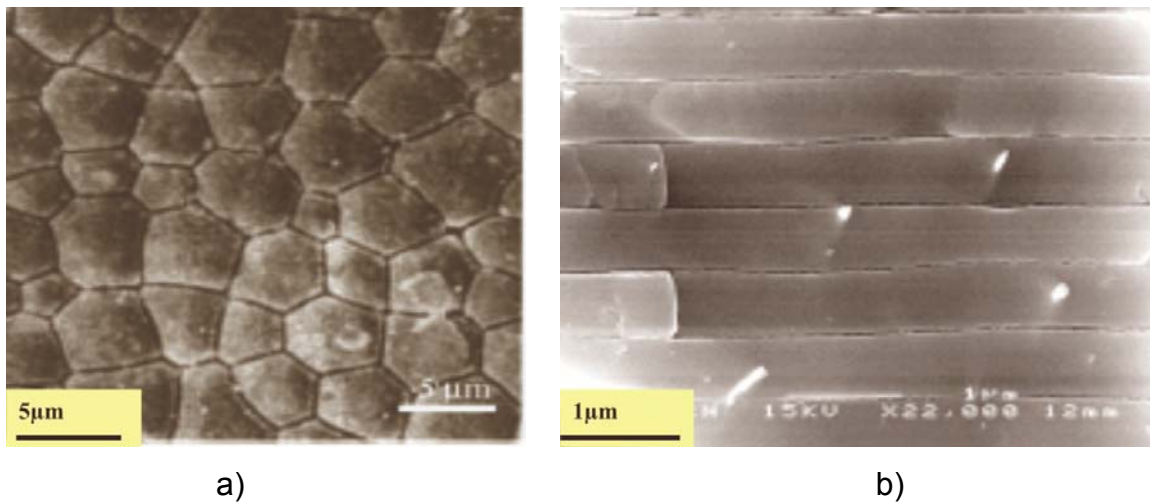


Fig. 2.2 SEM images of microstructure of abalone nacre: a) top and b) cross-section view

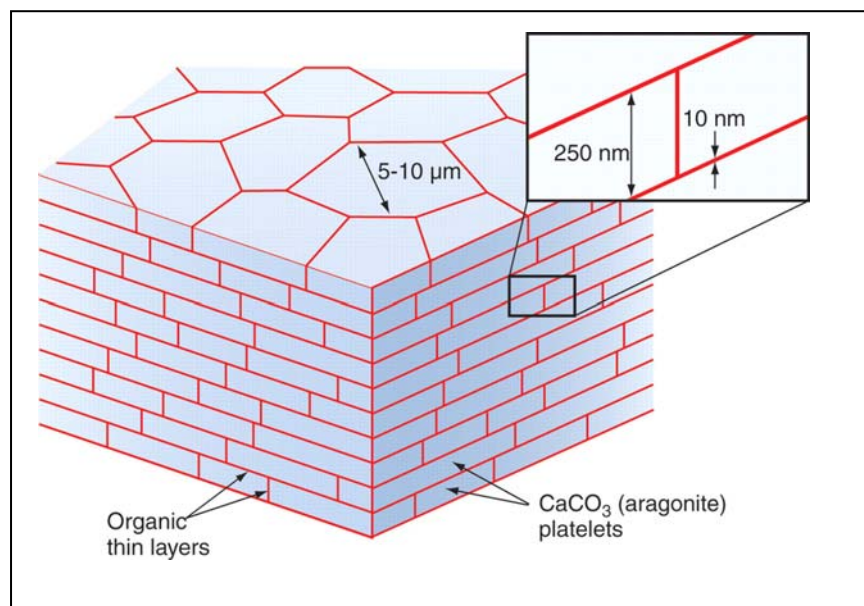


Fig. 2.3 Schematic 3D diagram of nacreous structure [2005 May]

Two primary toughening mechanisms for controlling damage were identified in shells [2000 MMM]: (1) sliding of inorganic blocks by means of viscoplastic deformation of the organic interlayers (Fig. 2.4 a) and (2) deflection of cracks by the organic layers (Fig. 2.4 b). These two mechanisms based on laminated microstructure lead to delocalization of failure, by which one single sharp crack is replaced by a large number of small cracks, within a broader region.

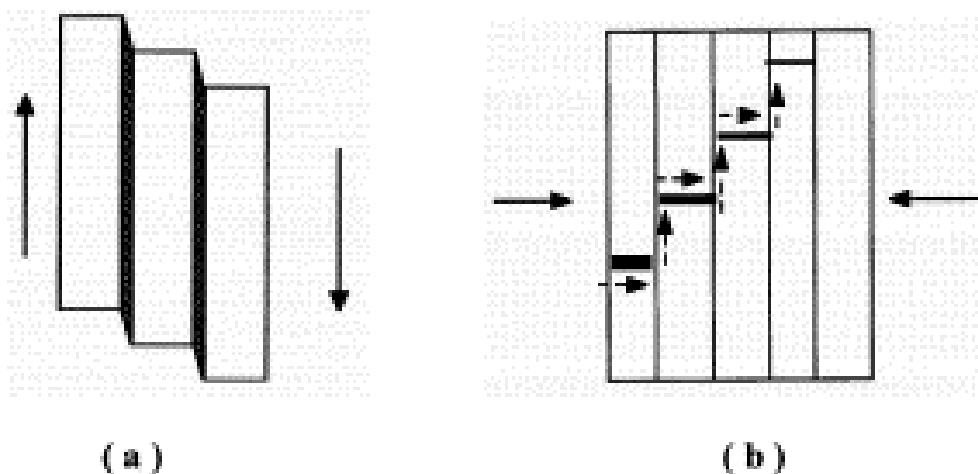


Fig. 2.4 Primary toughening mechanisms in shells: a) viscoplastic deformation of organic layers; b) crack deflection by organic layers [2000 MMM]

Also, based on the work of Jäger and Fratzl [2000 JFr] on the staggered arrangement of bone fibrils, Gao et al [2003 GLJ] proposed a one-dimensional composite model to study the nanoscale effective stiffness of a shell, presented in Fig. 2.5. The mineral crystals have large aspect ratios and are much harder than the soft protein matrix, and the tensile zone in the protein matrix near the ends of mineral crystals is assumed to carry no mechanical load. The load transfer is largely accomplished by the high shear zones of the protein between the long sides of mineral platelets. Therefore, the composite model of Fig. 2.5 a) can be simplified to Fig. 2.5 b) where the tensile zone of the soft phase is eliminated from the composite structure. Under an applied tensile stress, the mineral platelets carry most of the tensile load while the protein matrix transfers the load between mineral crystals via shear. The path of load transfer in the composite is thus simplified to an one-dimensional serial spring system consisting of mineral elements (tension) interspersed among protein elements (shear). Hence the model can be called a tension-shear chain model of biological nanostructure. The large aspect ratio of the minerals platelets ensures that the force

transferred between the platelets is distributed over a large shear region with relatively small stress within the protein.

Also, the critical length scale for mineral crystals was estimated (~ 30 nm) below which the fracture strength of a cracked crystal is identical to that of perfect, defect-free crystal. This length scale indicates that the nanometer size of mineral platelets in biocomposites may be the result of fracture strength optimization. As the thickness of mineral platelets in nacre can be several hundred nanometers larger than this estimated value, the thickness of mineral platelets may be a result of constrained optimization caused by the large volume fractions of mineral content in nacre. So, at a mineral volume fraction of 95% and a protein layer thickness of 10 nm (which is approaching the minimum size of single protein molecules), the mineral crystal needs to be of a thickness of about 200 nm.

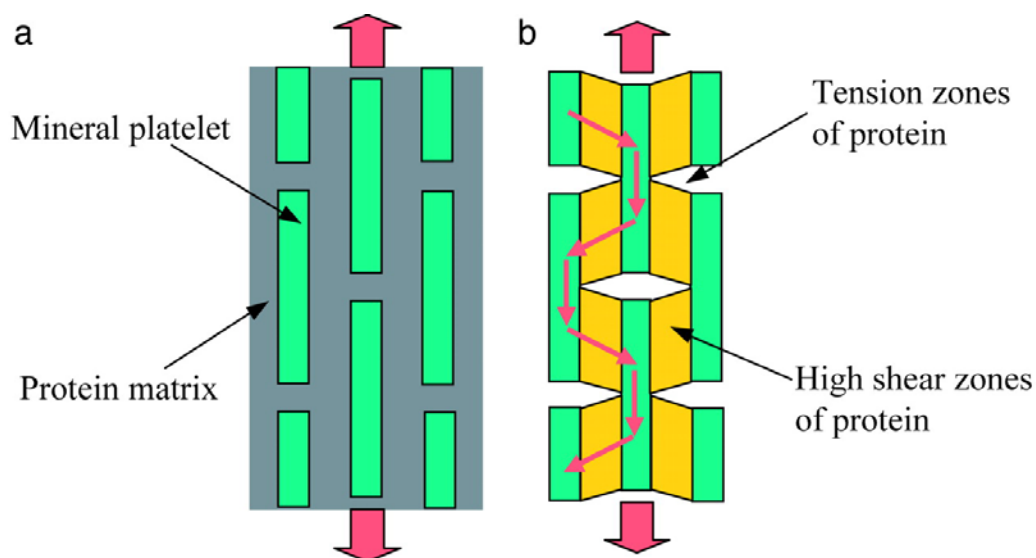


Fig. 2.5 A model of biocomposites a) Scheme of staggered mineral crystals embedded in protein matrix; b) tension-shear chain model of biocomposites in which the tensile regions of the protein are eliminated to emphasize the load transfer within the composite structure [2003 GLJ]

The general principles of biomineralization [1992 HFL] can be summarized as the following: (1) Biomineralization occurs within specific subunit compartments which implies crystal formation at certain functional sites. (2) A specific inorganic phase with a defined crystal size and orientation is grown by mediation of an organic phase. (3) Macroscopic growth is accomplished by packaging many incremental units together which results in formation of specific laminated structures in most cases.

The adaptation of one or more of this biological principles for producing novel organic layer-mediated materials is termed by 'bio-inspired processing' or 'bio-inspired approach' and it finds application in aqueous synthesis of oxides, sulfides and other ceramics [1992 HFL, 1997 ADH]. The bio-inspired processing generally has two important characteristics: (1) the use of an aqueous solution of soluble precursors to deposit ceramics and (2) the use of functionalized surfaces to promote crystallization at the interfaces of substrate solution [2001 WZh]. In bio-inspired processing several strategies are employed for functionalizing surfaces like: (1) chemical modification of plastics, (2) electrochemical deposition of functionalized polymers and (3) use of organic systems [1994 BRT]. The use of organic system include functionalizing surfaces with Langmuir and Langmuir-Blodgett (LB) films, liquid crystals, self-assembled monolayers (SAMs) and polyelectrolytes.

The main advantages of bio-inspired processing of inorganic materials include [1994 BRT]: (1) low cost and low temperature synthesis; (2) in most cases the formation of crystalline materials without subsequent heat treatment; (3) deposition ability on complex shaped surfaces; (4) deposition on a wide range of substrates, like plastics and temperature sensitive materials; (5) microstructure control and ability to produce nanostructured materials; (6) direct deposition of micro-scale patterned films. By appropriate control of solution and surface chemistry a variety of ceramics materials were formed by the bio-inspired processing such as CaCO_3 [1996 CRi], $\text{Ca}_3(\text{PO}_4)_2$ [1991 DKK], FeOOH [1996 TRL], Fe_2O_3 [1994 BRT], SnO_2 [2000 SDe], Y_2O_3 [1997 ADe], TiO_2 [1999 KSS, 1999 SIH, 2002 PSS], ZnO [2003 HJB], ZrO_2 [1997 ADH], NiO [2000 PKN], V_2O_5 [2004 HJW], CdS [1998 OMc], as well as organic/inorganic multilayer structures [2001 WZh].

2.2. Wet chemical processing

The main techniques in wet chemical processing include [2001 NDe, 2005 GKo]: (1) chemical bath deposition (CBD); (2) successive ion layer adsorption and reaction (SILAR); (3) liquid phase deposition (LPD); (4) electroless deposition with or without catalyst (ED), as well as variations of these techniques such as photochemical deposition (PCD), deposition assisted by applied fields, ferrite plating, using of functionalized surfaces and liquid-flow deposition (LFD). All of these techniques use aqueous solutions and low temperatures ($<100^{\circ}\text{C}$) for the synthesis of crystalline or amorphous ceramics films and powders.

By chemical bath deposition a solid film in a single immersion through control of the kinetics of formation of a solid is produced, usually without changing oxidation state of the metals. Most of the applications of CBD lie in the synthesis of sulfide and selenide films [2000 MLo], but it can also be successfully used for the deposition of oxide films [1998 OMc, 2001 NDe]. In these cases, the deposition medium for the CBD consists of a metal salt M^{n+} (chlorides, nitrates, sulfates or acetates), a source for the chalcogenide X (X = S, Se, O), and usually a complexing agent which provides ligands such as ammonia, citrate, cyanide, tartrate or ethylenediamine. Deposition is taking place in aqueous solutions. Careful control of the pH value of the solution, the choice of the complexant and its concentration and the reaction temperature is required. With the deposition of oxide films, water serves as the source of oxygen.

During the time of film deposition from a static liquid by the CBD process, some gradual changes in the reaction solution can occur due to a decrease of the concentration of the film-forming species in solution, resulting in a decrease of the film growth-rate [2002 BHF]. Also, large particles and agglomerates can be formed in the solution and deposited on the substrate surface. In order to reduce these solution aging effects, liquid flow deposition (LFD) is applied. In this case, the stock solution is continuously flowed over the substrate, providing a reaction medium with constant composition and reactivity during deposition. Beside to CBD, the concept of LFD can be also applied in other wet chemical processing techniques, like LPD [2001 NDe]. A variety of ceramic materials was synthesized by LFD such as TiO_2 [2002 FHN], ZnO [1996 INa], SnO_2 [2003 SDH] and CdS [1994 ITa].

2.3. Deposition of oxide films

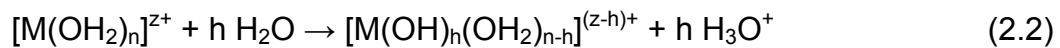
The formation of solid oxide phases from solutions is based on inorganic polycondensation involving the hydrolysis of metal ions and the condensation of hydroxylated complexes. The hydrolysis and condensation reactions are providing the base for the formation of colloidal particles which can be divided into the following steps [2000 Jol]:

- (1) Formation of the zero-charge precursor $[M(OH)_z(OH_2)_{N-z}]^0$;
- (2) Nucleation;
- (3) Growth of nuclei;
- (4) Aging of particles.

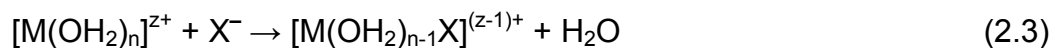
The initial stage of this process is metal ion (M^{z+}) hydration, where in aqueous solutions a hydration sphere of water molecules is formed around a central atom:



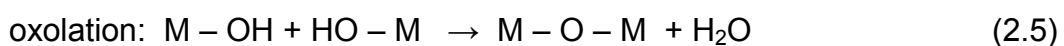
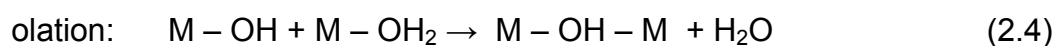
The formation of the zero-charge precursor is combined with a deprotonation of the metal cations which are solvated by water molecules:



This reaction depends on the acid concentration of the solution and can be also influenced by the complexation with anionic species (X^-), which controls the precipitation of the inorganic solid from solution:



The creation and growth of oxide based nuclei by further condensation of the hydrolyzed metal ions involves olation reactions by the formation of hydroxo bridges (ol bridges) and oxolation reactions by the formation of oxo bridges:



The last stage is aging of the solution which involves processes like Ostwald ripening and agglomeration of the colloids in the initial stage.

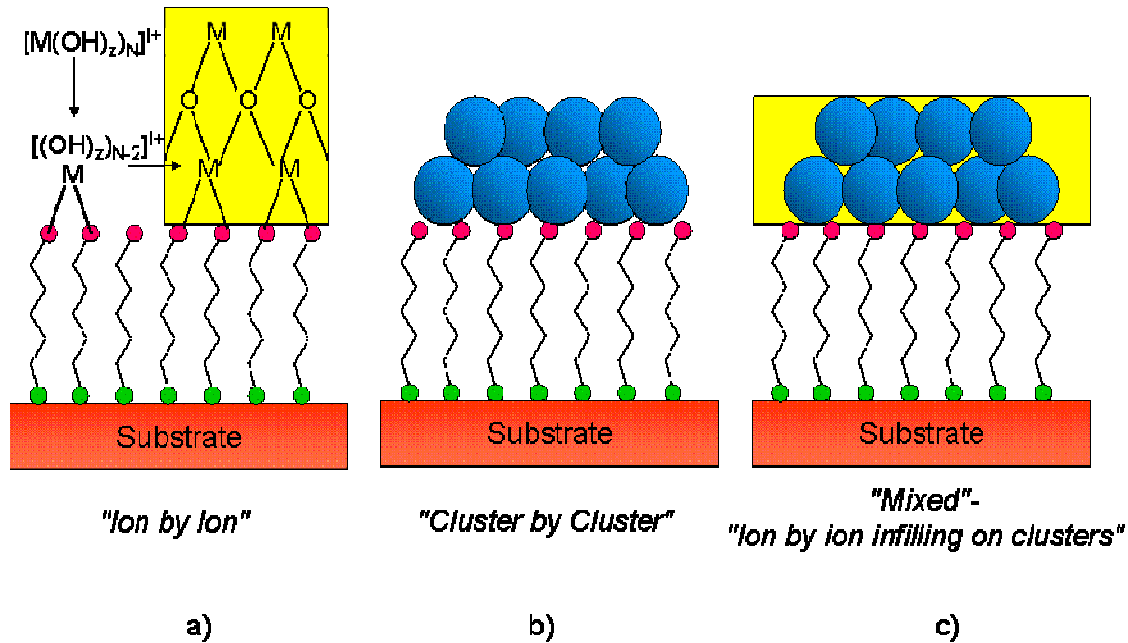


Fig. 2.6 A schematic representation of mechanisms for the formation of thin films a) ion-by-ion; b) cluster-by-cluster; c) mixed [1998 OMc]

Finally, for the deposition of oxide films by CBD two mechanisms or models have been considered [1998 OMc]. The first one is termed ion-by-ion deposition mechanism in which the dissolved ionic species condense at the reacting surface to form the film by heterogeneous nucleation (Fig. 2.6 a). With the second one colloidal clusters are formed in the solution by hydrolysis and condensation of dissolved species and subsequently attach to the substrate surface (termed cluster-by-cluster deposition, Fig. 2.6 b). This mechanism involves homogeneous nucleation in solution. In practice, both of these processes may occur or interact, forming films in which colloidal particles are included into a matrix, which is called mixed mechanism or ion-by-ion infilling on clusters [1998 OMc] (Fig. 2.6 c). The predominance of one mechanism over another is governed by the extent of heterogeneous and homogeneous nucleation.

2.4. Deposition of TiO₂ thin films

TiO₂ thin films have been successfully deposited from organic [2001 MSL, 2002 MJY] or aqueous solvents by LPD [2002 PSS, 2003 YYC], LFD [2002 BHF, 2002 FHN] and CBD [1995 SCD, 2001 NDe, 2005 HBW].

With the CBD technique, TiO₂ films were synthesized by hydrolysis of TiCl₄ (equation 2.6) [1995 SCD], TiF₄ [1999 SIH], a peroxy complex of titanium [2001 NBA] or a titanium lactate complex [1998 BSL]. In these cases, either amorphous or crystalline films are obtained.

The hydrolysis of TiCl₄ leads to formation of oxides according to



Precipitation by thermal hydrolysis of supersaturated solutions of titanium hydroxide can be understood as a series of reactions leading to hydrolyzed TiO₂ via various complexes [1995 SCD]:



The complexes are formed by the replacement of chloride ions by water. Different complexes are formed, such as TiOCl₃⁻, TiOCl₂, TiOCl⁺, TiO(OH)⁺ or [Ti(H₂O)₅OH]³⁺ depending on the acid and titanium concentration in the solution (Fig. 2.7).

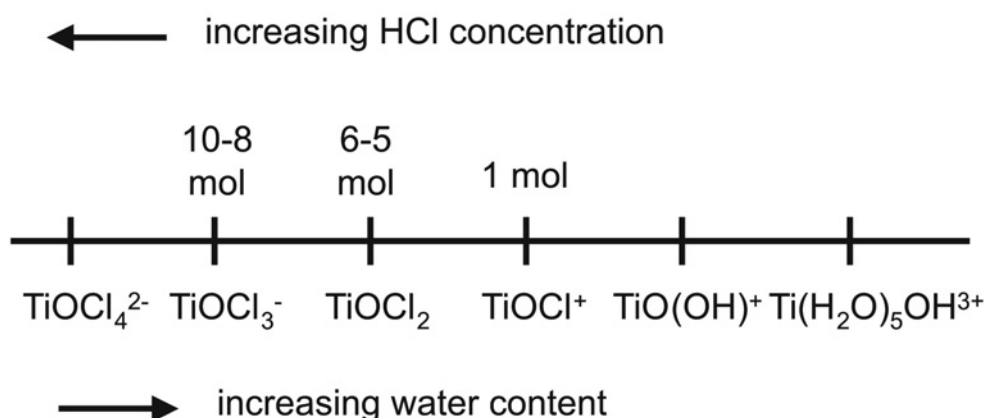


Fig. 2.7 Schematic view of the titanium chloro-complexes formed in hydrochloric solutions of TiCl₄ [1995 SCD]

The deposition of TiO₂ films is carried out in highly acidic solutions at elevated temperatures. Low acidic concentrations lead to immediate bulk precipitation within

the solution while at higher concentrations no film formation is observed [1995 SCD]. If the pH conditions (<1) that are chosen for film deposition are taken into account, the mechanism of the film formation is supported by considering the isoelectric point of the TiO_2 particles, which suggests positively charged colloidal particles and a negatively charged Si- or SAM-terminated substrate surface. The suggested mechanism is also supported and quantified by DLVO (Derjaguin, Landau, Verwey and Overbeck) calculations [1998 SAD] that reveal attractive electrostatic and van der Waals interactions between the particles and the substrate surface. These calculations also predict that the film growth continues due to van der Waals attraction between colloidal particles in the solution and the already deposited film.

The high acidity of the deposition medium might not be compatible with some substrates, like polymers for example, so stabilization of the solution against bulk precipitation was carried out by complexation of titanium with ligands [2001 NBA]. TiCl_4 solutions were stabilized by the addition of H_2O_2 , yielding the peroxo complex of titanium – $\text{Ti}(\text{O}_2)^{2+}$ by side-on coordination of O_2^{2-} to Ti^{4+} . If this approach was applied, titania films were deposited from aqueous solutions of 10mM $\text{Ti}(\text{O}_2)^{2+}$ at 80°C , with a HCl concentration of 0.14M, which is drastically reduced compared to 6M HCl necessary for the deposition of titania films conventionally, at the same deposition temperature [1995 SCD].

2.5. Layer-by-layer deposition of polyelectrolytes

For about 70 years the wet chemical fabrication of thin films has been dominated by the Langmuir-Blodgett (LB) technique, in which multilayers are formed on a water surface and then transferred onto a solid substrate [1997 Dec]. The LB technique requires special equipment and has some limitations with respect to substrate size and topology, as well as film quality and stability. As an alternative to LB films, self-assembly techniques, based mainly on chlorosilanes on oxidized surfaces, were developed from the beginning of 1980s [1983 NSa]. However, self-assembled monolayers based on covalent or coordination chemistry are restricted to certain classes of organics. In any case, high-quality multilayer films were hardly obtained.

A preparative method of thin films that is based on the electrostatic attraction of oppositely charged polyions was originally proposed in the work of Iler [1966 Ile] and extended by Decher et al [1992 DHS]. According to these studies, alternating

adsorptions of cationic and anionic polyelectrolytes leads to the formation of multilayer assemblies which is called layer-by-layer deposition (LbL). This technique has also been applied to functional polymers, bio-polymers and small molecules. In this approach, the fabrication of the films is quite independent on the nature, size and topology of the substrate [1997 Dec].

The practical set-up is extremely simple, e.g. just dipping the support into beakers filled with the polymer solution. The dipping can be done manually, although automatic dipping devices may provide some better process control [1998 YSR]. The method is relatively rapid, as adsorption steps last typically between 1 min and 1 h. Surplus polymer solution adhering to the support is removed by simple washing [2000 BJL].

The basic principle of the layer-by-layer deposition technique of polyelectrolytes is presented in Fig. 2.8. A solid substrate, e.g. positively charged, is immersed in a solution containing an anionic polyelectrolyte and a layer of polyanion adsorbs. After washing with water the substrate is immersed in a solution of a cationic polyelectrolyte and a negative charged polymer layer is formed. By repeating these steps in a cyclical way, multilayer assemblies of alternating polyanions and polycations are obtained.

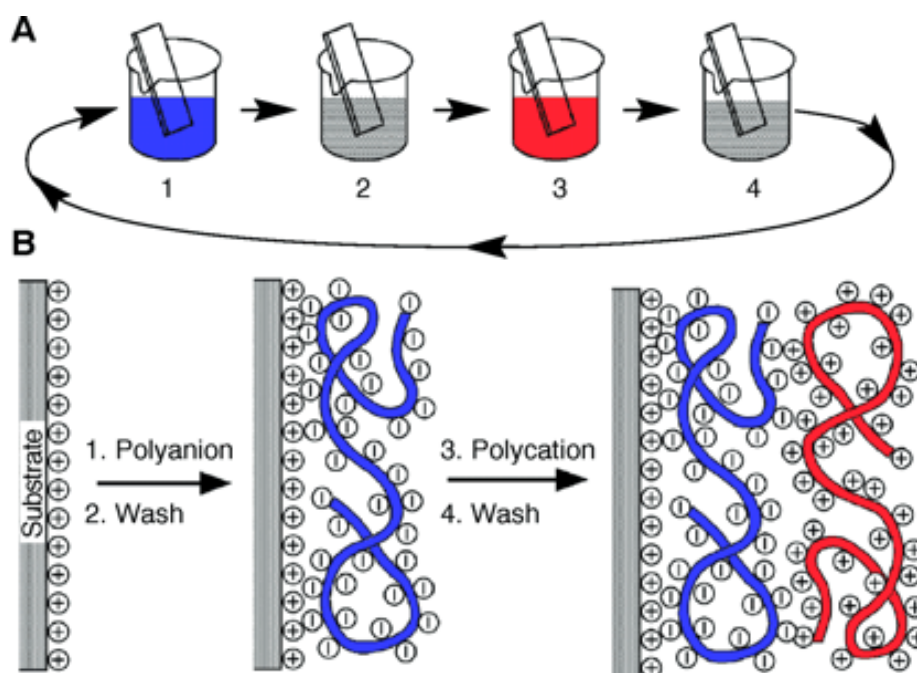


Fig. 2.8 A) Schematic view of the film deposition process using slides and beakers; B) simplified molecular picture of the first two adsorption steps [1997 Dec]

Molar mass effects, pH and ionic strength of polyelectrolyte solutions have an influence on the kinetics of layer formation [2000 BJL]. Films are typically deposited from solution concentrations of several grams per liter, which ensures that the solution does not become depleted during the fabrication of films composed of higher number of layers. One or more washing steps are usually used after adsorption of each layer to avoid the contamination of the next adsorption solution [1996 HSF]. The linear increase of film thickness with the number of deposited layers is often similar even for different substrates, which makes the film properties independent of the substrate. The thickness of each individual layer, as well as the film density and in some cases the film roughness can be increased by changing the ionic strength of the adsorption solution by addition of the salts (NaCl, NaBr, $MnCl_2$) [1996 LAO, 2000 KBe]. Addition of salt can cause changes in the polymer chain conformation from flat to coiled, which can increase the layer thickness and surface roughness [1999 KFJ, 2000 RLS].

Mostly used polyelectrolytes are commercially available ones, like poly(ethylenimine) [1997OLA, 1999 LAO, 2002PCI], poly(allylamine) [1995 RLD, 1997 CMc, 1999 LAO], poly(diallyldimethylammonium chloride) [1999 SEW, 2000 BKA], poly(styrene sulfonate) [1995 RLD, 1997 CMc, 2000 KTi], poly(vinylsulfate) [1993 LDM], (poly [N - vinyl - (4 - (3' - carboxy - 4' - hydroxy - phenylazo) benzenesulfonamide)] ('PAZO')) [1994 DLS] and poly(acrylic acid) [1996 HSF, 2001 IOS, 2003 THa]. The most studied system so far has been poly (allylamine) and poly(styrene sulfonate). More complex, functionalized polyelectrolytes have been employed much less frequently, and they are often chosen to exploit particular properties, to induce formation of patterned coatings, or to enable secondary chemical modifications [2000 BJL].

In addition to the preparation of uniform and homogeneous coatings from various polymers, polyelectrolyte layers are applied for compatibilization and protection of surfaces, sensors, separation membranes, conducting, light-emitting or photovoltaic devices, modified electrodes, magnetic films and controlled particle and catalyst preparation [2000 BJL].

3. Experimental methods

3.1. Film deposition

3.1.1. Substrate preparation

For substrates, p-type (100) single-crystal Si wafers (Wacker, Silitronic AG), 10x10 mm² in size, polished on one side, were used. The wafers were cleaned in acetone and ethanol using a fresh tissue and solvent. They were then oxidized in piranha solution (70vol% of conc. H₂SO₄, 30vol% of 35% H₂O₂ aqueous solution) for 20 min at 80°C, thoroughly washed with distilled water and blow dried in an argon stream.

3.1.2. Deposition of polyelectrolyte layers

Sodium poly(styrenesulfonate)-PSS (molecular weight $M_w = 70000$ g/mol), polyethyleneimine-PEI (M_w 70000) and poly(allylaminehydrochloride)-PAH (M_w 60000) (Fig. 3.1) were obtained from Aldrich, Germany. PEI was dissolved in distilled water in a concentration of 1.25 g/dm³, while PSS (4 g/dm³) was dissolved in 0.5 M aqueous solution of MnCl₂ and PAH (2 g/dm³) in 1 M aqueous solution of NaCl. The pH of the solutions was adjusted by adding 1 M HCl to pH 9 for PEI and pH 3.5 for PSS and PAH.

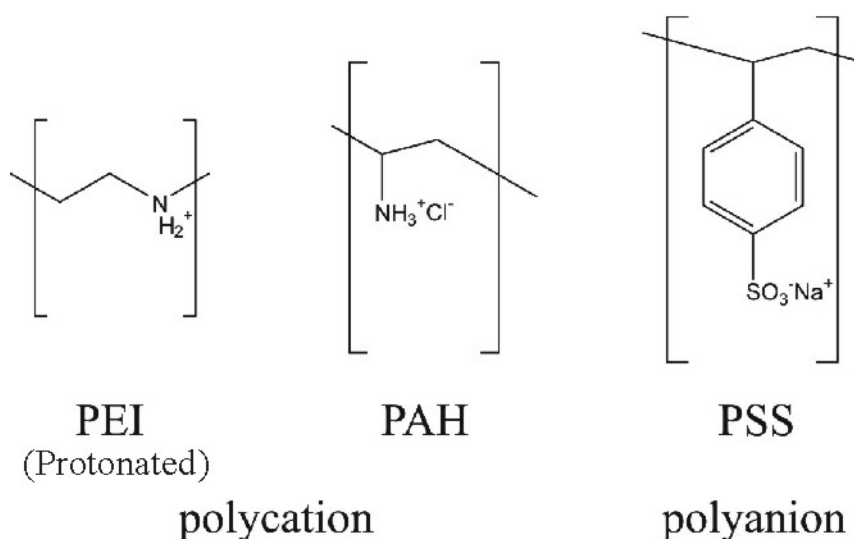


Fig. 3.1 The chemical structure of the polyelectrolytes: polyethyleneimine - PEI, poly(allylaminehydrochloride) - PAH and sodium poly(styrenesulfonate) - PSS

The adsorption was carried out by horizontal immersion of wafers into the solutions of the polyions at room temperature for 20 min. Intermediate washing was performed for 5 min with gentle shaking in distilled water after each deposition step. In the first step of deposition, a positively-charged surface was formed by adsorption of PEI on silicon, since PEI gives good covering of oxidized surfaces [1993 LDM, 1997 Dec]. After washing in water, the sample was treated with PSS to build alternately charged multilayer structures. In the next adsorption cycle, the sample was treated with PAH, then again with PSS, so that a multilayer structure $(\text{PEI/PSS})_1(\text{PAH/PSS})_{n-1}$ was obtained. The final layer was always PSS.

3.1.3. Deposition of TiO_2 layers

TiO_2 films were deposited on unmodified and polyelectrolyte-coated Si wafers from an aqueous solution of the Ti-peroxo complex $(\text{Ti}(\text{O}_2)^{2+})$ in the presence of HCl. For the preparation of the $\text{Ti}(\text{O}_2)^{2+}$ solution, freshly distilled TiCl_4 (82.07 mmol; Fluka) was added dropwise to an ice-cooled aqueous solution of 35 vol% H_2O_2 (164.1 mmol; Merck). Stock solutions for the film deposition were prepared from 10 mM $\text{Ti}(\text{O}_2)^{2+}$ and 7.5-160 mM HCl, depending on the reaction temperature (40 – 90°C). Each reaction temperature demands optimization of the acidity of the solution, i.e. higher deposition temperatures demands higher amounts of added HCl. Insufficient acid concentration lead to visible bulk precipitation during deposition and with use of too high acid concentration there is no film deposition.

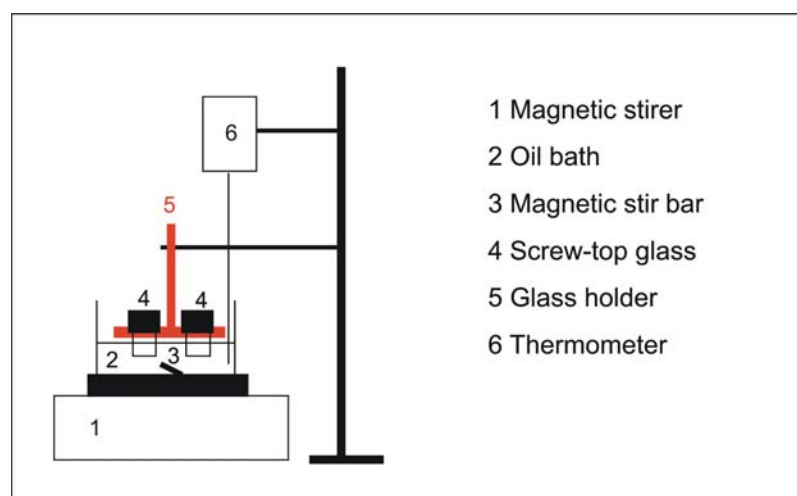


Fig. 3.2 Experimental set-up for the static deposition (SD) technique

The deposition was performed in two ways:

In static deposition experiments substrates were immersed in horizontal position in 10 ml aliquots of the reaction solution (covered glass chamber) and placed in an oil bath (Fig. 3.2)

For the liquid flow deposition (LFD) a reaction solution was transported by a peristaltic pump (ISMATEC Reglo Digital 2 Kanal) through the water heated reaction chamber (7.5 cm in length x 2.5 cm in diameter) (Fig. 3.3). With ca. 5 mm depth of the reaction solution, there is a volume of ca. 10 ml, similar to the volume used in static deposition experiments. Substrates were laid horizontally on a hemicylindrical teflon bar which reduces the chamber volume and improves the flow profile of the liquid inside. The temperature was monitored by a thermocouple (NiCr-Ni) placed in the vicinity of the substrate and the flow rate (1.5 ml/min) was controlled by adjusting the speed of both pumps.

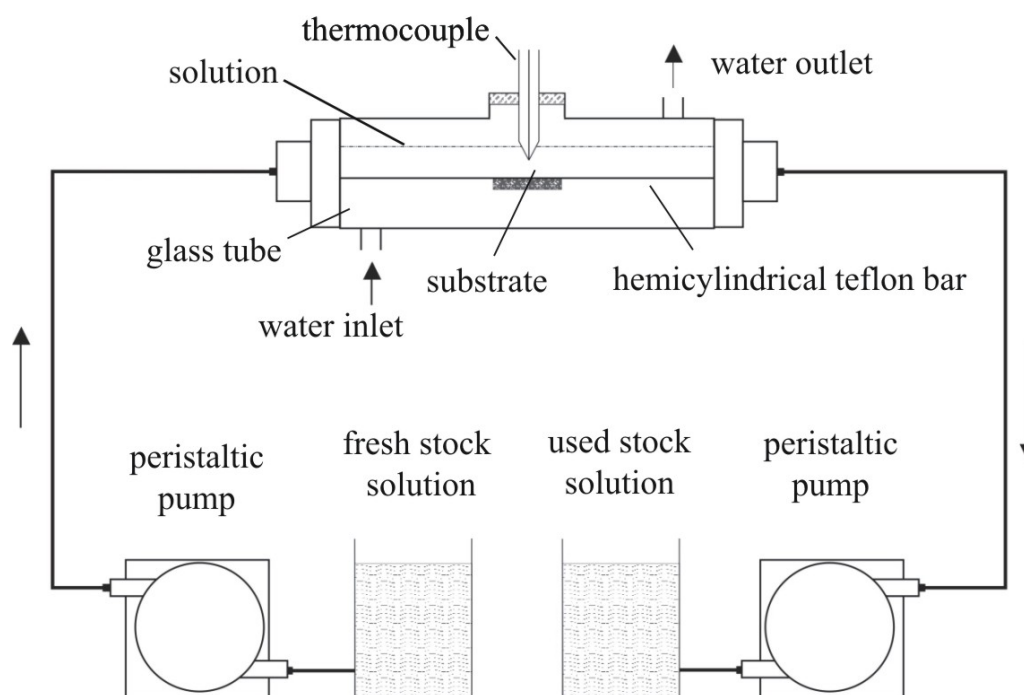


Fig. 3.3 Experimental set-up for liquid flow deposition (LFD) technique

In both techniques, after the deposition the samples were removed from the deposition chamber, rinsed with distilled water, cleaned ultrasonically in distilled water for 3 min to remove any loosely adherent particles and blow dried in an argon stream.

3.1.4. Deposition of PE/TiO₂ multilayers

Composite PE/TiO₂ films were synthesized by sequentially applying the layer-by-layer deposition technique for the deposition of the PE layers and the static deposition techniques for the synthesis of TiO₂ layers (Fig. 3.4).

TiO₂ films were deposited from an aqueous solution of 10 mM Ti(O₂)²⁺ and 30 or 45 mM HCl at 60°C for 2h. For deposition of PE layers, PSS and PAH were deposited from salt solution (0.5 M MnCl₂ for deposition of PSS and 1 M NaCl for deposition of PAH). There was no additional cleaning of PE surface before deposition of TiO₂.

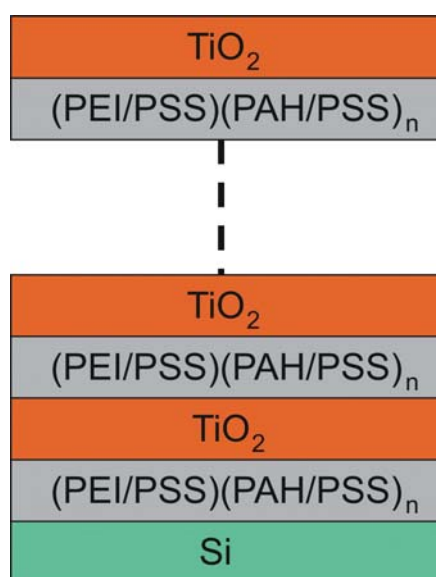


Fig. 3.4 Preparation of the PE/TiO₂ multilayer films on a Si substrate by consecutive adsorption of PE layers by the LbL deposition and TiO₂ films by the SD

3.1.5. Thermal treatment

Samples were annealed at 500°C for 2 h in air in a furnace (heating rate 25°C/h, cooling rate 25°C/h).

3.2. Characterization methods

3.2.1. Auger electron spectroscopy (AES)

The multilayer film composition as a function of depth of the layer was determined by AES depth profiling. To this end, Ti LMM, Si KLL, O KLL and C KLL peaks were recorded with a JAMP-7830 scanning Auger electronic microscope using a primary electron beam of 10 kV and 11 nA, an analysis area of $10 \times 10 \mu\text{m}^2$, and employing a sputter interval of initially 20s, and subsequently 60s (1 kV Ar^+ beam with a beam current of 170 nA; $300 \times 300 \mu\text{m}^2$ raster). For quantification, the linear least squares fitting procedure in the Phi Mulipack software package was used, while employing the peak-to-peak heights of the differentiated spectra in combination with the appropriate sensitivity factors for Ti, O, C and Si, as given by the manufacturer.

3.2.2. Atomic force microscopy (AFM)

The surface topography images were recorded by using a Digital Instruments Nanoscope III applying the tapping mode with silicon cantilevers, and a scan rate of 0.5 Hz. The thickness of the organic layers was measured applying AFM, by scratching the film with a sharp needle and measuring the depth of obtained scratch on $10 \times 10 \mu\text{m}^2$ scanned surface area. All scans were taken in air, at room temperature. Before AFM examination, specimens were cleaned ultrasonically in water and dried in an argon stream.

3.2.3. X-ray diffraction (XRD)

The structure of TiO_2 films was investigated by XRD using a Panalytical XPert MPD θ/θ -diffractometer with Bragg-Brentano geometry (equipped with a graphite monochromator in the diffracted beam to select CoK_α radiation with a wavelength 1.789 Å). The XRD patterns were recorded in the range of $2\theta = 10 - 60^\circ$. Besides this technique, a grazing incidence geometry with the incident angle of 2° was also applied for 2θ scans, using a Bruker diffractometer (equipped with a graphite monochromator in the diffracted beam to select CuK_α radiation).

3.2.4. Scanning electron microscopy (SEM)

SEM studies on the surface morphology of the film were performed with a JSM – 6300F scanning microscope using an acceleration voltage of 3 keV. For evaluation of film thickness by taking cross-sectional scanning electron micrographs of the film, the samples were cleaved by an edge-cutter. The film thickness was estimated using a Image-Tool program.

Cross-sectional imaging of multilayer films was performed DSM 982 Gemini scanning electron microscope using an acceleration voltage of 5 keV. The specimens were cleaved by an edge-cutter and mechanically polished using SiC abrasive-paper and diamond paste.

3.2.5. Transmission electron spectroscopy (TEM)

High resolution TEM studies were performed on a JEOL 4000EX microscope operated at 400 keV with a point resolution of 0.175 nm.

The analytical investigations (EELS and EDX) were carried out in a VG HB 501 UX scanning transmission electron microscope (STEM) operated at 100 keV. This microscope is equipped with a cold-field emission electron source and with a parallel EELS detector (Gatan UHV Enfina system). The Ti-L_{2,3} and the O-K edges were acquired using a dispersion of 0.1 eV/channel and with acquisition times between 10-20 sec. All data were corrected for dark current and detector channel gain variation. The pre-edge background was extrapolated using a power law function and subtracted from original data. The spectra were recorded using the beam scanning an area of about 3 nm x 4 nm or 6 nm x 8 nm.

Energy dispersive X-ray spectroscopy (EDS) is a valuable tool for qualitative and quantitative element analysis. The characteristic peaks which appear due to x-rays emitted when ionized atom return to the ground state. Each element has characteristic peak positions corresponding to the possible transitions in its electron shell.

EELS in the TEM enables a local analysis from plasmon losses and ionization edges of inner-shell ionization with energy-loss near-edge structures (ELNES) and extended energy-loss fine structures (EXELFS). The characteristic edges enable the qualitative analysis of chemical elements and the edge intensity can be related to the amount of

the element present. ELNES is due to transitions of electrons from a particular core level to the lowest unoccupied states in the solid and is dependent on details of the local atomic environment such as co-ordination, valence and the type of bonding. The identification of an edge in EEL spectrum is less routine compared to the EDS, because the edges can have a variety of shapes. The edges in the EEL spectrum are due to the ionization process. The K-shell electron is in the 1s state and it leads to a single K edge. The electrons in the L shell are in 2s or 2p orbitals. The L_1 edge is present when a 2s electron is ejected and a 2p electron causes either a L_2 or L_3 edge. Sometimes the L_2 and L_3 edges may not be resolvable and we call the edge $L_{2,3}$. The nomenclature $L_{2,3}$ is due to the fact that the electron was ejected from the L shell, which has different energy levels. Such separation of the core state energies is called spin-orbit splitting [1996 WCa].

3.2.5.1. Preparation of cross-sectional TEM specimens

The samples investigated by cross-sectional TEM were prepared in the following way, using the care in order to minimize thermal exposure of the organic layer in the multilayer film:

1. A Si/multilayer sample ($10 \times 10 \text{ mm}^2$), was cleaved by an edge-cutter into two pieces with a width of about 2.5 mm (Fig. 3.5 a). Cleaving the sample prevents damaging of the original sample surface which may occur by sawing the sample.
2. Two sample slices were glued together. The glue (Gatan G1) was stabilized in an oven at 70°C for 2h thereby obtaining a sandwich structure (Si/multilayer/glue/multilayer/Si) (Fig. 3.5 b). It was important to use an epoxy-glue which is stabilized at low temperatures (below 100°C), in a short time (about 2 h), in order to minimize the time during the organic film is exposed to elevated temperatures. Subsequently two pieces of silicon were glued on the same way to both side of the sandwich in order to reach 2.5-3 mm in size of all cross-section. The sandwich is then sliced with a wire saw into slices of about 0.8 mm thickness (Fig. 3.5 c).
3. The 0.8 mm thin slices were fixed with wax on a steel sample holder. The slices were ground and polished on one side using a Gatan model 623 Disc grinder, to a final thickness of $\sim 100 \mu\text{m}$ (Fig. 3.5 d). As grinding and polishing implies fixing the slice with a thin layer of wax on each side, in this step attention should be pay on

quickly fixing specimen on the sample holder which is kept at 130°C in order to melt the wax. The amount of acetone used to remove the wax should be minimized, since acetone can dissolve the organic layer.

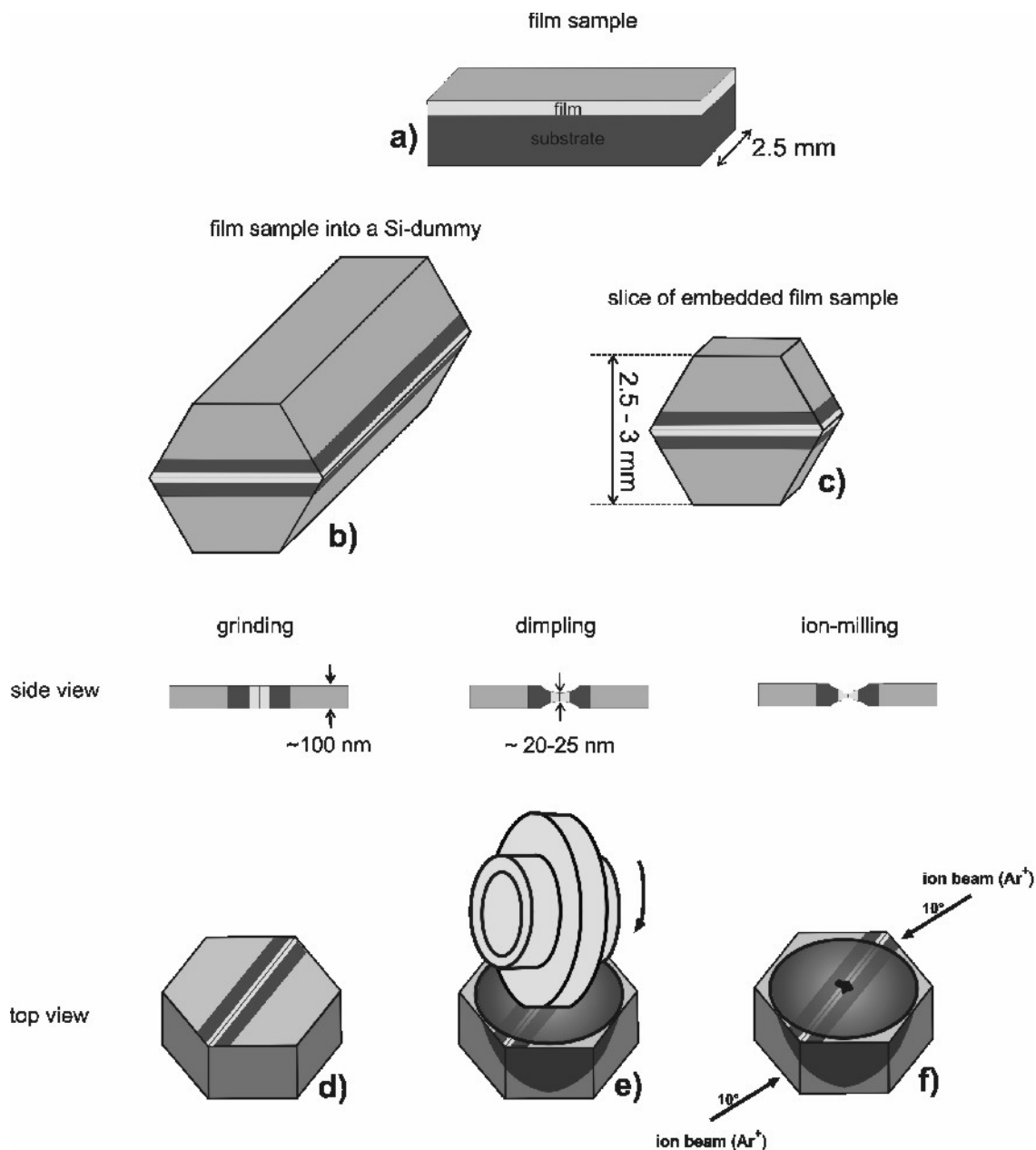


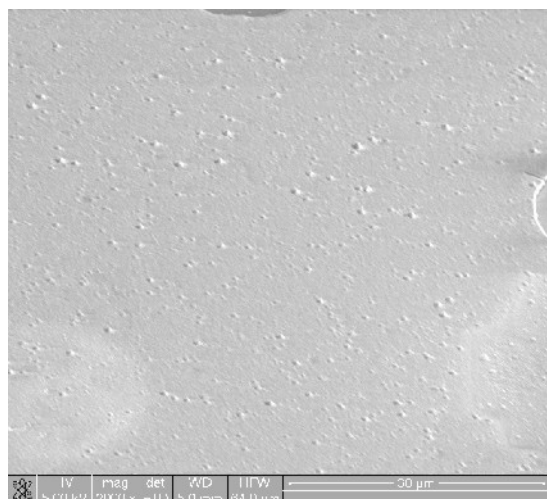
Fig. 3.5 Steps in the conventional preparation of cross-sectional TEM specimens: a) cleaved sample (10x2.5 mm²); b) the sample embedded into a Si-dummy; c) slice of the embedded sample; d) sample grinding; e) sample dimpling; f) ion-milling

4. The bottom side of the specimen was further dimple-ground and polished using a Gatan model 656 Dimple Grinder to a thickness $\leq 15 \mu\text{m}$ which is revealed on the Si substrate by a dark red transparency (Fig. 3.5 e).

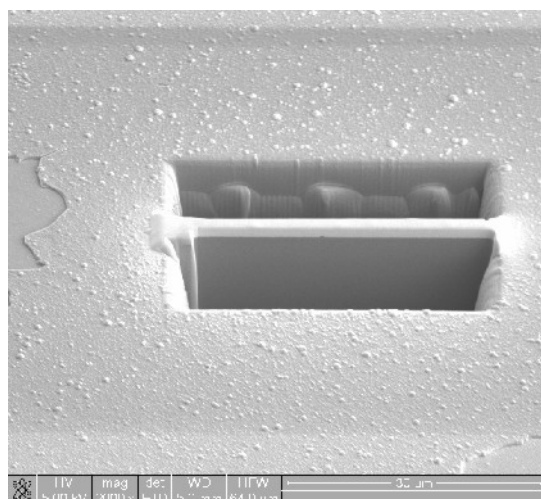
5. For the final thinning step, the specimen was glued on a copper ring (3 mm diameter) to increase the stability and to protect specimen from mechanical damaging during further handling. The specimen was thinned by a Gatan Duo 691 precision ion-milling machine which operated at 4 keV, 1 mA, and at an incident angle of argon ions of 10° in the double sector thinning mode. During the whole ion-milling process the specimen is cooled by liquid nitrogen until a hole is formed in the center. At this point the edges of the hole are transparent for electrons (10 – 100 nm) (Fig. 3.5 f).

3.2.5.2. Focused ion beam (FIB) preparation of cross-sectional TEM specimens

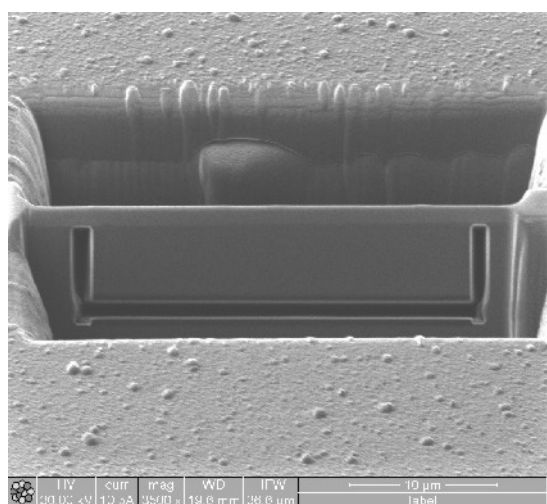
The FIB TEM sample preparation has become an interesting alternative to conventional TEM sample preparation. The FIB technique is an efficient method which allows fast site-specific preparation of TEM specimens. In these studies a dual beam FIB/SEM instrument (FEI NovaTM 200) with a Ga⁺ ion source was used for the preparation of cross-sectional specimens. Since the size of the TEM lamella should be reasonably kept below 30 μm length, the area of interest had to be chosen carefully (Fig. 3.6 a). The TEM lamella was cut out using the FIB at 30 keV beam energy (Fig. 3.6 b,c). Using an in situ micromanipulator, the samples were lifted out (Fig. 3.6 d) and fastened to a TEM grid (Fig. 3.6 e). The specimen was subsequently coated with a protective Pt layer and thinned to a wedge-shaped lamella with regions of <100nm thickness (Fig. 3.6 f). To reduce the thickness of the amorphous damage layers a final thinning and polishing step at 5 keV ion beam energy was carried out. Using FIB microscopy and in situ sample preparation we have succeeded in preparing a thin TEM specimen where the area of interest was situated in the thin part of the lamella. The main advantages of using the FIB for the preparation of TEM samples are high accuracy and shorter preparation time compared to conventional ion-milling techniques.



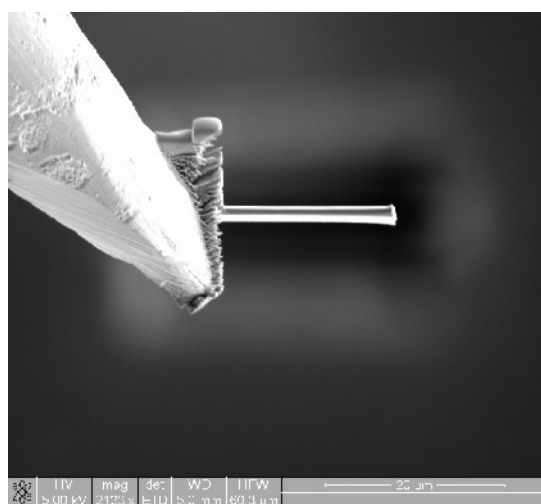
a)



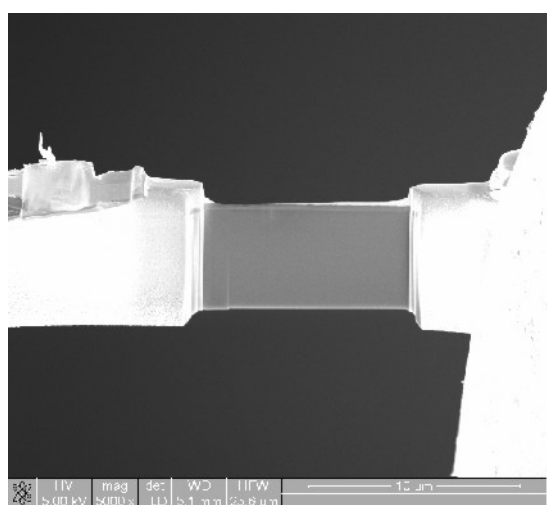
b)



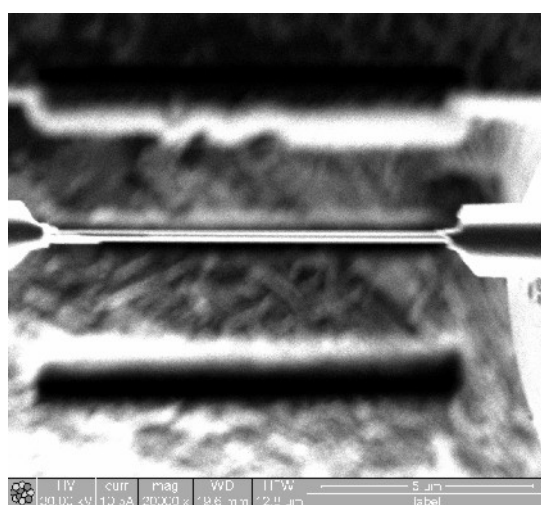
c)



d)



e)



f)

Fig. 3.6 Steps in the FIB preparation of cross-sectional TEM specimens: a) choosing a homogeneous area; b, c) cutting of a lamella; d) lifting out of the lamella with a micromanipulator; e) fastening to a TEM grid; f) thinning to a wedge-shaped lamella (~100 nm thickness)

3.2.5 Quartz crystal microbalance (QCM) measurements

Quartz crystal microbalance (QCM) is well known as a very sensitive mass sensor, where the resonant frequency of a quartz crystal changes according to the amount of deposited mass [2000 BKA]. This operation is based on the piezoelectric effect of a quartz crystal which has an oscillating resonant frequency proportional to its thickness. Fig. 3.7 shows a schematic picture of the QCM. Research Quartz Crystal Microbalance (RCQM) and crystals were purchased by Maxtek Inc. The diameter of QCM crystals is 24.5 mm and the gold electrodes and SiO₂ coatings which cover the quartz crystal have diameter 9.5 mm. The quartz crystal operates at 5 MHz. The oscillation frequency is measured with a frequency counter which is connected to a personal computer for data acquisition and monitoring with special Data-Log software (Maxtek Inc.).

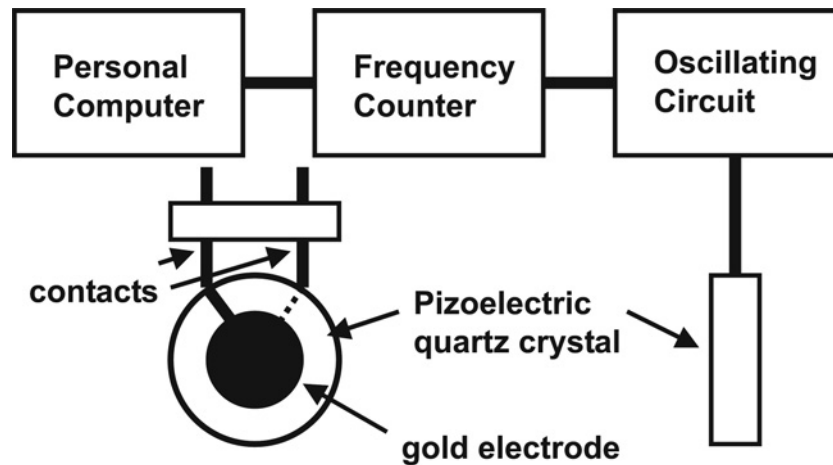


Fig. 3.7 Schematic picture of the QCM set-up [2000 BKA]

Due to the piezoelectric properties of the quartz crystal, its oscillation frequency (ΔF) changes proportionally to the mass (Δm) deposited onto the crystal surface. This relationship which can be expressed by Sauerbrey's equation [1959 Sau]:

$$\Delta F = \frac{-2F_q^2}{A\sqrt{\rho_q\mu_q}} \Delta m \quad (3.4)$$

where F_q is the fundamental resonant frequency of the QCM (5×10^6 Hz), A is the mass sensitive electrode area (0.3165 cm^2), ρ_q is the density of the quartz (2.65

g/cm^2) and μ_q is the shear modulus of the quartz ($2.95 \times 10^6 \text{ N/cm}^2$). Applying this equation it is possible to obtain the adsorbed mass from the change of the resonant frequency of the quartz crystal:

$$\Delta m(\mu\text{g} / \text{cm}^2) = -1 \times 10^{-5} \Delta F(\text{Hz}) \quad (3.5)$$

From the adsorbed mass the film thickness is derived using a density value of the deposited film.

The measurements of PE multilayer growth were carried out at room temperature in a vessel with the quartz crystal, placed at its bottom. For each measurement, 10 ml of the PE solution is dropped into the vessel with a help of the pipette. After 20 min, the solution was moved and an intermediate washing was performed with distilled water for 5 min.

3.2.6 Nanoindentation

The study of the mechanical properties of oxide single layers as well as multilayer nano-composite films is an area still in infancy. This is largely due to the fact that the traditional methods used to evaluate mechanical properties of bulk materials are often not applicable for this purpose. In this context, novel perspectives are opened by the recent progress made in the further development of mechanical characterization techniques [1996 VVI] such as depth-sensing nanoindentation testing [1986 DNi, 1992 OPh] or microbridge tests [2000 ZSQ].

Among these, as the simplest and most direct way of testing is nanoindentation which attracted strong attention in recent years [1997 Nix, 2000 OBJ, 2004 CLR, 2004 OPh]. It employs high resolution sensors and actuators to continuously control and monitor the loads and displacements on a nano-sized indenter relative to the surface as it is driven into and withdrawn from the material. A typical load (P) – displacement (h) curve recorded during an indentation experiment is shown in Fig. 3.8 a) quantities are the peak load (P_{max}), the maximum depth (h_{max}), the final or residual depth after unloading (h_f) and the slope of the upper portion of the unloading curve ($S = dP/dh$), the so-called contact stiffness. A schematic representation of a cross-section of an indent during indentation is presented in Fig. 3.8 b).

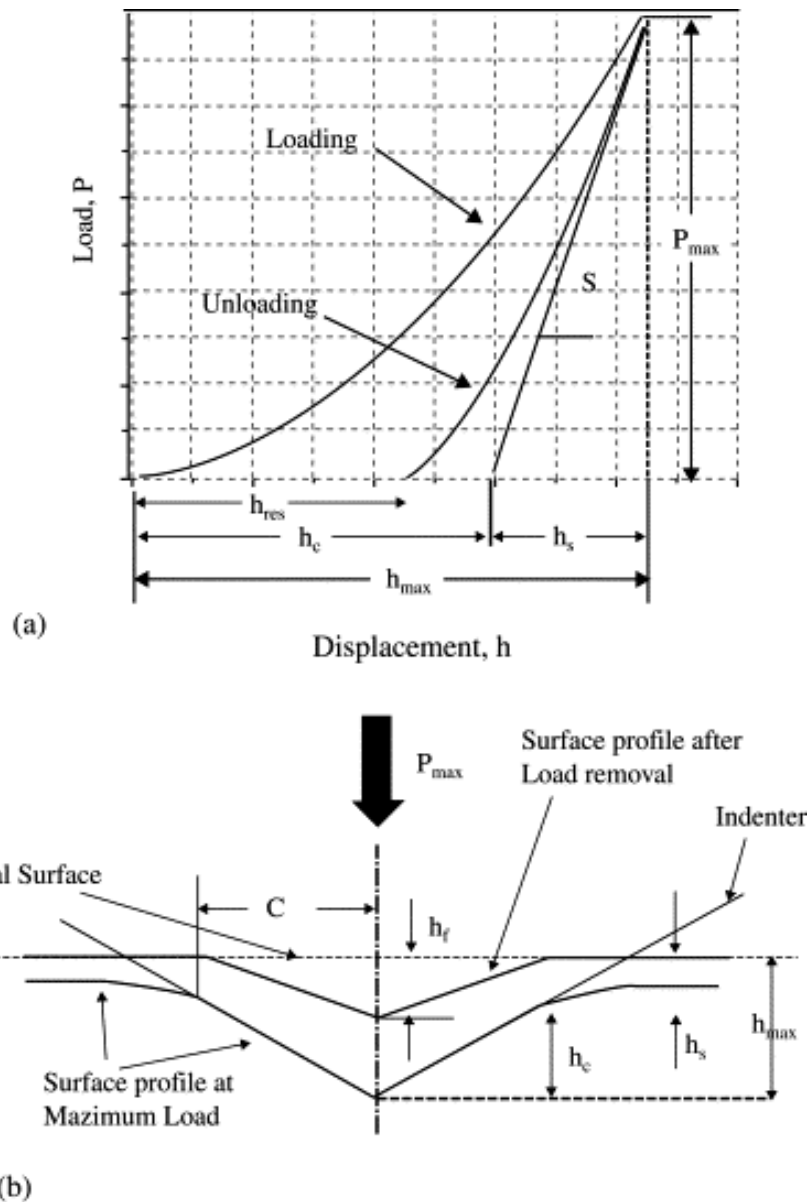


Fig. 3.8 a) A schematic illustration of a load-displacement curve and b) cross-section of an indent during indentation [2004 CLR]

While the loading curve characterizes the resistance of the sample against the penetration of the tip into the material and reflects both the plastic and elastic properties of tested materials, the unloading curve is mainly determined by elastic recovery of material during indenter withdrawing.

One great advantage of the nanoindentation technique is that in principle various mechanical properties can be determined from the indentation load-displacement data. Routinely it is employed to evaluate the hardness and Young's modulus.

The fundamental relations from which hardness and Young's modulus are determined are

$$H = \frac{P_{\max}}{A_c} \quad (2.8)$$

and

$$E_r = \frac{\sqrt{\pi}}{2} \cdot \frac{S}{\beta \cdot \sqrt{A_c}} \quad (2.9)$$

respectively, where H is the hardness, P_{\max} the load and A_c the projected contact area of the load, E_r the reduced Young's modulus, β a constant that depends on the geometry of the indenter and S the contact stiffness.

If the shape of the tip is known, the contact area A_c can be determined as a function of contact depth h_c ($A = f(h_c)$), where

$$h_c = h_{\max} - h_f = h_{\max} - \varepsilon \cdot \frac{P_{\max}}{S} \quad (2.10)$$

h_{\max} is the maximal contact depth, h_f the final depth after complete unloading and ε a constant that depends of indenter geometry.

A variety of procedures have been developed for extracting these quantities from load-displacement curves and the geometry of the indenter. The procedure proposed by Oliver and Pharr [1992 OPh], which is most frequently followed, pertains to indentation with the three-sided pyramidal Berkovich indenter. A major limitation of this method arises from the fact that it relies heavily on the accurateness of a calibration process, and it does not incorporate details of the indentation shape which may be affected by pile-up or sink-in. Moreover, in the case of indentation testing of thin coatings, this procedure does not account for the elastic mismatch effects caused by the substrate, such that only the combined properties of the film and substrate are obtained. Reliable results can therefore be obtained only for films that show no pile-up effect and minimal elastic mismatch between the film and the substrate.

Nanoindentation testing was performed with a scanning nanoindenter consisting of a depth-sensing force transducer (Hysitron TriboScope) combined with a commercial scanning probe microscope (NanoScope III Multimode, Digital Instruments). A cube corner diamond indenter with a nominal tip radius of ~40nm was used. The high load and displacement resolution (100nN and 0.2 nm, respectively) of the force transducer allowed working with very shallow indentation depths. All indentations were made by applying the maximum force of 150 μ N, which was chosen in order to reach a maximum penetration depth of about 150 nm. The indentation force was varied during subsequent load/partial unload-cycles over 25 steps at the same location, with automatic recording of the indentation depth after each step. For each specimen, the results were averaged over fifteen indentations made at different locations. Tip calibration was performed utilising a fused silica standard sample within the penetration depth range of up to 150 nm.

Before the measurements, the samples were aged in a close box (with air circulation) for 1 month.

4. Results and discussion

4.1. Deposition of TiO₂ films

The present chapter describes the deposition of TiO₂ films from an aqueous solution of the titanium-peroxo complex in the presence of HCl on unmodified Si substrates by the liquid flow technique. This new deposition technique will be considered in comparison with the static deposition. Microstructure and morphology of the obtained films were characterized by means of SEM, AFM, XRD in order to establish the optimum parameters of the reaction process with respect of the film homogeneity, thickness and surface roughness.

4.1.1. Liquid flow vs. static deposition

TiO₂ thin films were deposited on unmodified Si substrates applying acidic aqueous solutions (30 mM HCl) of 10 mM Ti(O₂)²⁺ at 60°C by the liquid-flow deposition technique (LFD) and the static deposition technique (SD) with and without changing reaction solution during the deposition process every 2 h.

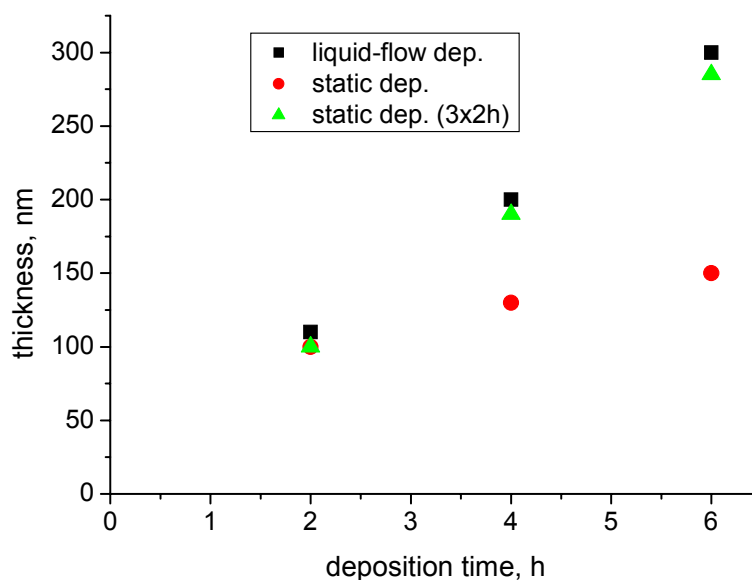


Fig. 4.1 Dependence between the film thickness and the deposition time for the TiO₂ films deposited on a Si substrate from an aqueous solution of 10 mM Ti(O₂)²⁺ and 30 mM HCl at 60°C by: (■) LFD, (●) SD and (▲) SD with changing the reaction solution (3x2h)

It can be seen (Fig. 4.1) that the film thickness increases linearly with time in the range of 2-6 h for films deposited by LFD (growth rate about 47 nm/h, Fig. 4.1). Nearly the same results were achieved by SD (growth rate about 46 nm/h, Fig. 4.1) with changing of the reaction solution, whereas without changing the solution the growth rate is parabolic and much less at a given deposition time.

The obtained results show that the SD technique can substitute the LFD procedure, if the reaction solution is renewed in appropriate time intervals. Recent investigations showed, that further reduction of the exchange interval to 1.5 h or 1 h for the films deposited by the SD from an aqueous solution of 10 mM $\text{Ti}(\text{O}_2)^{2+}$ and 40 mM HCl at 60°C had only a slight effect on the film thickness [2005 Röh].

In comparison, the thickness i.e. growth rate of the films deposited by SD without changing reaction solution after 2 h of deposition is decreased with increasing deposition time. This can be attributed to the aging of the reaction solution and the reduction of concentration of precipitating species. According to Agarwal et al., who investigated ZrO_2 films deposited by the SD without changing reaction solution, these kinetics results from film growth involving deposition and aggregation of nanosized 'primary' particles, produced and present in the solution. Due to their small size, these particles have a high tendency to aggregate in the solution. The film formation occurred through adhesion of these nanoparticles to the substrate. During the deposition process, the number density of these primary particles decreased, their aggregation rate was lower, which caused poorer adhesion of the larger precipitates to the substrate. The film growth rate then decreased with time [1997 ADH].

4.1.2. Influence of the film thickness on the film roughness

The topography of the TiO₂ films deposited by the LFD technique on Si substrates at 60°C from an aqueous solution of 10 mM Ti(O₂)²⁺ and 30 mM HCl for 2 h, 4 h and 6 h was investigated by AFM. The thickness of the deposited films, determined from SEM cross-sections (see chapter 4.4.4), was 110, 200 and 300 nm, respectively. The corresponding AFM images are presented in Fig 4.2.

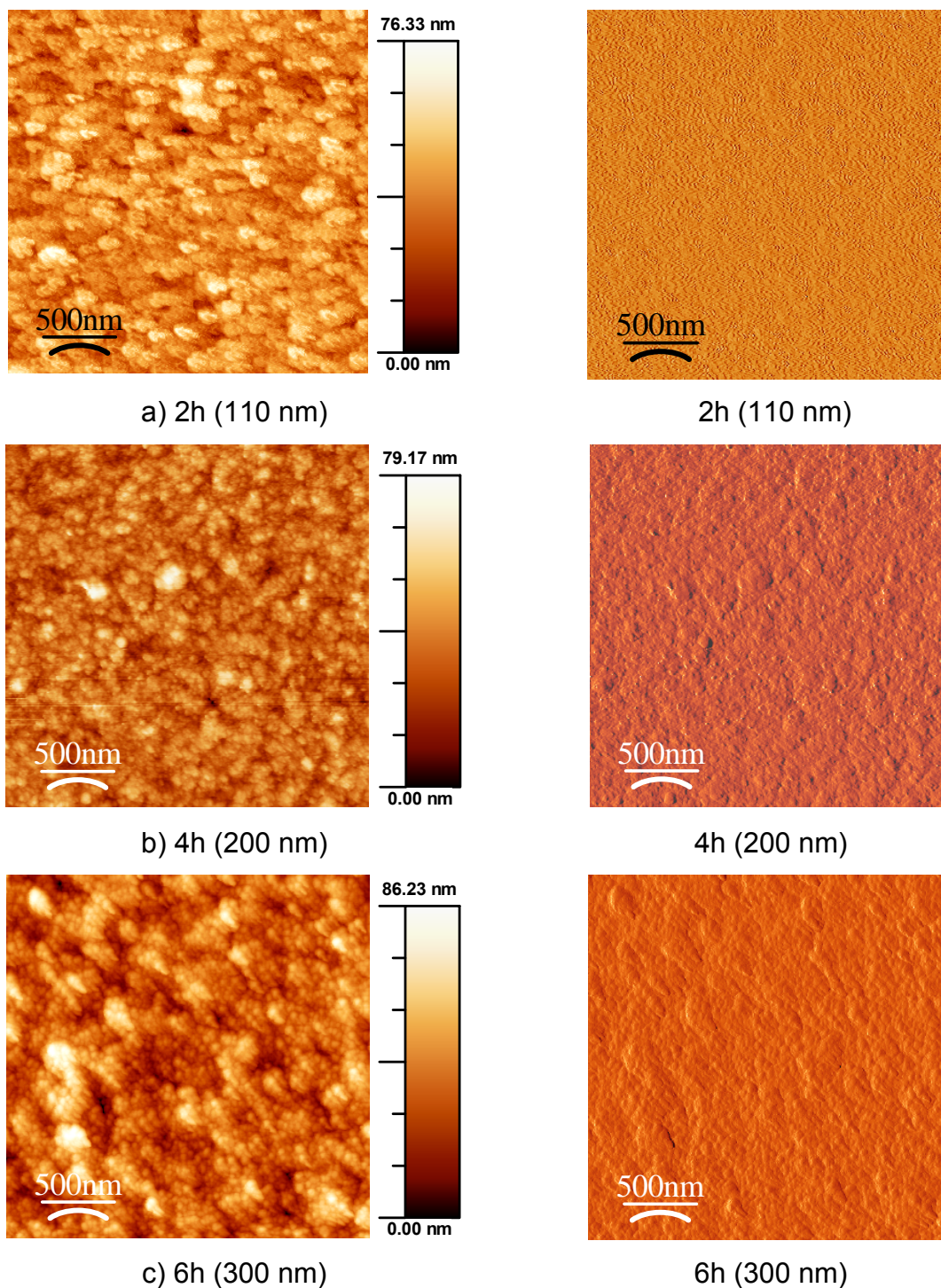


Fig. 4.2 AFM topographic (left) and corresponding deflection mode images (right) of TiO₂ films deposited on a Si substrate from an aqueous solution of 10 mM Ti(O₂)²⁺ and 30 mM HCl at 60°C by the LFD for: a) 2 h (film thickness 110 nm); b) 4 h (200 nm); c) 6 h (300 nm)

The images reveal a dense packing of agglomerates that are ~100 nm in width for the 110 and 200 nm thick films and ~150 nm for the 300 nm thick films. The height variations of the deposited films are 76, 79 and 86 nm and the surface roughness is 8.0, 10.8 and 12.5 nm, respectively.

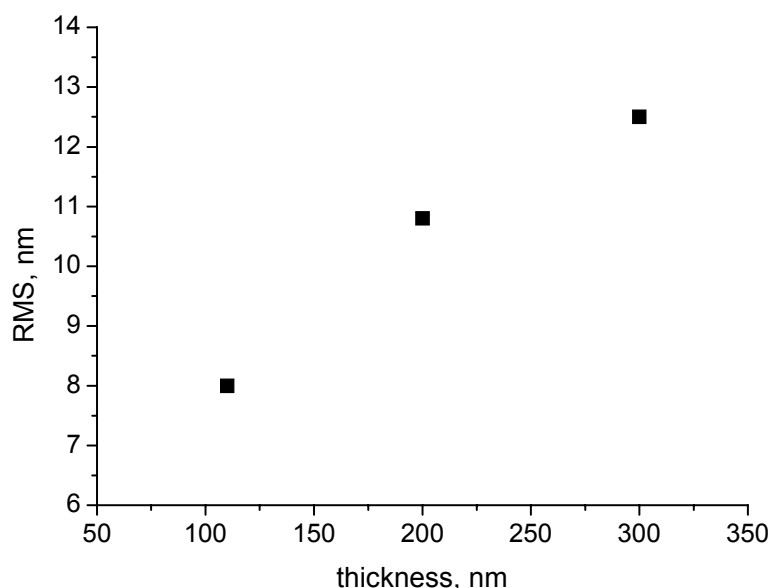


Fig. 4.3 Dependence between the surface roughness and the film thickness for TiO₂ films deposited on a Si substrate from an aqueous solution of 10 mM Ti(O₂)²⁺ and 30 mM HCl at 60°C by the LFD

In general, the film roughness is mainly determined by the size of the aggregated colloidal titania particles which are discernable from the topographic AFM images. The surface roughness increases with increasing thickness of the films (Fig 4.3), which is consistent with preferred deposition of the next particle on already deposited ones. This increase was also observed for TiO₂ films deposited by the SD on a Si at 60°C from an aqueous solution of 10 mM Ti(O₂)²⁺ and 35 mM HCl [2005 HBW]. Moreover, investigations of TiO₂ films deposited by the SD with changing the reaction solution on a Si at 60°C from an aqueous solution of 10 mM Ti(O₂)²⁺ and 45 mM HCl in wider thickness range (50-600 nm) [2005 Röh] showed that with the increase of the film thickness, the surface roughness decreases at the beginning, and then increases again for longer film deposition time. This higher value of the surface roughness for very thin films is explained by the fact that for the short deposition time the substrate surface is not totally covered with the film. In this early stage the inhomogeneous and island-like precipitations may increase the surface roughness. If

the deposition time is expanded, the islands grow together resulting in formation of continuous film. With further extension of the deposition time bigger agglomerates appeared on the film surface and the surface roughness increases again [2002 FHN, 2005 Röh].

In these investigations, TiO₂ films obtained after a deposition time of 2 h are homogeneous and continuous (Fig. 4.2 a), so the increase of surface roughness with the film thickness is attributed to the explanation given above.

4.1.3. Influence of the deposition temperature and the composition of the reaction solution on the thickness and morphology of films

TiO₂ films were deposited on a Si substrate by the LFD technique for 4 h from a 10 mM Ti(O₂)²⁺ solution in addition of HCl at different deposition temperatures (40-90°C). As can be seen, the thickness of the films after 4 h, as estimated by SEM cross-section examinations, depends strongly on the acidity of solution and temperature. The thickness can be enhanced by decreasing the acid concentration and increasing temperature (Fig. 4.4).

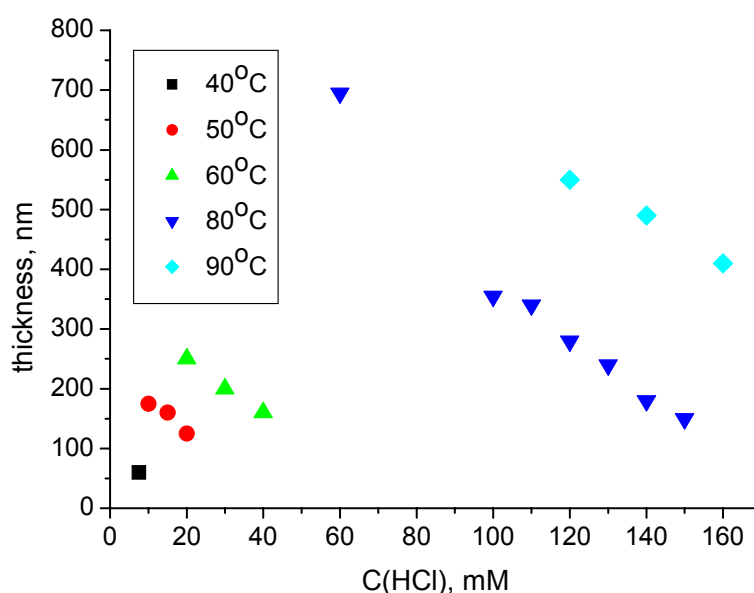


Fig. 4.4 Dependence of TiO₂ film thickness on the acid concentration; the films were deposited on a Si substrates by the LFD for 4h from an aqueous solution of 10 mM Ti(O₂)²⁺ at different temperatures: 40, 50, 60, 80 and 90°C

The diagram reveals a nearly linear dependence between the film thickness and the acid concentration, for each deposition temperature. Such conditions may, therefore, be expected to result in a higher nucleation and growth rate of the particles [2002 TLS]. The influence of the temperature on the growth rate can be explained by the Arrhenius equation (temperature dependence of the rate constant). The decrease of the film thickness with increasing acid concentration can be attributed to the equilibrium of the hydrolysis reaction shown in Equation 2.6 (chapter 2.4).

Each reaction temperature demands optimization of the acidity of the solution, i.e. higher deposition temperatures requires higher amounts of added HCl. An insufficient acid concentration lead to visible bulk precipitation during the deposition, while in the case of a high acid concentration there was no film deposition.

The investigation of the reaction solution by the dynamic light scattering (DLS) measurements [2005 HBW], carried out for solutions containing various amount of HCl at 60°C, show the progression of the mean average size (hydrodynamic radius) of the formed particles as a function of the reaction time (Fig. 4.5).

According to Fig. 4.5, the induction time for the formation of the first nanoparticles which can be observed due to the detection limit of the DLS (> 20 nm) in solution depends on the acid concentration of the reaction solution, i.e. higher concentrations lead to longer induction times. The induction period dropped from about 30 min for 50 mM HCl to about 5 min for 25 mM HCl. The same influence of pH on nucleation and growth of particles was observed by DLS for SnCl₄/HCl [2002 TLS] and Zr(SO₄)₂/HCl solutions [2002 CSF].

A low acid concentration leads to the formation of the agglomerated particles on the film surface, even when no visible precipitation occurred in the reaction solution during the film deposition. So, formation of large particles in solution and their sedimentation on the film surface cannot be avoided even with applying the LFD technique, where reaction solution is refreshing in the deposition chamber during the deposition process, if the acid concentration is insufficient (120 mM for 90°C, 60 mM for 80°C and 20 mM for 60°C, Fig 4.6 a, 4.7 a and 4.8 a). In such cases it can be assumed that the induction time is so short that particle formation starts immediately when deposition medium reach the deposition temperature in the chamber. In this situation, particles sedimentation in the reaction chamber can be prevented with increasing the acid concentration in solution (Fig 4.6 b,c, 4.7 b,c and 4.8 b,c). Supothina et al. in their investigation of deposition SnO₂ films by the LFD [2003 SDH]

suggested that the formation of the big particles can be controlled by the flow rate, i.e. at higher flow rates, there is less time to form bigger particles in the reaction solution before it is flushed from the deposition chamber. It is possible to define the average residence time of the fluid in the LFD chamber, $t = V/F$, where V is volume of reaction solution in the chamber and F is the flow rate. With the volume of 10 ml and the flow rate of 1.5 ml/min, the average residence time is about 6.5 min. According to the DLS measurements shown at Fig. 4.5, the induction time for 20 mM HCl reaction solution is less than 5 min, so the average residence time of 6.5 min is sufficient for the formation of the bigger particles in solutions and their deposition on the substrate surface.

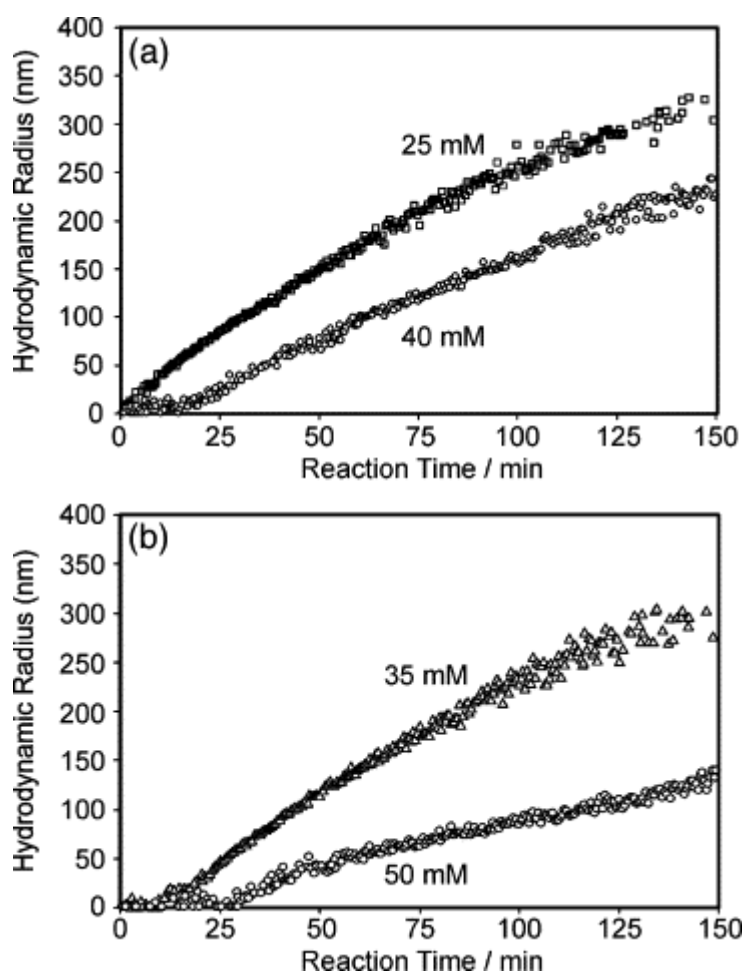


Fig. 4.5 Particle size as measured by DLS vs. time from solution containing 10 mM $\text{Ti}(\text{O}_2)^{2+}$ and a) 25 and 40 mM HCl; b) 35 and 50 mM HCl; reaction temperature was 60°C [2005 HBW]

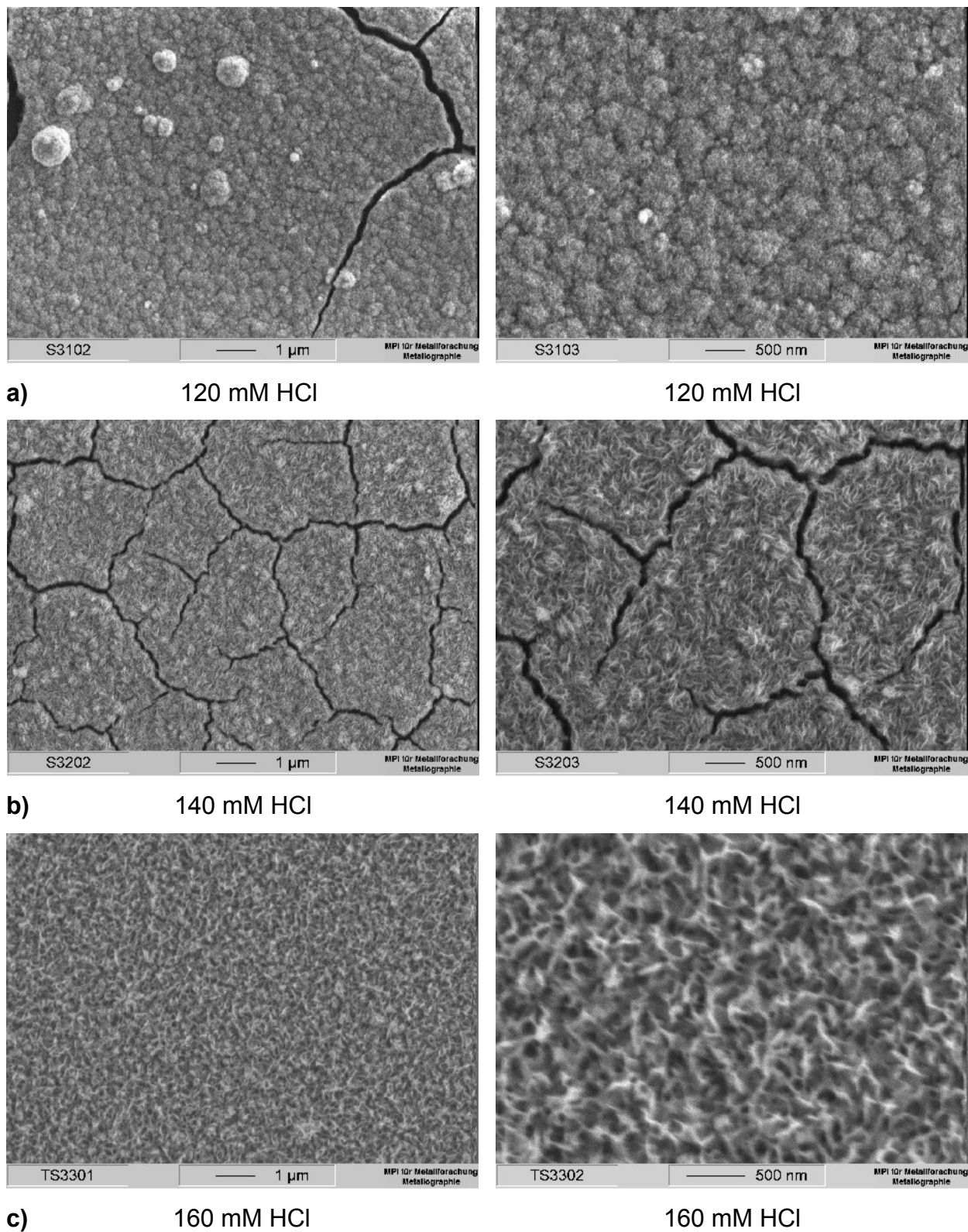


Fig. 4.6 SEM micrographs of TiO_2 films deposited on a Si substrates by LFD for 4 h from a 10 mM $\text{Ti}(\text{O}_2)^{2+}$ solution at 90°C in addition of a) 120; b) 140 and c) 160 mM HCl

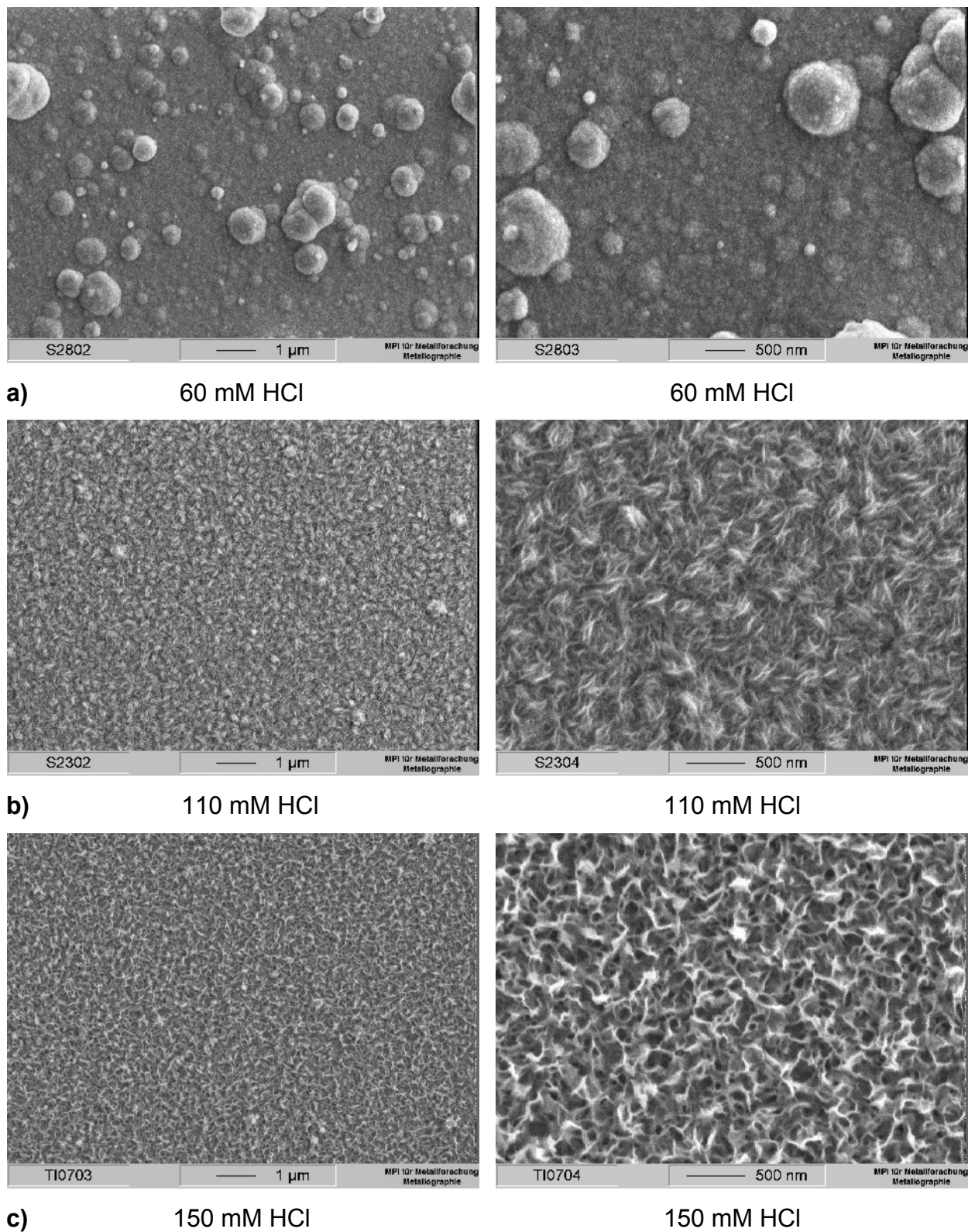


Fig. 4.7 SEM micrographs of TiO_2 films deposited on a Si substrates by LFD for 4 h from a 10 mM $\text{Ti}(\text{O}_2)^{2+}$ solution at 80°C in addition of a) 60; b) 110 and c) 150 mM HCl

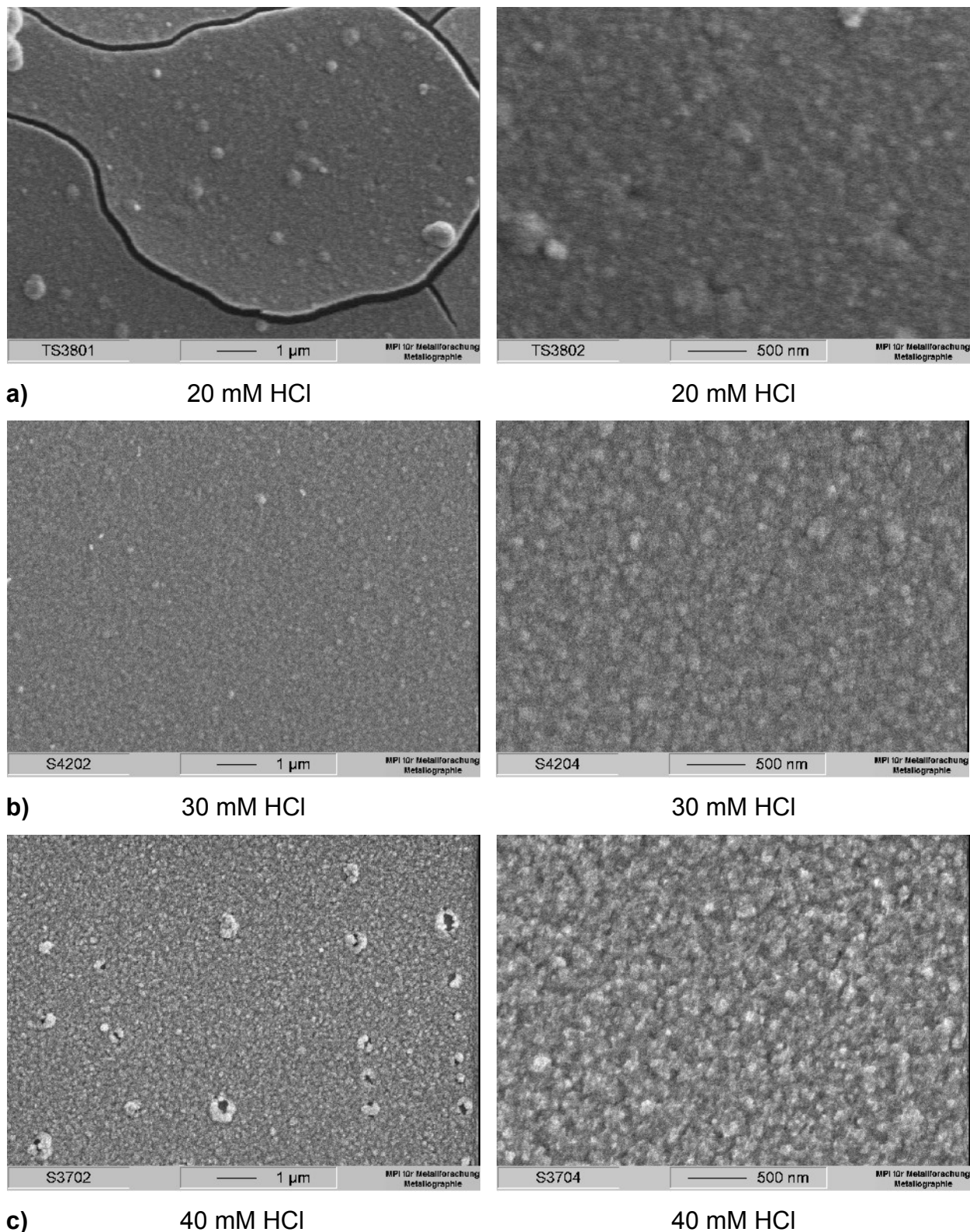


Fig. 4.8 SEM micrographs of TiO_2 films deposited on a Si substrates by LFD for 4 h from a 10 mM $\text{Ti}(\text{O}_2)^{2+}$ solution at 60°C in addition of a) 20; b) 30 and c) 40 mM HCl

The acid concentration in the reaction solution also has an influence onto the morphology of the films. The spherical structure of the deposits resulting from low acid concentration (Fig. 4.6 a and 4.7 a) become needle- or sponge-shaped for the films deposited with higher one (Fig. 4.6 b,c and 4.7 b,c). Cracks in the films are considered to arise due to the shrinkage during the drying of the films.

Changes of the film morphology affected by the composition of the precursor solution were reported by Yamabi et al. [2002 YIm]. They investigated the morphology of TiO₂ films grown from a TiOSO₄ – urea aqueous solution at 60°C. In their investigation urea was used for the complexation of Ti⁴⁺ cations with amino groups to reduce the reactivity of the Ti source in the system. The pH of the reaction solutions ranged from 0.5 to 1.6. Addition of urea into precursor solution greatly reduced the deposition rate of the films and also influenced the film morphology. They found that anatase films show spherical or needle-like shape, depending of the reaction rate. The deposition of spherical anatase particles from TiOSO₄ solutions without urea was accompanied with massive precipitates. On the other hand, the oriented needle-like anatase crystallites were prepared from TiOSO₄ solutions containing urea. The deposition rate of the anatase crystals in the TiOSO₄ solutions without urea occurred more rapidly resulting in the production of the non-oriented spherical particles with massive precipitates via homogeneous nucleation. In contrast, deposition with a relatively low reaction rate predominantly gives rise to heterogeneous nucleation and induces formation of the highly oriented needle-like crystals.

In this investigation, the growth rate of the TiO₂ films is influenced by the acidity of the reaction solution (pH ranged from 0.8 to 1.7). As it was mentioned before, an increase of the acid concentration leads to a decrease of the deposition rate (Fig. 4.4). That results in a change of the film morphology from spherical, for the TiO₂ films deposited with a high reaction rate, to needle-like structure, for the films deposited with a low reaction rate. Therefore, the obtained results confirm the influence of such kinetical factors, i.e. the reaction rate controlled by the acidity of the reaction solution on the film morphology.

The surface roughness of TiO₂ films deposited at 60°C from an aqueous solution of 10 mM Ti(O₂)²⁺ and 20, 30 or 40 mM HCl was investigated by AFM (Fig. 4.9). The obtained values show that the surface roughness reaches the minimum in case of films deposited with 30 mM acid concentration (Fig. 4.10). Higher roughness values for films deposited with lower acid concentration can be attributed to the formation of

big agglomerates in the solution and their deposition on the film surface (Fig. 4.5). Another increase in the surface roughness with higher acid concentrations in the solution is in accordance with the coarsening of the surface with the change of the spherical morphology to a sponge-like one, as it is shown on the SEM micrographs (Fig. 4.6, 4.7 and 4.8).

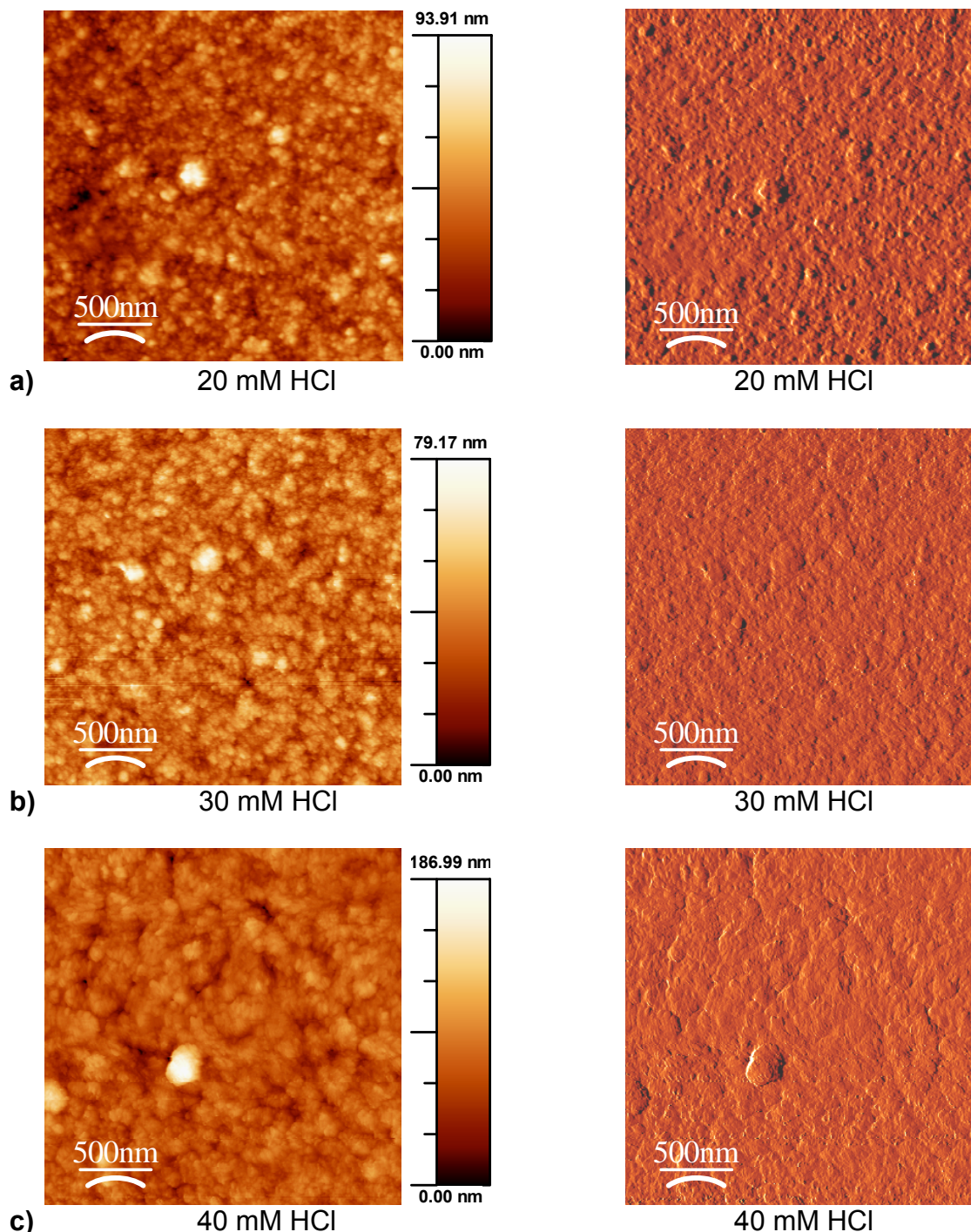


Fig. 4.9 AFM topographic (left) and corresponding deflection mode images (right) of TiO_2 films deposited by LFD on Si substrates at 60°C for 4 h from an aqueous solution of $10 \text{ mM Ti}(\text{O}_2)^{2+}$ and a) 20 mM; b) 30 mM and c) 40 mM HCl

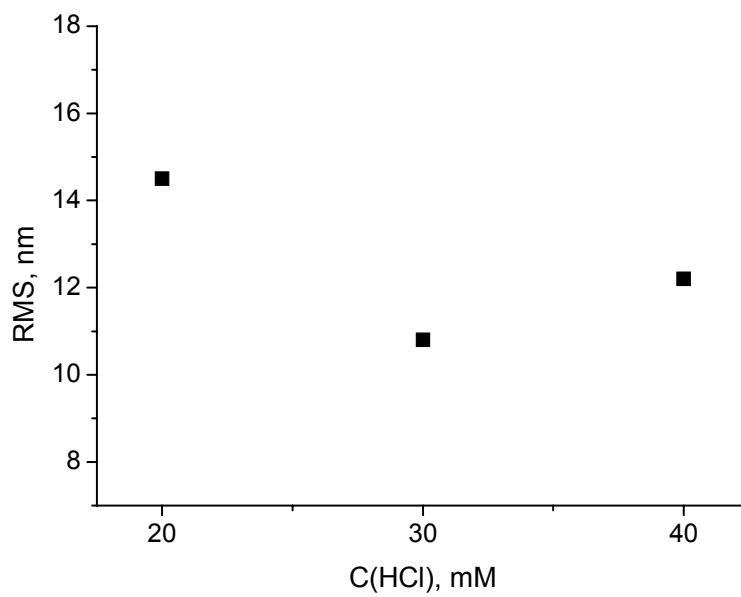


Fig. 4.10 Dependence between the surface roughness of TiO₂ films and the acid concentration of the corresponding reaction solution (10 mM Ti(O₂)²⁺). The deposition was carried out by LFD for 4 h at 60°C on Si substrates

4.1.4. XRD investigations

The structural characterization of the TiO_2 films was carried out by XRD measurements. The scans taken with grazing incidence configuration with an incident angle of 2° of films deposited at 60°C (Fig. 4.8b), 70°C (Fig. 4.11a) and 80°C (Fig. 4.11b) do not show any TiO_2 diffraction peaks (Fig. 4.12). The peaks present in the diffractograms belong to the silicon substrate [2005 Jia].

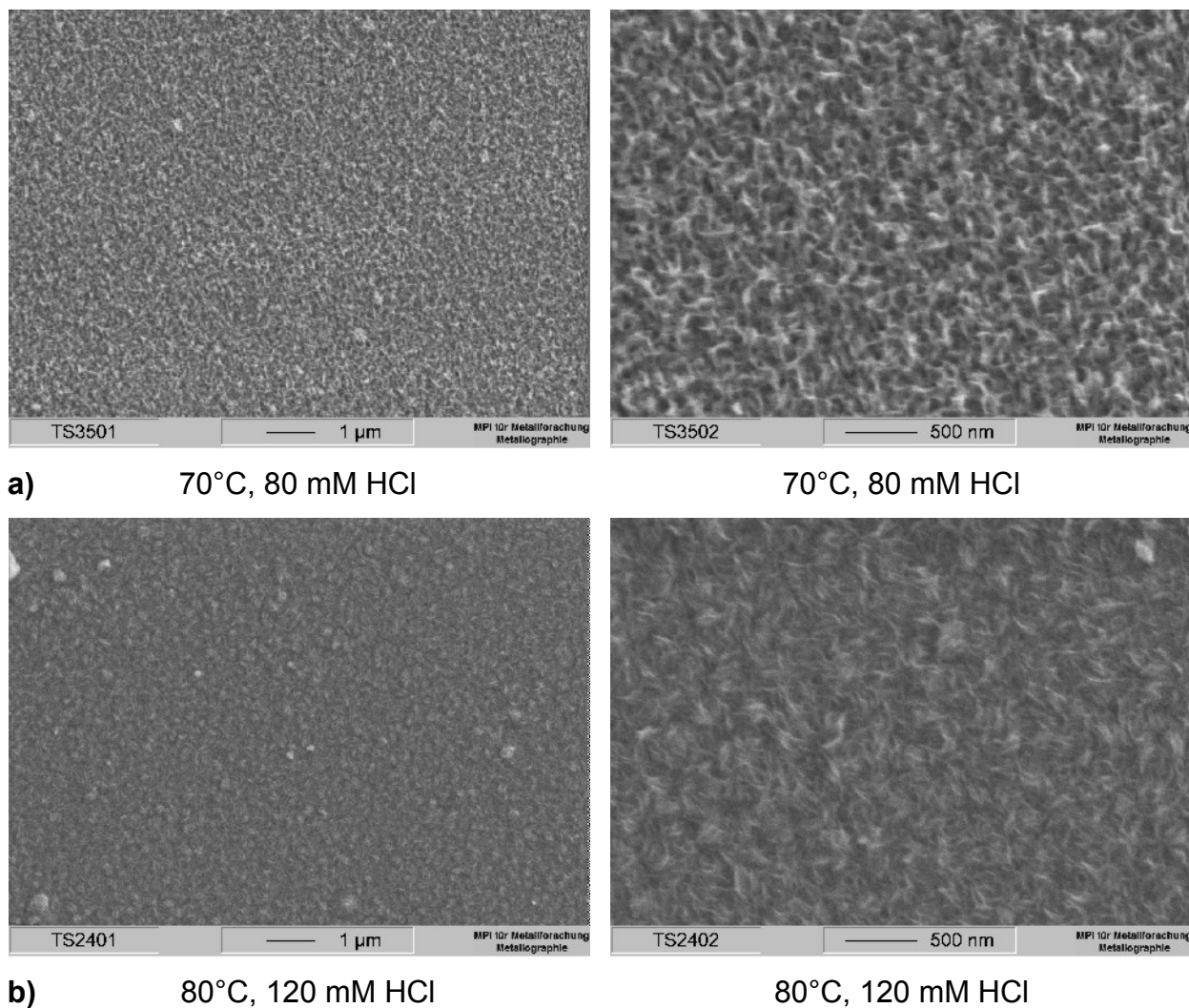


Fig. 4.11 SEM micrographs of TiO_2 films deposited by LFD for 4 h on Si substrates from an aqueous solution of $10\text{ mM Ti}(\text{O}_2)^{2+}$ and a) 80 mM HCl at 70°C ; b) 120 mM HCl at 80°C

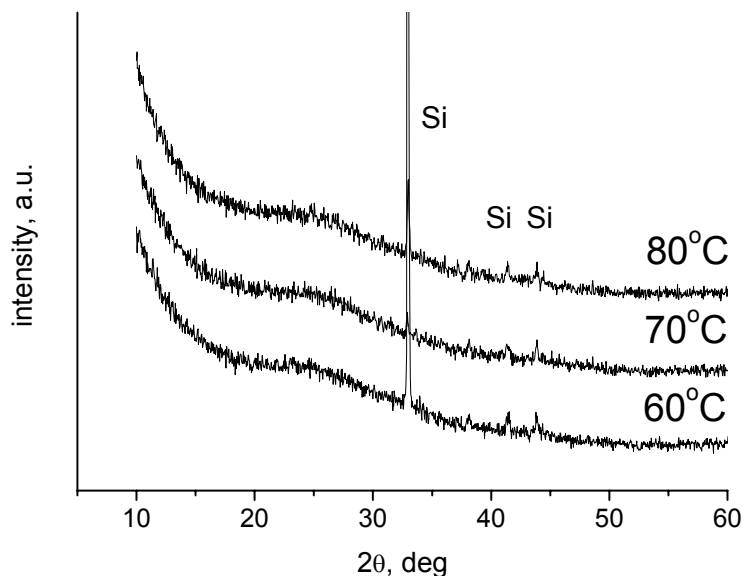


Fig. 4.12 Diffraction patterns (grazing incidence geometry) of TiO₂ films obtained by LFD for 4 h on Si substrates from an aqueous solution of 10 mM Ti(O₂)²⁺ and 30, 80 and 120 mM HCl at 60, 70 and 80°C, respectively

Further measurements were acquired using a Bragg-Brentano configuration (Fig. 4.13) for the as-deposited TiO₂ films and for the same films annealed for 2 h at 500°C.

The scans taken with the Bragg-Brentano technique of the as-deposited film do not show any TiO₂ diffraction peaks, like in case of their investigations with the grazing incidence configurations. The films annealed at 500°C for 2 h show one diffraction line. According to the Ref. [1969 NBS] (JCPDS file No. 21-1272 for TiO₂), it corresponds to the most intense peak (101) of anatase, indicating crystallization in the film during annealing. The same results were reported for TiO₂ films deposited by SD from an aqueous solution of 10 mM Ti(O₂)²⁺ and 140 mM HCl at 80°C and annealed at 500°C for 2h [2001 NBA]. Beside annealing, crystallization of the amorphous TiO₂ films can also be induced by the electron beam irradiation (see chapter 4.4.5.2.).

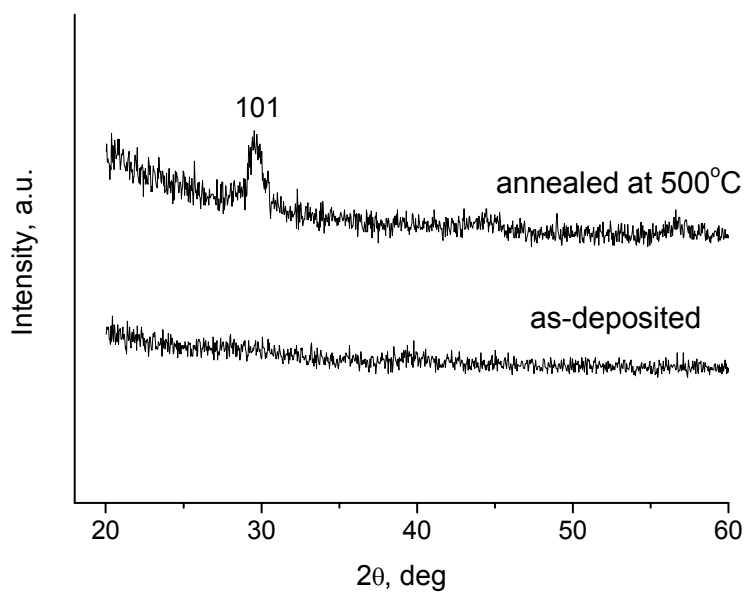


Fig. 4.13 Diffraction patterns (Bragg-Brentano geometry) of as-deposited TiO_2 films and TiO_2 films annealed at 500°C for 2 h; the TiO_2 films were deposited by LFD for 4 h on Si substrates at 60°C from an aqueous solution of 10 mM $\text{Ti}(\text{O}_2)^{2+}$ and 30 mM HCl

4.2. Synthesis of polyelectrolyte layers obtained via the layer-by-layer deposition technique and their characterization

Polyelectrolyte films were synthesized applying the layer-by-layer deposition technique. For the deposition of the polyelectrolyte (PE) films, poly(styrenesulfonate) (PSS) was used as anionic PE, polyethyleneimine (PEI) and poly(allylamine hydrochloride) (PAH) as cationic PEs. The deposition was carried out at room temperature for 20 min.

4.2.1. Thickness measurements

4.2.1.1. QCM measurements

The deposition process of the PE films was monitored by quartz crystal microbalance measurements (QCM). Due to the highly sensitive mass detection of this technique, it is possible to determine the adsorbed mass (i.e. the thickness) of every single polycation and polyanion layer that built up the multilayer film.

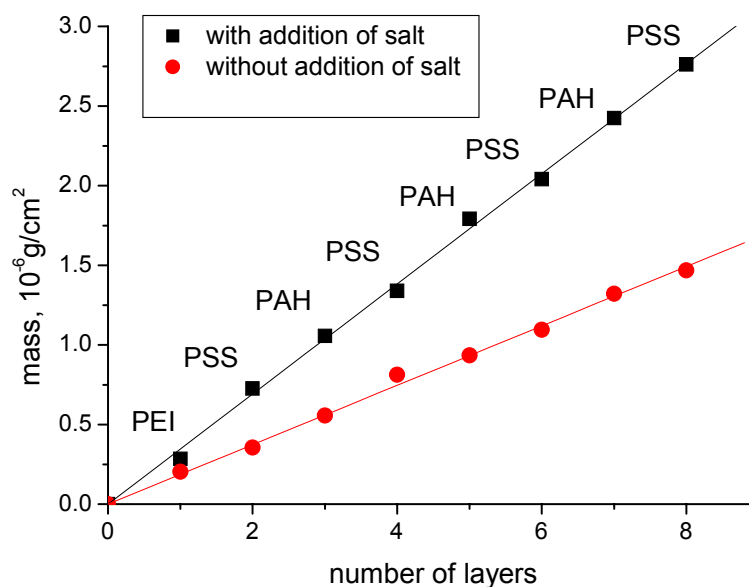


Fig. 4.14 Dependence between the deposited mass of a adsorbed polymer and the number of adsorbed cationic and anionic layers; the films were deposited from an aqueous solution: (■) with addition of salt (0.5 M MnCl_2 for deposition of PSS and 1 M NaCl for deposition of PAH); (●) without addition of salt

The formation of the PE multilayer films was investigated regarding the ionic strength of the original solutions. The experiments were performed using a salt-free aqueous solution or an aqueous solution in the presence of salt. In both experiments PEI layers were deposited from salt-free aqueous solutions in order to obtain a good coverage of the silicon substrate and the homogeneous, positively-charged film surface due to the flat conformation of polymer chains (see chapter 2.5. and latter discussion). Representative results are plotted in Fig. 4.14. The adsorbed mass of each polymer layer increases linearly with the number of deposition cycles.

The thickness of the layers (d) can be estimated if the density of the deposit (ρ) is known by substituting ρd for the deposited mass of the layer. The assumed density value of 1.2 g/cm^3 , which is common used in the literature [1997 CNF, 1999 LAO, 2000 BKA], is the density of dried, bulk polymers [1999 Blm]. In the layer-by-layer deposition of polyelectrolytes, the density value of the obtained films may vary with preparation conditions. It may depend on the conformation and the composition of the individual film components and their final structures, homogeneity and the surface coverage of the dried films, i.e. the film density. Because the multilayers that formed with polyelectrolytes of different charge densities and different ionic strength may show differences in the surface roughness and in water content [2004 SSH], an accurate assumption of the film density is difficult. Steitz et al. found in their investigations of PSS/PAH system deposited in the presence of salt, that the water content of un-dried films is about 40 vol% [2000 SLS].

By addition of salt to the aqueous solution of polyelectrolytes, the thickness of the films prepared from these solutions increases. The differences in film thickness are due to different conformations of the polymer chains: without salt the polymer chains are oriented flat and parallel to the substrate, whereas with higher salt concentration of the aqueous solution the chains form coils which are then adsorbed at the surface. Due to the screening of the charges along the polyelectrolyte chains in the presence of salt, the polymer is more entangled with larger thickness [2000 RLS].

4.2.1.2. AFM measurements

The thickness of the deposited $(\text{PEI/PSS})(\text{PAH/PSS})_n$ films was estimated by AFM in order to investigate the PE film growth. PSS and PAH layers were deposited from an aqueous solution in the presence of salt. The film thickness was measured from the second to the eighth cationic/anionic layer couple ($n = 1, 3, 5, 7$). Fig 4.15 shows a linear increase of the thickness with the number of adsorbed cationic/anionic layer couples.

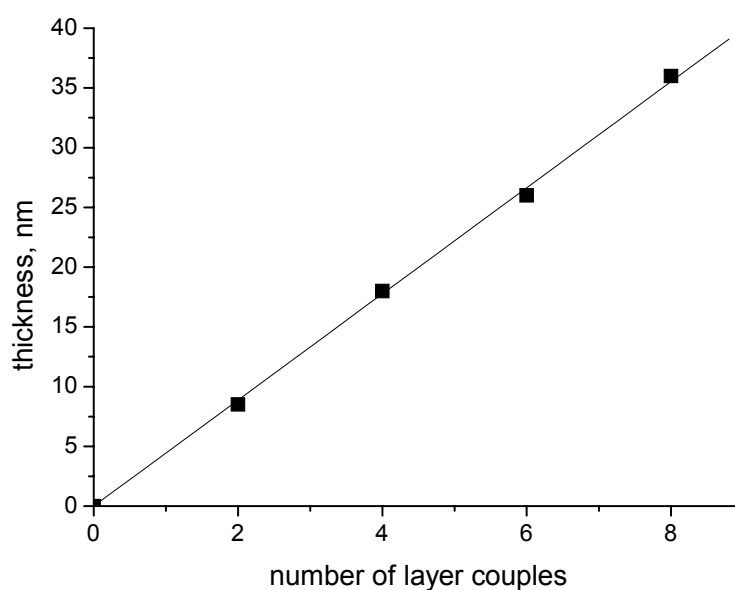


Fig. 4.15 Dependence between the thickness of $(\text{PEI/PSS})(\text{PAH/PSS})_n$ ($n = 1,3,5,7$) films and the number n of adsorbed cationic/anionic layer couples; PSS and PAH layers were deposited from an aqueous solution in the presence of salt (0.5 M MnCl_2 for deposition of PSS and 1 M NaCl for deposition of PAH)

4.2.1.3. TEM cross-section measurements

The thickness of the PE layers measured by AFM is revealed with TEM cross-section images. Due to the sensitivity of the PE layers to the TEM cross-section preparation process, the layer thickness was estimated from composite PE/TiO₂ specimens.

Fig. 4.16 presents TEM cross-section image of a PE/TiO₂ bilayer deposited on a Si substrate (see chapter 4.4) where the PE layer is consist of six cationic/anionic couples ((PEI/PSS)(PAH/PSS)₅).

The estimated thickness of the layer is about 25 nm, which is in agreement with obtained AFM measurements.

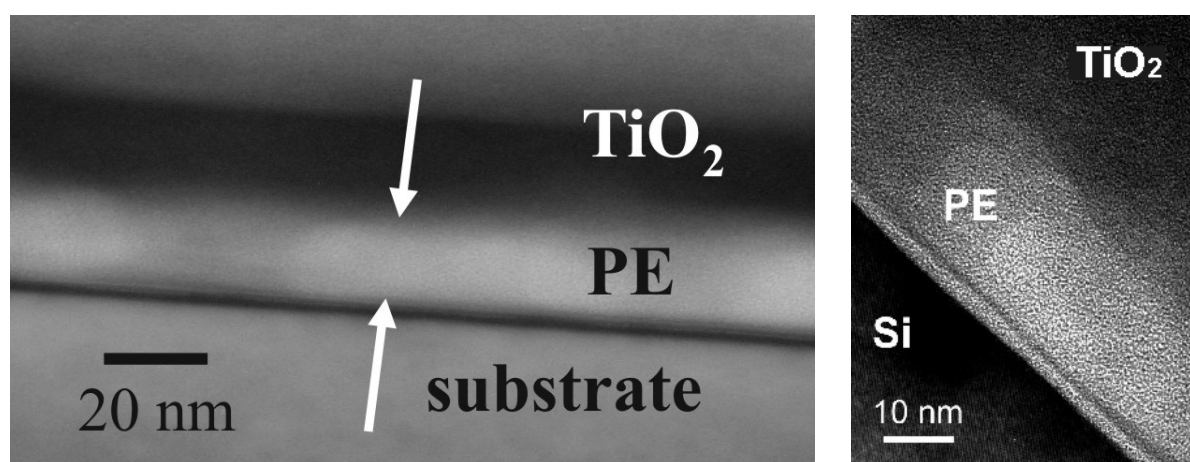


Fig. 4.16 TEM cross-section images of PE/TiO₂ bilayer taken from the image of (PE/TiO₂)₃ multilayer film (see Fig. 4.29); the PE layer consists of six cationic/anionic couples ((PEI/PSS)(PAH/PSS)₅); PSS and PAH layers were deposited from an aqueous solution in the presence of salt (0.5 M MnCl₂ for deposition of PSS and 1 M NaCl for deposition of PAH)

4.2.1.4. UV/VIS spectroscopy measurements

UV/VIS spectroscopy was also used to characterize the growth of PE layers and the amount of material deposited per layer on Si substrates. The optical absorption of the films increases with the number of cationic/anionic PE layer couples. The consistency of the deposition process is indicated in Fig. 4.17 (taken from Ref. [2005 Röh]), which shows a linear increase of the difference in the absorption peak (maximum) at a wavelength of 230 nm (due to PSS) and the absorption at 349 nm (located within the range of wavelengths where absorption stays nearly constant) (ΔA) with an increase of number of PE layer couples.

If the thickness value is already estimated by some other characterization methods, for example by TEM cross-section images as presented in Fig. 4.16 (25 nm), the thickness of the other PE couples can easily be calculated from the corresponding ΔA values using the known thickness value of (PEI/PSS)(PAH/PSS)₅ as a reference (Fig. 4.17). QCM and AFM measurements presented before (Fig. 4.14 and 4.15) are in agreement with linear dependence between the layer growth and number of deposited layers

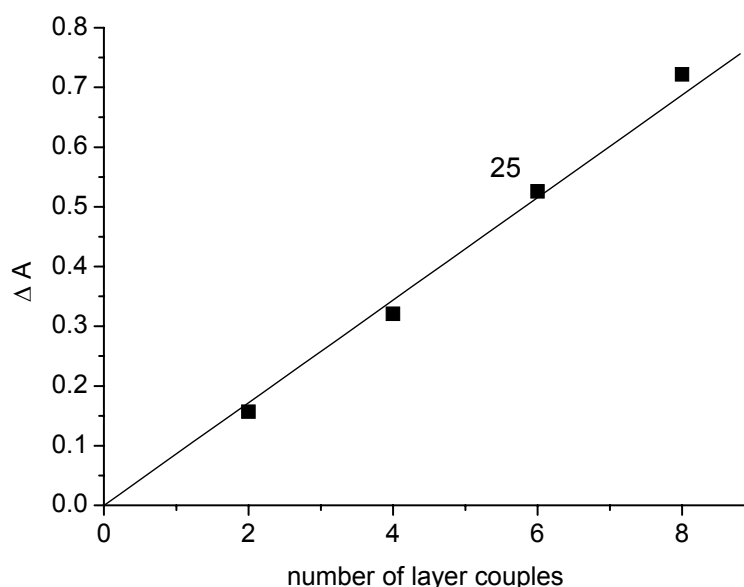


Fig. 4.17 Dependence between the difference in the absorption peak (ΔA) and the number of adsorbed layer couples [2005 Röh]; PAH and PSS layers were deposited in the presence of salt (0.5 M MnCl_2 for deposition of PSS and 1 M NaCl for deposition of PAH); the numbers in the diagram represent thickness values of PE films. For the calculation of these values the experimentally determined thickness for 6 layer couples (25 nm, obtained from TEM cross-section image, Fig. 4.15) was used as a reference.

4.2.1.5. Thickness of PE films

The thickness values determined by AFM, UV spectroscopy and the QCM technique for the films deposited from salt solution are summarized in Tab 4.1. It can be seen that thickness values for the films measured by the QCM technique are somewhat higher than the ones measured by AFM and the estimated values from UV spectroscopy measurements. It is known that the structure of the films made from water-based systems is sensitive to humidity changes and film thickness can vary with humidity of the air, after immersion in aqueous solutions, or after drying [1994 DLS, 2000 BJL]. As QCM measures the adsorbed mass of polymer during the deposition process, some residual water molecules can be incorporated in the polymer layers and increase the adsorbed mass. Therefore, the thickness estimated by QCM is the thickness measured for hydrated films, while the other techniques investigate the thickness of dried films. Determined thickness values are about 30% higher than the ones estimated by AFM measurements, which confirms incorporation of water in the polymer films [2000 SLS].

All applied techniques have demonstrated that the thickness of the PE films increase linearly with the number of adsorption steps. This means that the thickness increase of each polycation and polyanion layer remains constant independent on the number of adsorption cycles.

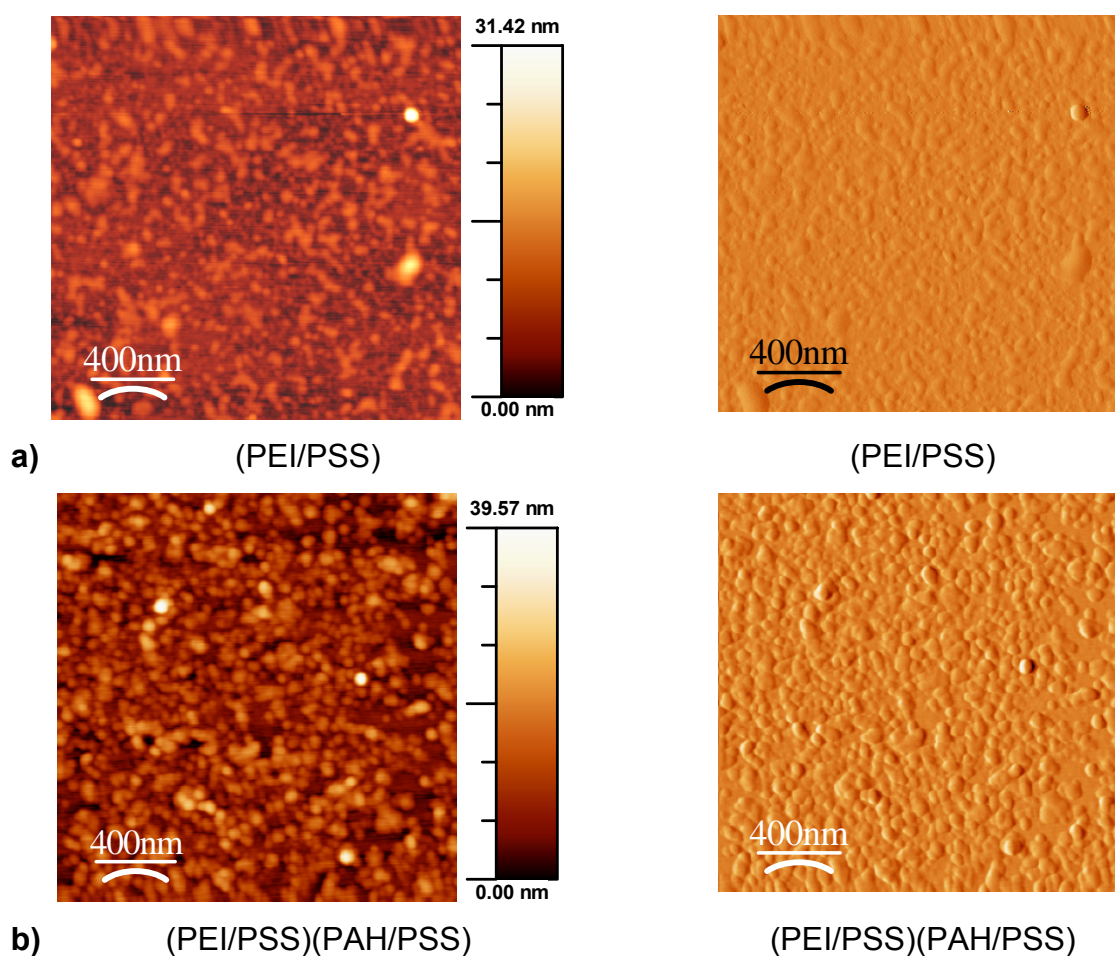
Tab. 4.1 Thickness of (PEI/PSS)(PAH/PSS)_n layers obtained by AFM, UV spectroscopy (in combination with TEM cross-section data) and QCM; PSS and PAH layers were deposited from an aqueous solution in the presence of salt (0.5 M MnCl₂ for deposition of PSS and 1 M NaCl for deposition of PAH)

number of layers	thickness (nm)		
	AFM	UV + TEM	QCM
1	n.d.*	n.d.	2.5
2	n.d.	n.d.	6
3	n.d.	n.d.	9
4	8.5	8	11
5	n.d.	n.d.	5
6	n.d.	n.d.	17
7	n.d.	n.d.	20
8	18	17	23
12	26	25	n.d.
16	35	34	n.d.

n.d. – not determined

4.2.2. Morphological characterization of the PE layers

AFM images of $(\text{PEI/PSS})(\text{PAH/PSS})_n$ films, where PSS and PAH layers were deposited in the presence of salt, are presented in Fig. 4.18. The images show densely packed globular aggregates, with diameters in the range of 40-100 nm. With the increasing number of layers the size of the features grows. This is in agreement with findings that globular structures are present in the case of PE systems deposited in the presence of salt, causing an increase in surface roughness of the deposited films [1993 LDM, 1999 KFJ]. The aggregates are coiled chains of PSS and PAH, forced in this configuration by the presence of salt ions in the deposition solution.



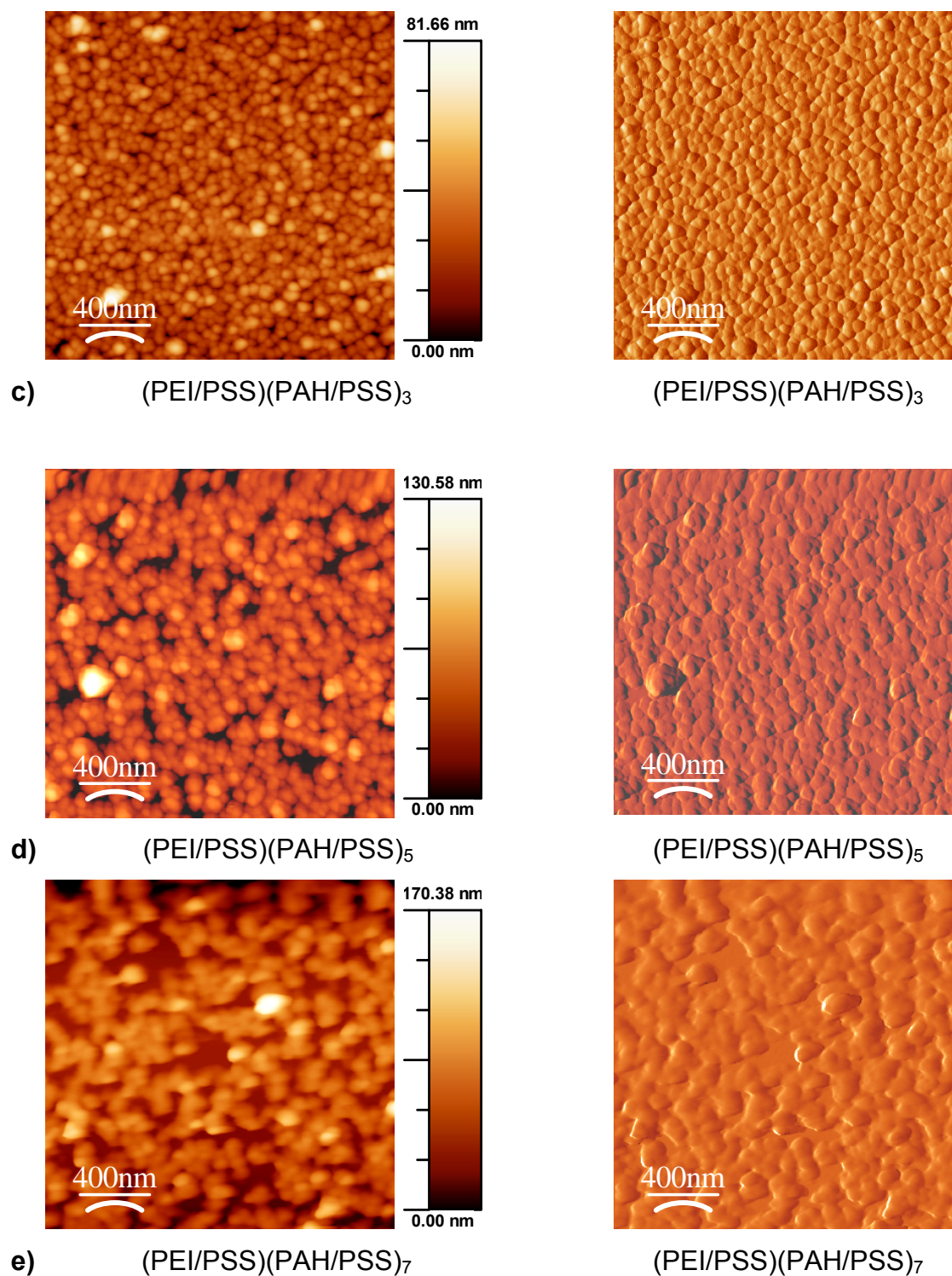


Fig. 4.18 AFM topographic (left) and corresponding deflection mode images (right) of Si/(PEI/PSS)(PAH/PSS)_n layers: a) n = 0, b) n = 1, c) n = 3, d) n = 5, e) n = 7; PSS and PAH layers were deposited in the presence of salt (0.5 M MnCl₂ for deposition of PSS and 1 M NaCl for deposition of PAH)

STEM cross-section images of a (PEI/PSS)(PAH/PSS)₅ layer (Fig. 4.19) reveal the presence of globular aggregates in the deposited polymer.

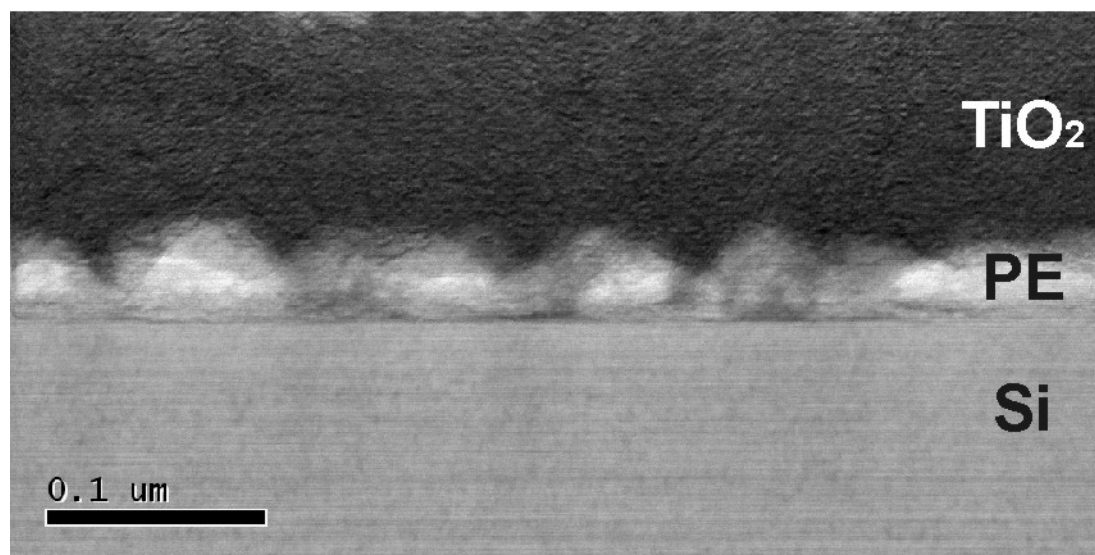


Fig. 4.19 STEM cross-section image of (PEI/PSS)(PAH/PSS)₅ film in PE/TiO₂ bilayer film; the polyelectrolyte layer (PE) is appearing as a bright region on the image

The surface roughness of the deposited PE films increases with the number of layer couples, i.e. with the film thickness (Fig. 4.20 a). Although the surface roughness of PE layers deposited in the presence of salt is higher in comparison with the one of PE layers deposited without salt for the same number of cationic/anionic couples, investigations of surface roughness for PE layers deposited without salt showed that the roughness values are almost equivalent for the same final thickness of both PE films (Fig. 4.20 b).

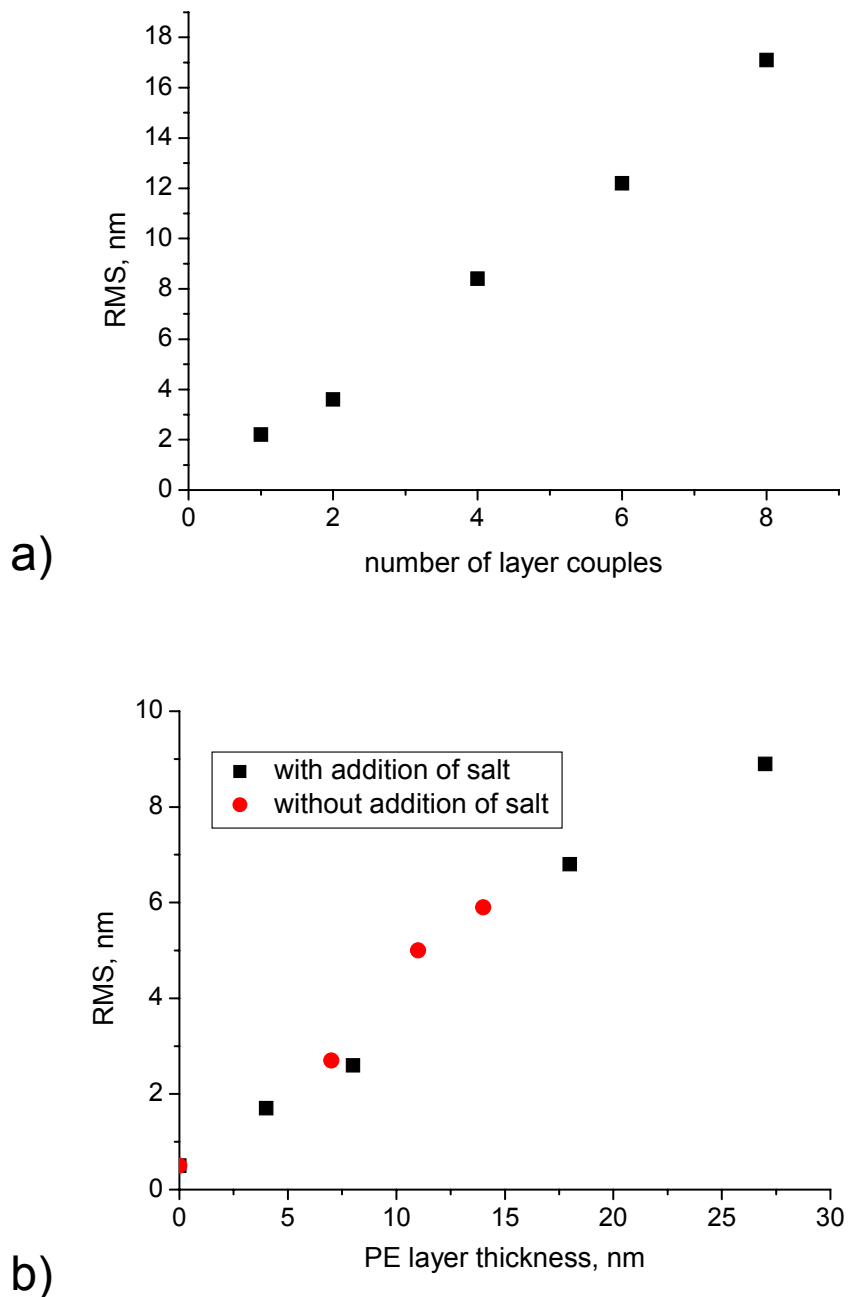


Fig 4.20 a) Dependence between the surface roughness of $(PEI/PSS)(PAH/PSS)_n$ layer and the number of adsorbed cationic/anionic layer couples; PAH and PSS layers were deposited in the presence of salt (0.5 M $MnCl_2$ for deposition of PSS and 1 M NaCl for deposition of PAH). b) Dependence between the surface roughness of $(PEI/PSS)(PAH/PSS)_n$ layer and the layer thickness; the films were deposited from an aqueous solution: (■) with addition of salt (0.5 M $MnCl_2$ for deposition of PSS and 1 M NaCl for deposition of PAH); (●) without addition of salt [2005 Röh]

4.3. Deposition of TiO₂ films on modified surfaces

SEM images of TiO₂ films deposited on PE-modified Si substrates can be seen in Fig. 4.21. The deposition of TiO₂ was carried out in the same way as the deposition on bare Si substrates, applying LFD from an aqueous solution of 10 mM Ti(O₂)²⁺ and 30 mM HCl solution at 60°C for 4h. The PE templates consist of two cationic/anionic couples ((PEI/PSS)(PAH/PSS)) with the thickness of about 8 nm (Tab. 4.1). The thickness of the TiO₂ film, estimated from the SEM cross-sections images in Fig. 4.21 on PE-modified Si substrates is slightly higher (230 nm) than the one of the film deposited on unmodified Si (200 nm).

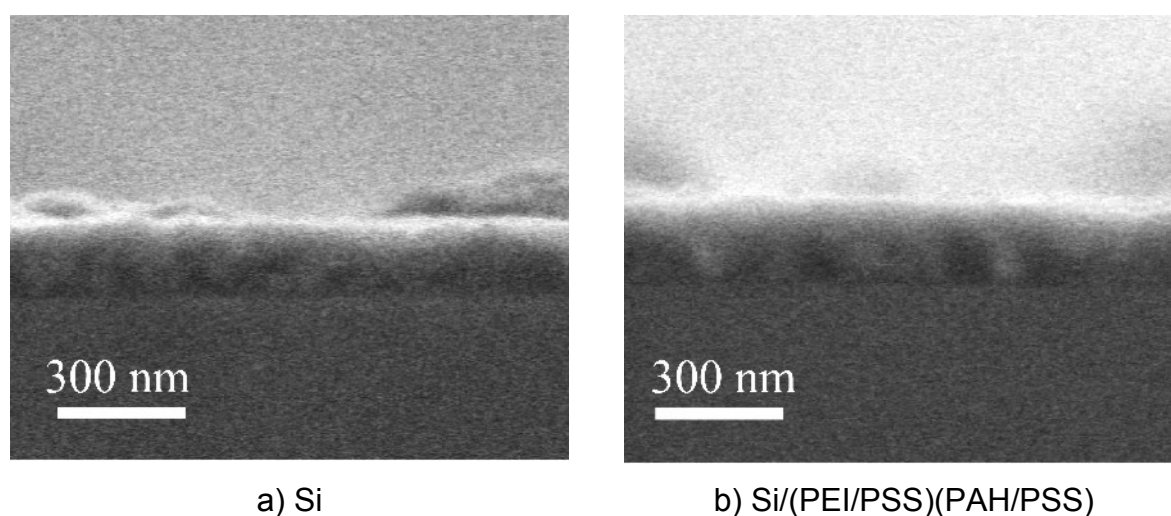


Fig. 4.21 SEM cross-section images of TiO₂ films deposited from an aqueous solution of 10 mM Ti(O₂)²⁺ and 30 mM HCl at 60°C for 4h by LFD on: a) Si and b) Si/(PEI/PSS)(PAH/PSS); the PE layers consist of two cationic/anionic couples ((PEI/PSS)(PAH/PSS)), where PSS and PAH were deposited from salt solution (0.5 M MnCl₂ for deposition of PSS and 1 M NaCl for deposition of PAH)

The results are in line with the model for the TiO₂ film formation suggested for the deposition from aqueous solutions of titanium, which are also used in this study [1995 SCD, 2001 NBA]. According to this model, the TiO₂ film growth is based on the attachment of positively charged titania colloidal particles formed in the solution to the negatively charged sulfonate-terminated surface of SAMs (chapter 2.4.). This model is also discussed in other reports [2005 Röh] that deal with the deposition of TiO₂ film on the PE-terminated substrates, with the sulfonate group of PSS.

The increase in film thickness, for the films deposited on PE-modified Si substrates compared to the bare silicon substrates, can be explained by an increased electrostatic attraction between the positively charged TiO₂ particles and the negatively charged PSS layer. As the pH of the reaction solution is 1.6 and the

isoelectric point (IEP) of the TiO_2 particles is in the range of 5.9-6.2 [1998 SAD], it can be assumed that TiO_2 particles are positively-charged in the deposition medium. Under the acidic deposition conditions, the sulfonate group of PSS, similar to the strongly deprotonating sulfonate-terminated surface of SAMs ($-\text{SO}_3\text{H} \rightarrow -\text{SO}_3^- + \text{H}^+$) [1995 SCD] makes the surface negatively-charged. Therefore, the negatively-charged sulfonate groups of PSS would then add an electrostatic attraction to the van der Waals attraction between the PE and the TiO_2 particles, initiating the formation and adhesion of the film. Although the IEP of silicon is 2 [1998 SAD] at the pH value of 1.6, uniform and homogeneous films are also formed on the bare Si substrates. In this case, obviously the attractive van der Waals forces between the particles and the bare substrate overrule the repulsive electrostatic contribution. Consequently, the obtained films are thinner than the ones obtained on the PE-modified surface (Fig. 4.21).

SEM micrographs of the obtained films are presented in Fig 4.22. Homogeneous films with very similar topography are deposited on both the unmodified Si substrate (Fig. 4.22 a) and the PE-covered silicon substrates (Fig. 4.22 b).

The topography and the roughness of the TiO_2 films deposited on PE-modified Si substrates was investigated also by AFM (Fig 4.23). The obtained surface roughness values (RMS ~ 12 nm) are comparable with that of the TiO_2 films deposited on unmodified Si substrates (~ 11 nm, Fig. 4.3). This result is in accordance with the relatively low surface roughness of the thin PE layer (~ 3.5 nm, Fig. 4.20) not much different from the bare Si substrate (0.5-1 nm).

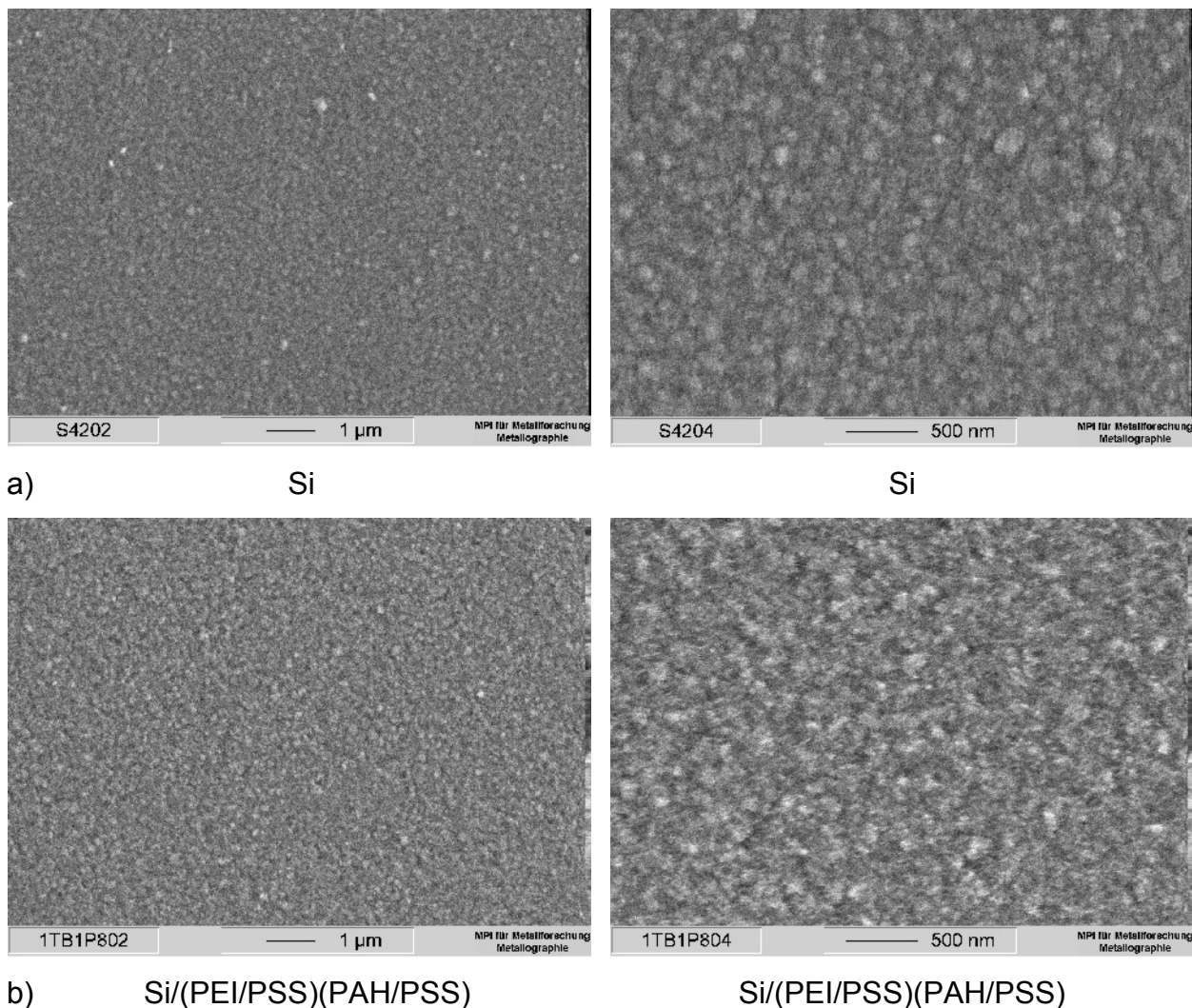


Fig. 4.22 SEM images of TiO₂ films deposited from an aqueous solution of 10 mM Ti(O₂)²⁺ and 30 mM HCl at 60°C for 4h by LFD on: a) Si and b) Si/(PEI/PSS)(PAH/PSS); the PE layers consist of two cationic/anionic couples ((PEI/PSS)(PAH/PSS)); PSS and PAH were deposited from salt solution (0.5 M MnCl₂ for deposition of PSS and 1 M NaCl for deposition of PAH)

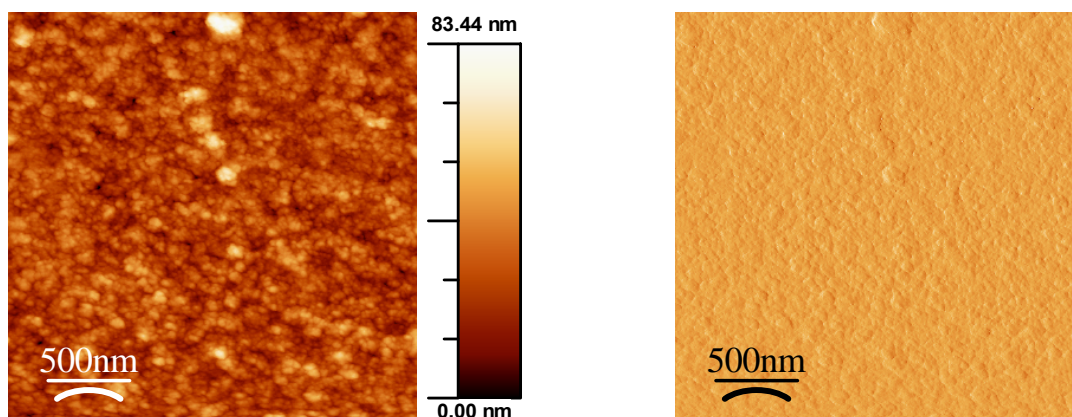


Fig 4.23 AFM topographic (left) and corresponding deflection mode image (right) of TiO₂ films deposited from an aqueous solution of 10 mM Ti(O₂)²⁺ and 30 mM HCl at 60°C for 4h by LFD on a Si substrate modified with PE; the PE layers consist of two cationic/anionic couples ((PEI/PSS)(PAH/PSS)); PSS and PAH were deposited from salt solution (0.5 M MnCl₂ for deposition of PSS and 1 M NaCl for deposition of PAH)

Both types of TiO_2 films were investigated also by X-rays using a Bragg-Brentano configuration (Fig. 4.24). In both cases the diffraction patterns do not show any peaks of TiO_2 , thus obviously also PE does not induce crystallization of TiO_2 films. Although it was reported that nanocrystalline TiO_2 was formed from a solution of 10 mM $\text{Ti}(\text{O}_2)^{2+}$ and 0.14 M HCl at 80°C on sulfonate-terminated SAMs-, the TiO_2 films deposited on PE-modified Si are amorphous. The lack of the crystallinity in the film could be a result of random arrangement of sulfonate sites on the PE surfaces comparing to a high-ordered SAM, which may not favor the nucleation of crystalline phases of TiO_2 . Though the PE layer completely covers the silicon surface, it is rougher and more disorganized than a well-formed SAM [2002 PSS].

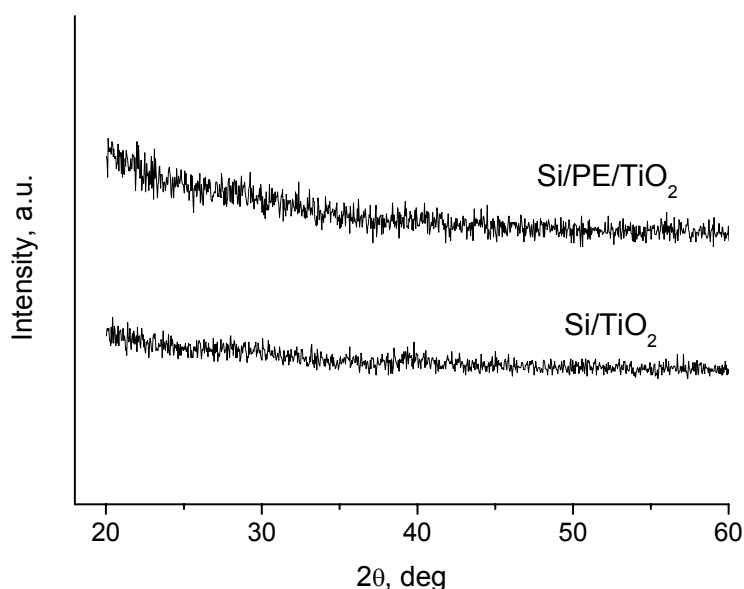
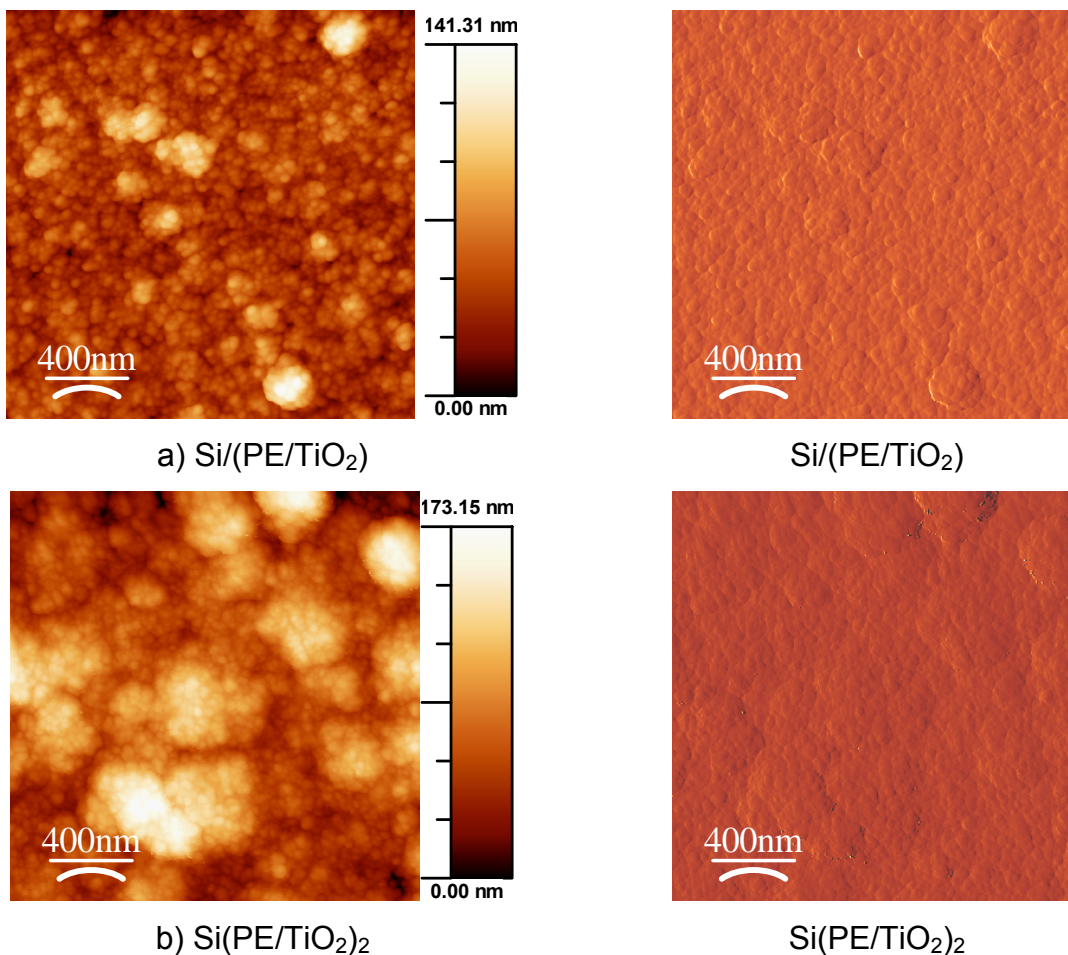


Fig. 4.24 Diffraction patterns (Bragg-Brentano geometry) of TiO_2 films deposited by LFD from an aqueous solution of 10 mM $\text{Ti}(\text{O}_2)^{2+}$ and 30 mM HCl at 60°C on a Si substrate and on a Si substrate modified with PE; the PE layers consist of two cationic/anionic couples ((PEI/PSS)(PAH/PSS)); PSS and PAH were deposited from salt solution (0.5 M MnCl_2 for deposition of PSS and 1 M NaCl for deposition of PAH)

4.4. Synthesis and characterization of PE/TiO₂ multilayers

4.4.1. Characterization of the topography of PE/TiO₂ multilayers by AFM

For investigation of the evolution of the multilayer film formation, multilayers with one, two, three and five PE/TiO₂ couples were synthesized. The topography of the PE/TiO₂ multilayer film surface was investigated by AFM measurements (Fig. 4.25). The investigations show that the TiO₂ films deposited on PE are uniform and homogeneous even after deposition of five PE/TiO₂ couples. The film surface reveals agglomerates of TiO₂ that are in size from 100–200 nm for one PE/TiO₂ couple to 300–400 nm for the (PE/TiO₂)₅ multilayer.



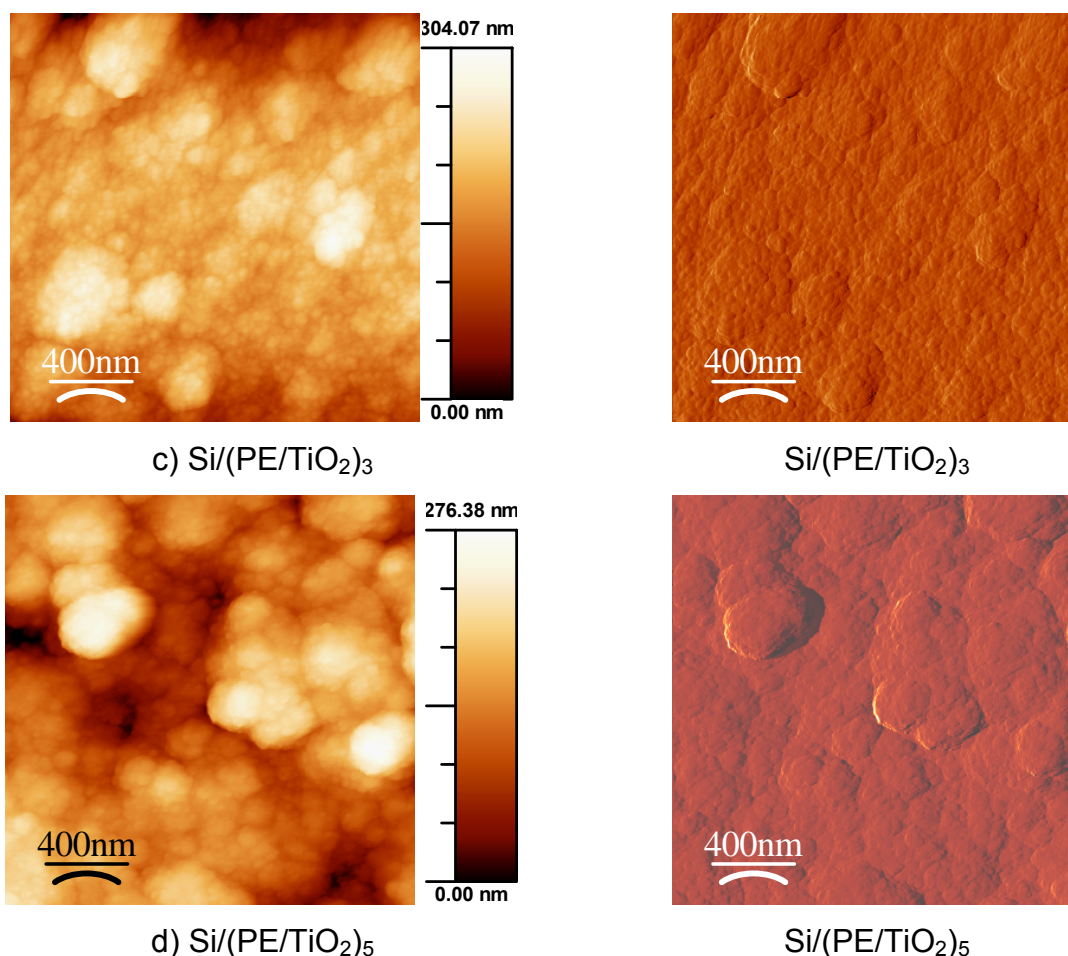


Fig. 4.25 AFM topographic (left) and corresponding deflection mode images (right) of PE/TiO₂ multilayer films: a) Si/(PE/TiO₂); b) Si/(PE/TiO₂)₂; c) Si/(PE/TiO₂)₃ and d) Si/(PE/TiO₂)₅; the PE layers consist of six cationic/anionic couples ((PEI/PSS)(PAH/PSS)₅); PSS and PAH were deposited from salt solution (0.5 M MnCl₂ for deposition of PSS and 1 M NaCl for deposition of PAH); the TiO₂ films were deposited by SD from an aqueous solution of 10 mM Ti(O₂)²⁺ and 30 mM HCl at 60 °C for 1x2 h

The surface roughness increases with the number of PE/TiO₂ bilayers and it is enhanced by the incorporation of the PE layers (Fig. 4.26). The surface roughness values for TiO₂ films deposited for 2 h on (PEI/PSS)(PAH/PSS)₅ modified silicon is ~17 nm and it's higher than the one for the films deposited on unmodified silicon (~8 nm, Fig. 4.3). The increase in surface roughness can be attributed to the higher surface roughness of the (PEI/PSS)(PAH/PSS)₅ layer (~12 nm), comparing to the roughness of bare Si (0.5-1 nm). The incorporation of PE layers provides larger surface irregularities which accumulate with an increasing number of deposition cycles, so for the multilayer made of five PE/TiO₂ couples it approaches a value of about 50 nm.

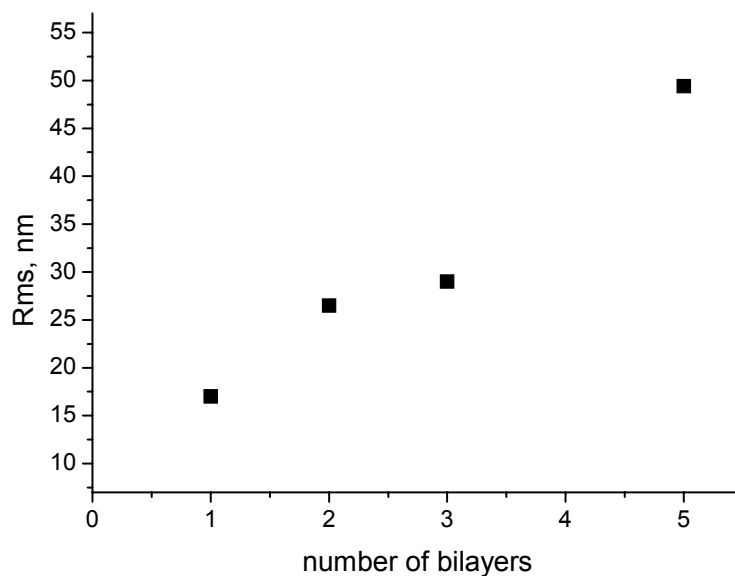
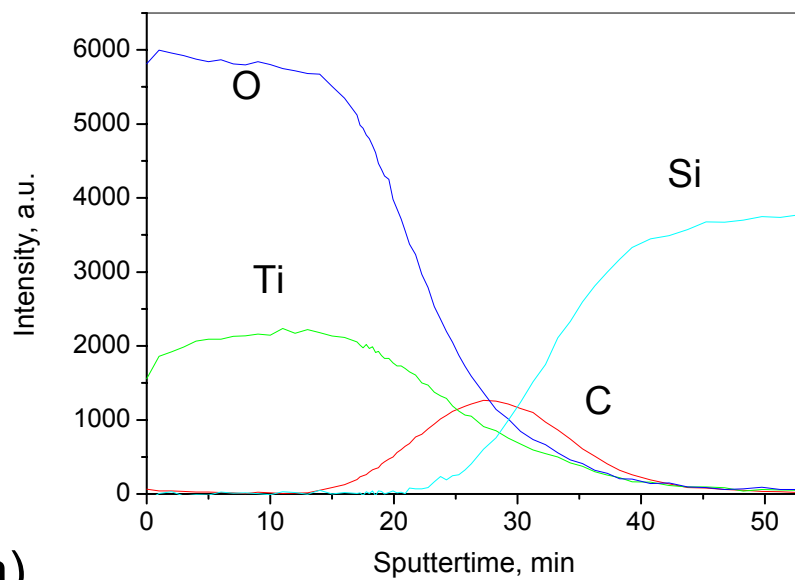


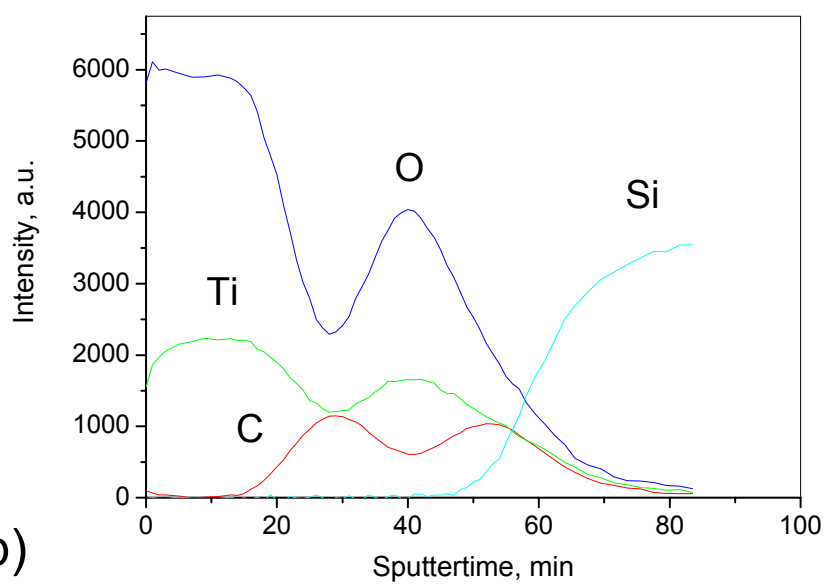
Fig. 4.26 Dependence between the AFM surface roughness and the number of PE/TiO₂ bilayers; the PE layers consist of six cationic/anionic couples ((PEI/PSS)(PAH/PSS)₅); PSS and PAH were deposited from salt solution (0.5 M MnCl₂ for deposition of PSS and 1 M NaCl for deposition of PAH); the TiO₂ films were deposited SD from an aqueous solution of 10 mM Ti(O₂)²⁺ and 30 mM HCl at 60°C for 1x2 h

4.4.2. Composition of the PE/TiO₂ multilayers

Auger electron spectroscopy (AES) was used to determine the concentrations of Ti and O, C (as the main constituent of the organic phase) and of Si (substrate), as a function of the depth below the film surface. The resulting concentration-depth profiles show a well-defined periodic structure of the organic-inorganic composite film (Fig. 4.27).



a)



b)

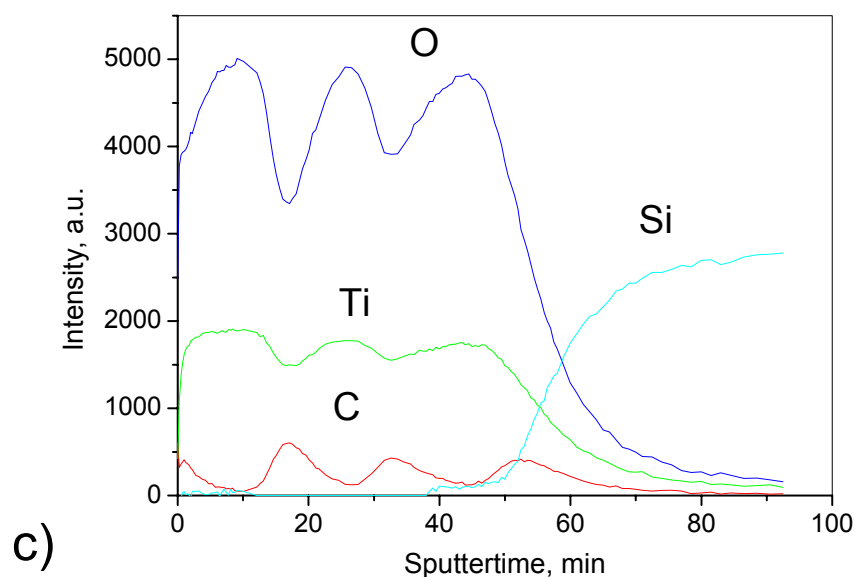
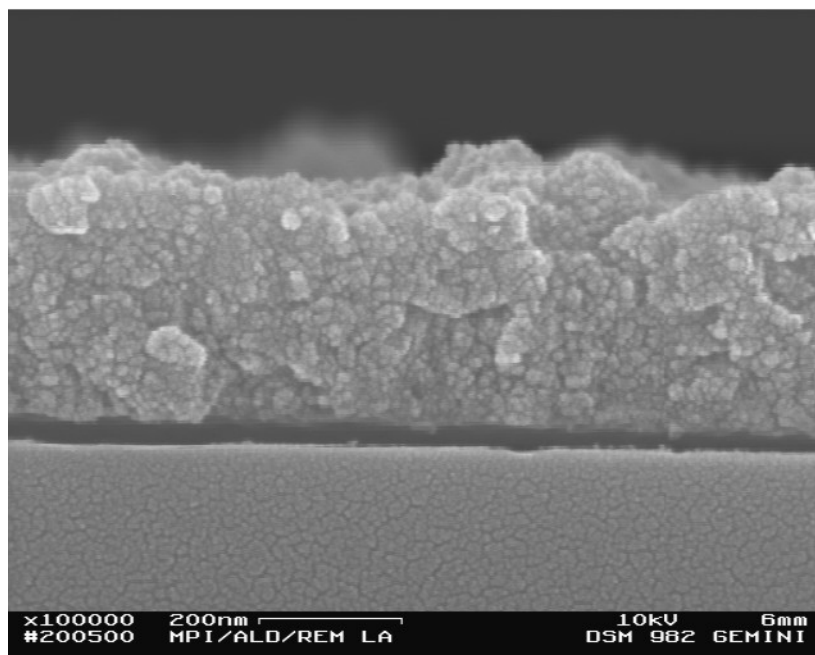


Fig. 4.27 Composition-depth profiles of (PE/TiO₂)_n composite films on Si substrates recorded by a AES: a) Si/(PE/TiO₂); b) Si/(PE/TiO₂)₂ and c) Si/(PE/TiO₂)₃; the PE layers consist of six cationic/anionic couples ((PEI/PSS)(PAH/PSS)₅); PSS and PAH were deposited from salt solution (0.5 M MnCl₂ for deposition of PSS and 1 M NaCl for deposition of PAH); the TiO₂ films were deposited by SD from an aqueous solution of 10 mM Ti(O₂)²⁺ and 30 mM HCl at 60°C for 1x2 h

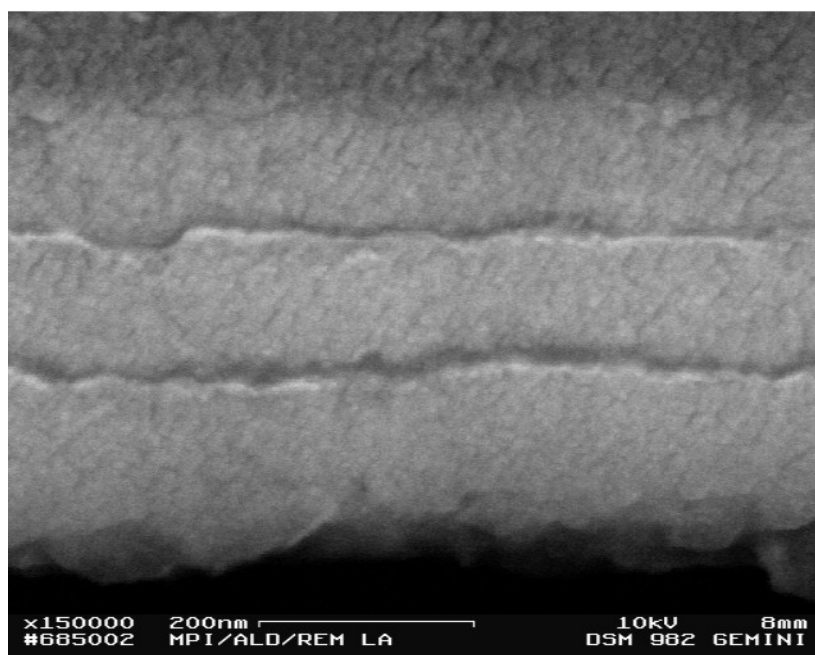
The sharp increase of the Si intensity indicates the interface of the deposited film and the substrate. One (Fig. 4.27 a), two (Fig. 4.27 b) or three (Fig. 4.27 c) periodic peaks of C, as well as of Ti and O, demonstrate the presence of a multi-layered structure of alternating C- and TiO₂-enriched layers. This result is consistent with a SEM and TEM cross-sectional analysis shown below.

4.4.3. Microstructure of the PE/TiO₂ multilayers

The microstructure of the obtained Si/(PE/TiO₂)₃ multilayer films was clearly detected on the nanometer level by the analysis of film cross-sections using SEM and TEM. SEM micrographs are shown in Fig. 4.28. Three alternate TiO₂ layers with about the same thickness can be seen on the micrograph of the polished sample (Fig. 4.28 b). The film is detached from the Si substrate due to the process of specimen cross-section preparation (see chapter 3.2.4).



a)



b)

Fig. 4.28 SEM cross-section images of a $\text{Si}/(\text{PE}/\text{TiO}_2)_3$ multilayer film: a) unpolished and b) polished sample; the PE layers consist of six cationic/anionic couples $((\text{PEI}/\text{PSS})(\text{PAH}/\text{PSS})_5)$, where PSS and PAH were deposited from salt solution (0.5 M MnCl_2 for deposition of PSS and 1 M NaCl for deposition of PAH); the TiO_2 films were deposited by the SD from an aqueous solution of 10 mM $\text{Ti}(\text{O}_2)^{2+}$ and 30 mM HCl at 60°C for 1x2 h

Transmission electron microscopy micrographs presented in Fig 4.29 reveal clearly the three alternate bilayers: The organic and inorganic layers appear as bright and dark layers with a thickness of 25 nm and 125 nm, respectively. The somewhat blurred interfaces between the two types of layers indicate a sizeable interpenetration between TiO_2 and the organic PE component. The constituents of the organic, polyelectrolyte layers (PEI, PSS and PAH) cannot be distinguished on the images due to their well interpenetration.

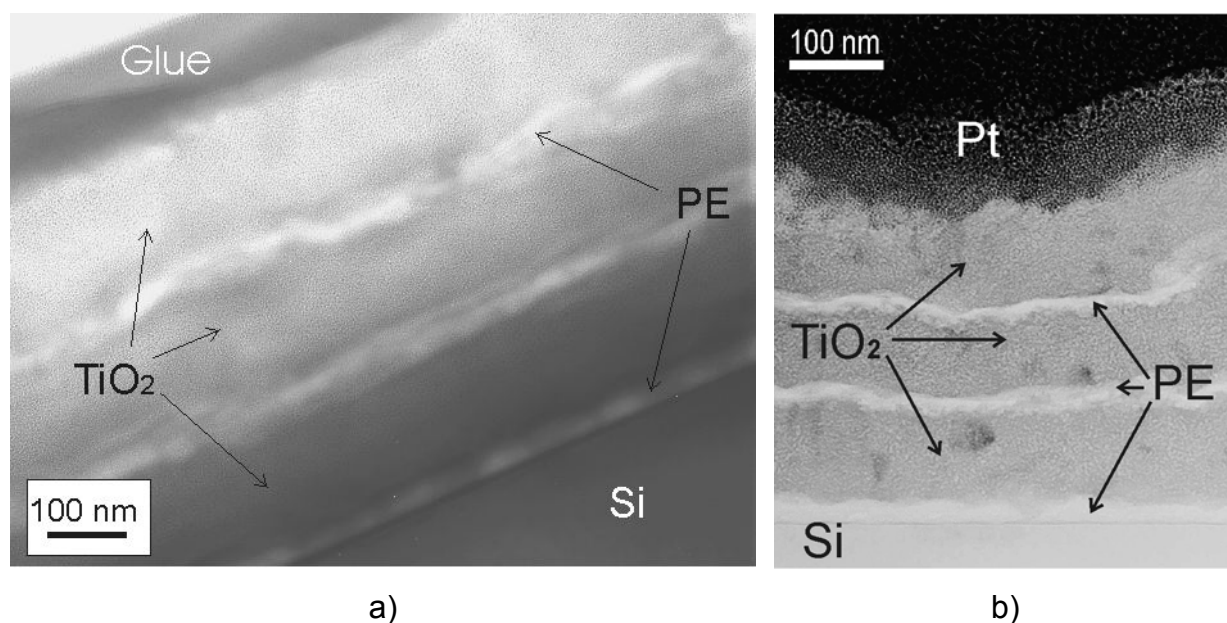


Fig. 4.29 TEM images of a $\text{Si}/(\text{PE}/\text{TiO}_2)_3$ multilayer film. The samples were prepared by a) conventional and b) FIB preparation; the PE layers consist of six cationic/anionic couples ((PEI/PSS)(PAH/PSS)₅); PSS and PAH were deposited from salt solution (0.5 M MnCl_2 for deposition of PSS and 1 M NaCl for deposition of PAH); the TiO_2 films were deposited by SD from an aqueous solution of 10 mM $\text{Ti}(\text{O}_2)^{2+}$ and 30 mM HCl at 60 °C for 1x2 h

The analytical TEM investigations were performed using energy-dispersive X-ray spectroscopy (EDX) and electron-energy loss spectroscopy (EELS).

Bright field scanning transmission electron microscopy (BF-STEM) and high angle annular dark field (HAADF) images of a Si/(PE/TiO₂)₃ multilayer film are shown in Fig. 4.30. In the BF-STEM image the organic layers appear brighter compared to the inorganic part. In scanning transmission electron microscopes (STEM) the annular detector is used, which collects electrons that have been scattered through relatively large angles. Applying the Z contrast imaging technique (HAADF detector), the atoms with higher Z number appear brighter.

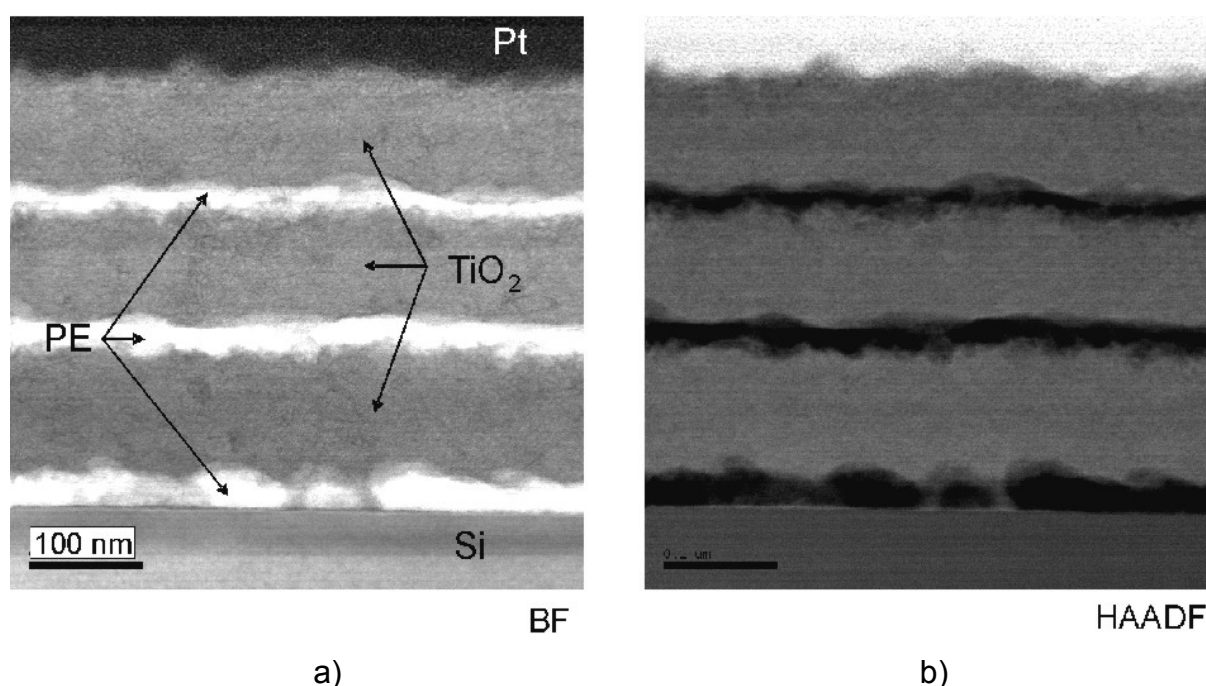


Fig. 4.30 STEM images of Si/(PE/TiO₂)₃ multilayer film: a) BF-STEM; b) HAADF; the PE layers consist of six cationic/anionic couples ((PEI/PSS)(PAH/PSS)₅), where PSS and PAH were deposited from salt solution (0.5 M MnCl₂ for deposition of PSS and 1 M NaCl for deposition of PAH); the TiO₂ films were deposited by the SD from an aqueous solution of 10 mM Ti(O₂)²⁺ and 30 mM HCl at 60°C for 1x2 h

The spectra shown in Fig. 4.32 are attributed to the bulk TiO₂ layer (Fig. 4.31 a, point 1) and to two areas of the polymer layer (Fig. 4.31 a, points 2 and 3).

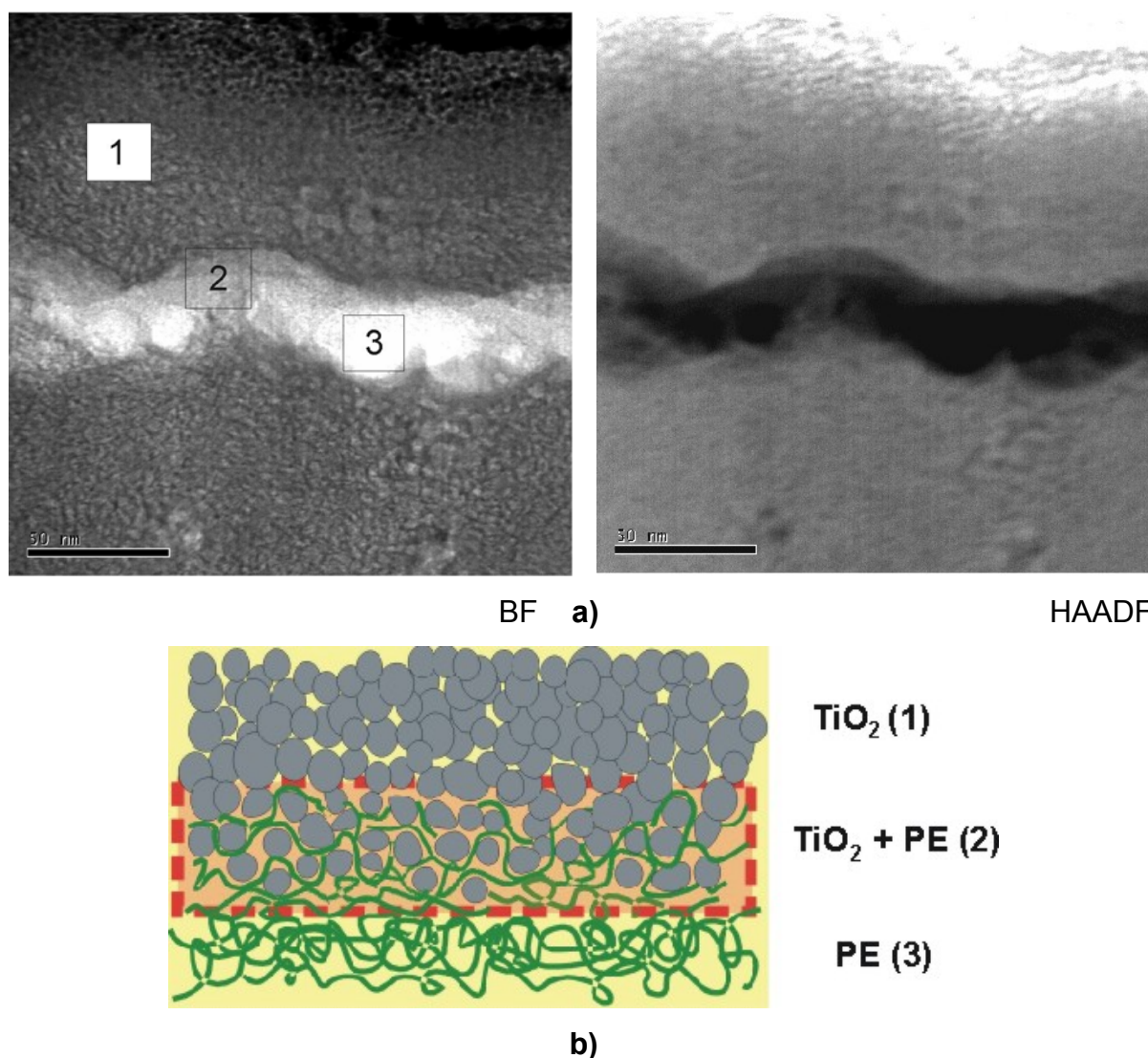


Fig. 4.31 Penetration of TiO_2 into the polyelectrolyte layer: a) STEM images; b) schematic presentation of mixed layers: (1) TiO_2 layer, (2) dense PE layer, (3) penetrated PE layer. The film investigated here is identical with the one shown in Fig. 4.30.

EDX spectra that correspond to the bulk TiO_2 layers show the presence of titanium and oxygen peaks (Fig. 4.32 a). The spectra that belong to the dense polyelectrolyte layer show that the main constituent is carbon (Fig. 4.32 b and c). Sulfur and oxygen are also detectable in the polymer layer, because they are constituents of the PSS. Apart from that, the EDX spectra that correspond to the grey area of Fig. 4.31 a (point 2) show also the presence of titanium which can be attributed to the penetration of TiO_2 into the polyelectrolyte layer, whereas the spectra taken at the brighter portion of the organic layer does not show any TiO_2 . Thus obviously the organic layer consists of two layers: one next to TiO_2 which contains penetrated TiO_2 particles and one in the centre which doesn't, as shown schematically in Fig. 4.31 b. The presence of Ga in all EDX spectra is caused by the FIB specimen preparation

and the Si peak probably appears due to the sputtering of the Si substrate during the specimen preparation.

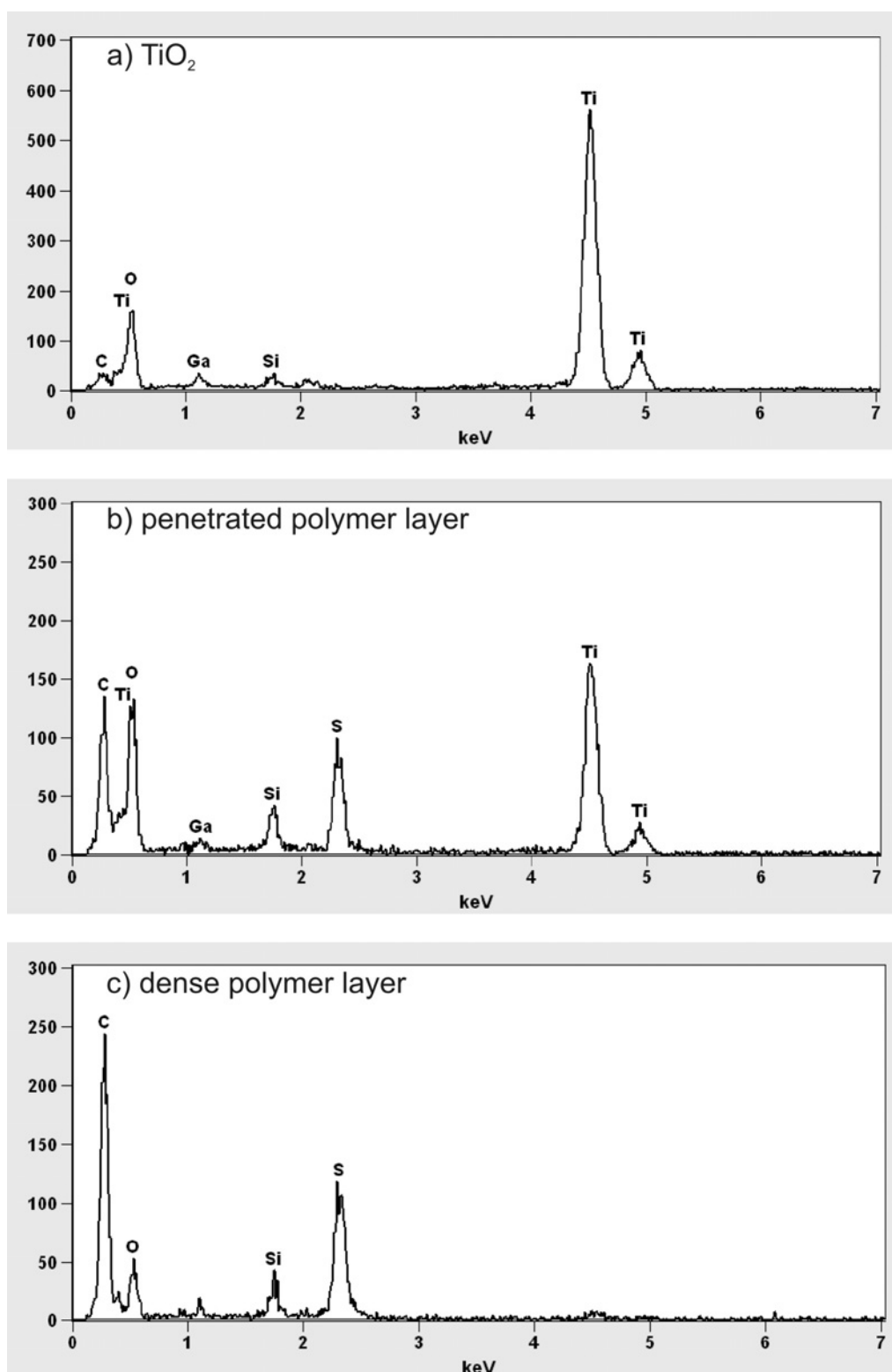


Fig. 4.32 EDX spectra recorded for a) TiO₂ layer; c) penetrated PE layer and c) dense PE layer; the PE layers consist of six cationic/anionic couples ((PEI/PSS)(PAH/PSS)₅); PSS and PAH were deposited from salt solution (0.5 M MnCl₂ for deposition of PSS and 1 M NaCl for deposition of PAH); the TiO₂ films were deposited by SD from an aqueous solution of 10 mM Ti(O₂)²⁺ and 30 mM HCl at 60°C for 1x 2 h

Further analytical TEM investigations of PE/TiO₂ multilayers were performed using EELS. EELS complements EDX through better detection of the light elements, improved spatial resolution and analytical sensitivity. Since the energy resolution of EELS spectrometer is very good, the energy-loss spectrum contains informations about the specimen that are in addition to its basic elemental chemistry.

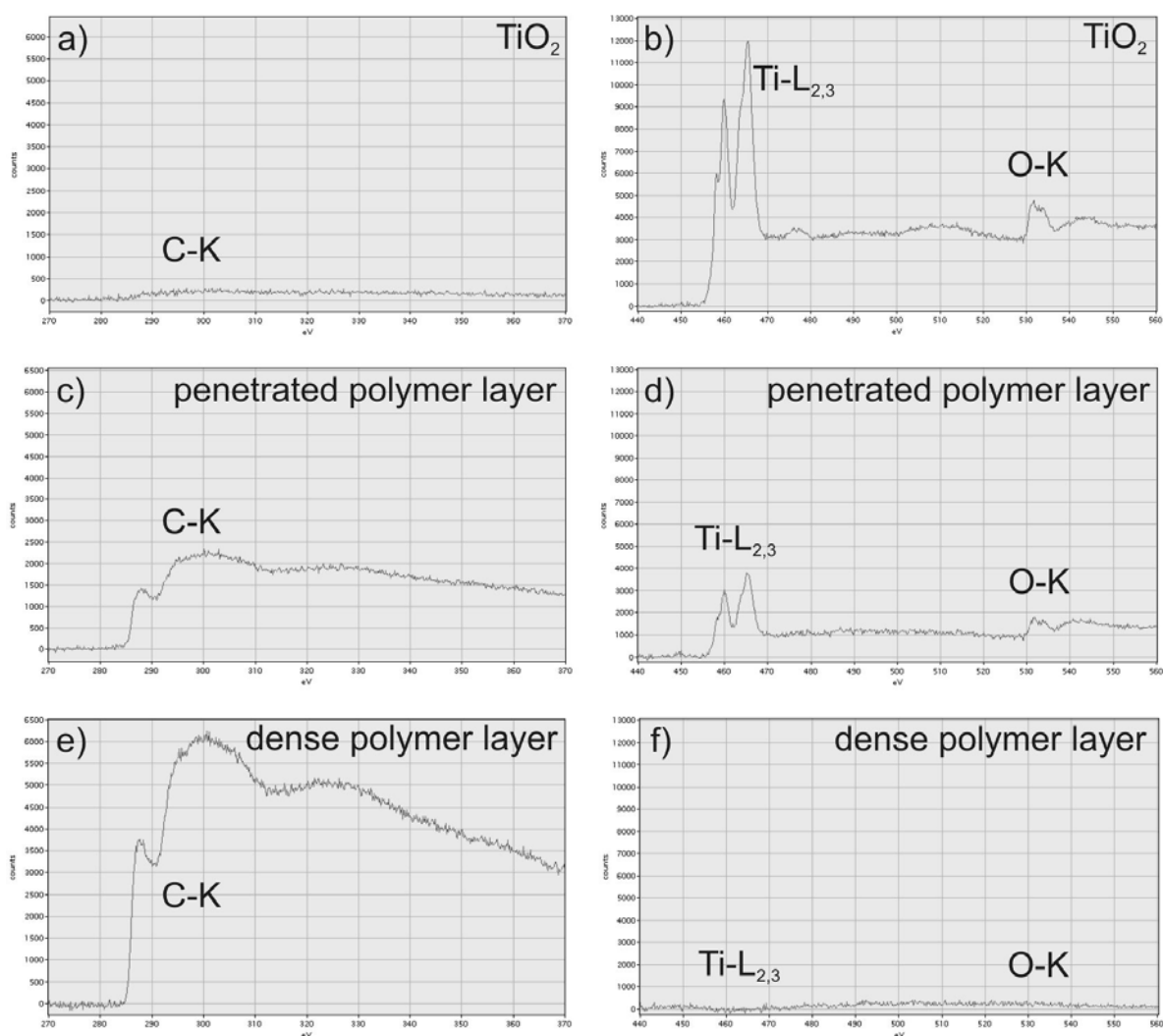


Fig. 4.33 EEL spectra of C-K, Ti-L_{2,3} and O-K edges recorded in: a,b) TiO₂ layer; c,d) penetrated polymer layer; e,f) dense polymer layer; the PE layers consist of six cationic/anionic couples ((PEI/PSS)(PAH/PSS)₅); PSS and PAH were deposited from salt solution (0.5 M MnCl₂ for deposition of PSS and 1 M NaCl for deposition of PAH); the TiO₂ films were deposited by SD from an aqueous solution of 10 mM Ti(O₂)²⁺ and 30 mM HCl at 60°C for 1x2 h

The EEL spectra that correspond to the TiO₂ layer show the presence of the Ti-L_{2,3} and O-K edges (Fig. 4.33 a and 4.33 b). In the dense polymer layer (Fig. 4.31) the recorded spectra show the presence of the C-K edge (Fig. 4.33 e). According to the literature data [1996 EGe], this C-K edge corresponds to the C-K edge of amorphous

carbon. The spectra which correspond to the penetrated polyelectrolyte layer (Fig. 4.33 c and 4.33 d) show the presence of the C-K edge and apart from that also the presence of Ti-L_{2,3} and O-K edges, which is in agreement with the EDX results (Fig. 4.32).

Additionally, energy loss near edge fine structures (ELNES) studies of the Ti-L_{2,3} and O-K edges (Fig. 4.35) were employed to determine the modification of TiO₂ within the layers.

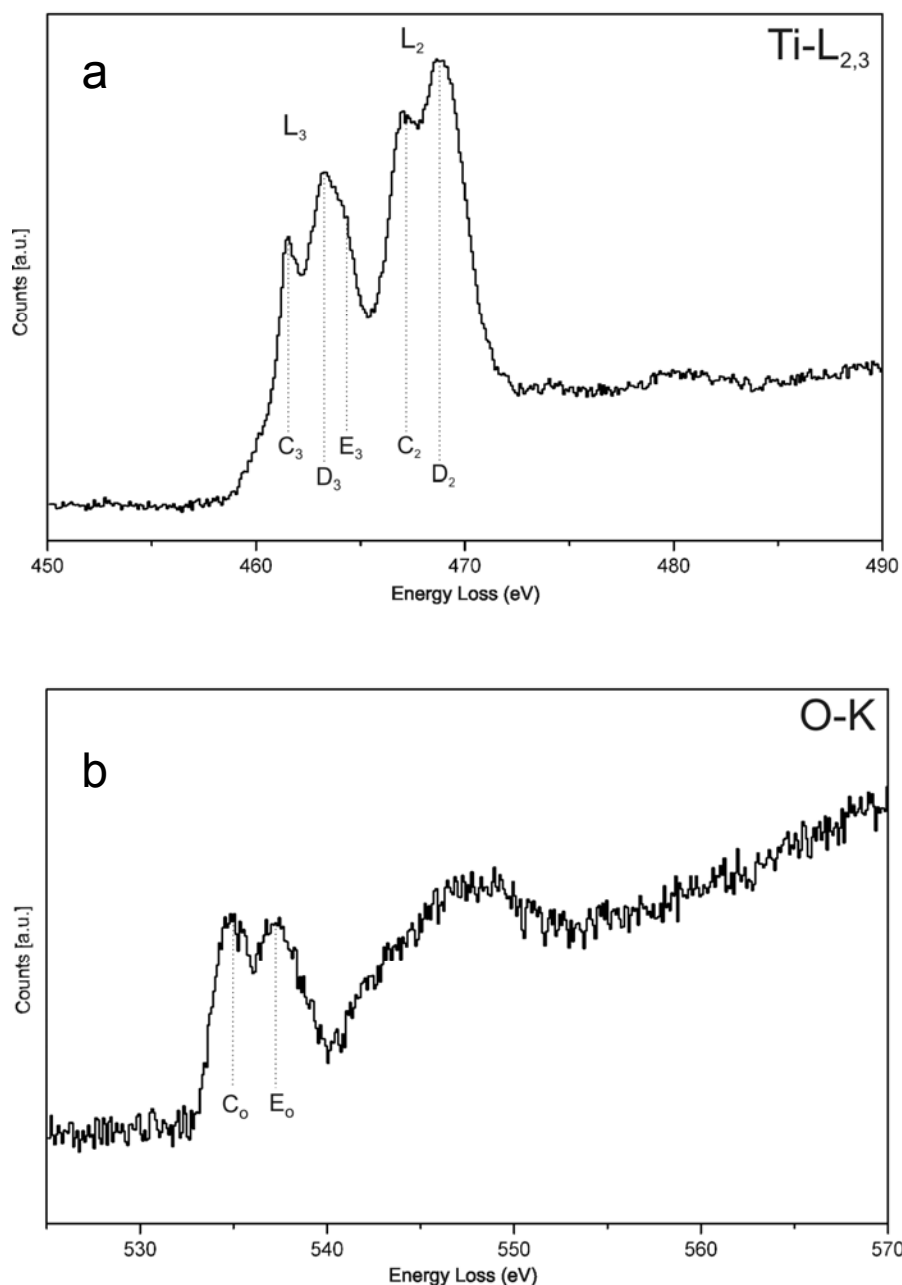


Fig. 4.35 ELNES spectra of a) Ti-L_{2,3} and b) O-K edges recorded in the TiO₂ layer; the TiO₂ films were deposited by the SD from an aqueous solution of 10 mM Ti(O₂)²⁺ and 30 mM HCl at 60°C for 1x2 h (system Si/(PE/TiO₂)₃). The marks are corresponding to the marks present on Fig. 4.36.

The most obvious feature of the Ti-L_{2,3} edges in all TiO₂ polymorphs is the spin-orbit splitting of the L₃ and L₂ lines that are separated for approximately 5.5 eV (D₃ – D₂, Fig. 4.35 a) [1989 BSE, 2003 Mit, 2004 KBB]. The first part of the Ti-L_{2,3} edges represents the L₃ edge and the second part the L₂ edge. Additionally, the L₃ and L₂ lines are split into two peaks. For the TiO₂ modifications it is known from the literature [1989 BSE, 2003 Mit] that the second peak of the L₃ edge shows a splitting (D₃-E₃ in Fig. 4.35), which appears as a low energy shoulder in rutile, a high energy shoulder in anatase and a broad peak in brookite (Fig 4.36 a).

Experimental O-K spectra recorded in the TiO₂ layer show two main peaks (C₀, E₀) that are followed by an additional structure (Fig 4.36 b).

The electron energy-loss spectroscopy (EELS → ELNES: near edge structures) and X-ray absorption spectroscopy (XAS → XANES: near edge structures) techniques are both able to detect significant differences in edge structures irrespective of very similar environments of Ti and O atoms in different TiO₂ phases [2004 KBB]. In EELS and XAS an electron from a core state is excited into the unoccupied states, however EELS uses electron and XAS uses photon as the incident radiation. Both techniques cover the same energy range and they provide information on the unoccupied density of states therefore the results of both are comparable.

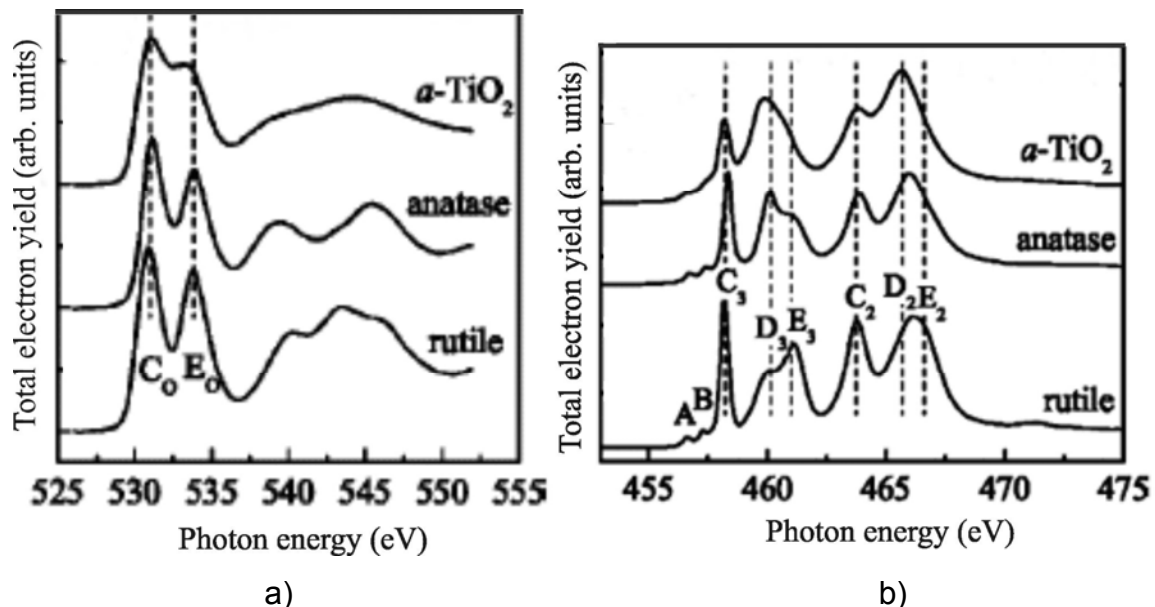


Fig. 4.36 X-ray absorption near edge structures spectroscopy (XANES) spectra for rutile, anatase and amorphous TiO₂ (*a*-TiO₂): a) TiO₂ L_{2,3}-edge and b) oxygen K-edge [2004 KBB]

According to the literature data (energy separation, intensity ratios and peak shapes) of amorphous and crystalline phases of TiO₂ shown in Fig. 4.36 [2004 KBB] and Tab. 4.2 and 4.3, the experimental spectra of Ti-L_{2,3} and O-K edges recorded in the TiO₂ layer are best corresponding to the spectrum of amorphous TiO₂ (in this investigation amorphous TiO₂ was prepared by bombardment of a (001)-oriented rutile single crystal with Xe²⁺ ions which resulted in formation of a continuous surface amorphous layer). In amorphous TiO₂ the peaks of Ti-L_{2,3} and O-K edges are broadened compared to the spectra of rutile and anatase. Such a broadening is inherent to the spectra from amorphous solids. Due to the amorphization the intensity of the E₃ peak (Ti-L_{2,3} edge) is reduced, additionally there is also a significant decrease in the distance between C₀ and E₀ peaks (O-K edge) [2004 KBB].

Obtained results are in agreement with XRD investigations presented in chapter 4.3. and confirmed the amorphous structure of TiO₂ films deposited on PE-modified silicon.

Tab. 4.2 Peak position relative to peak C₃ – values of the splitting of different features within the ELNE spectra for TiO₂ (Ti-L_{2,3} edges) in eV

Ti-L _{2,3} edges	C ₃	D ₃	E ₃	C ₂	D ₂	reference
amorphous TiO ₂	0	1.7	2.4	5.5	7.4	this work
amorphous TiO ₂	0	1.6	2.4	5.5	7.4	[2004 KBB]
rutile	0	1.8	2.9	5.6	7.5	[2004 KBB]
anatase	0	1.8	2.7	5.5	7.6	[2004 KBB]

Tab. 4.3 Peak position relative to peak C₀ – values of the splitting of different features for TiO₂ (O-K edge) in eV

O-K edge	C ₀	E ₀	reference
amorphous TiO ₂	0	2.4	this work
amorphous TiO ₂	0	2.3	[2004 KBB]
rutile	0	3	[2004 KBB]
anatase	0	2.8	[2004 KBB]

4.4.4. Crystallinity of PE/TiO₂ multilayers

High-resolution TEM studies were employed in order to determine the crystallinity of the TiO₂ layers. According to HRTEM image, taken at the very beginning of the irradiation during investigation (Fig. 4.37 a), beside very rare and small areas which can be counted as crystalline, the sample is fully amorphous.

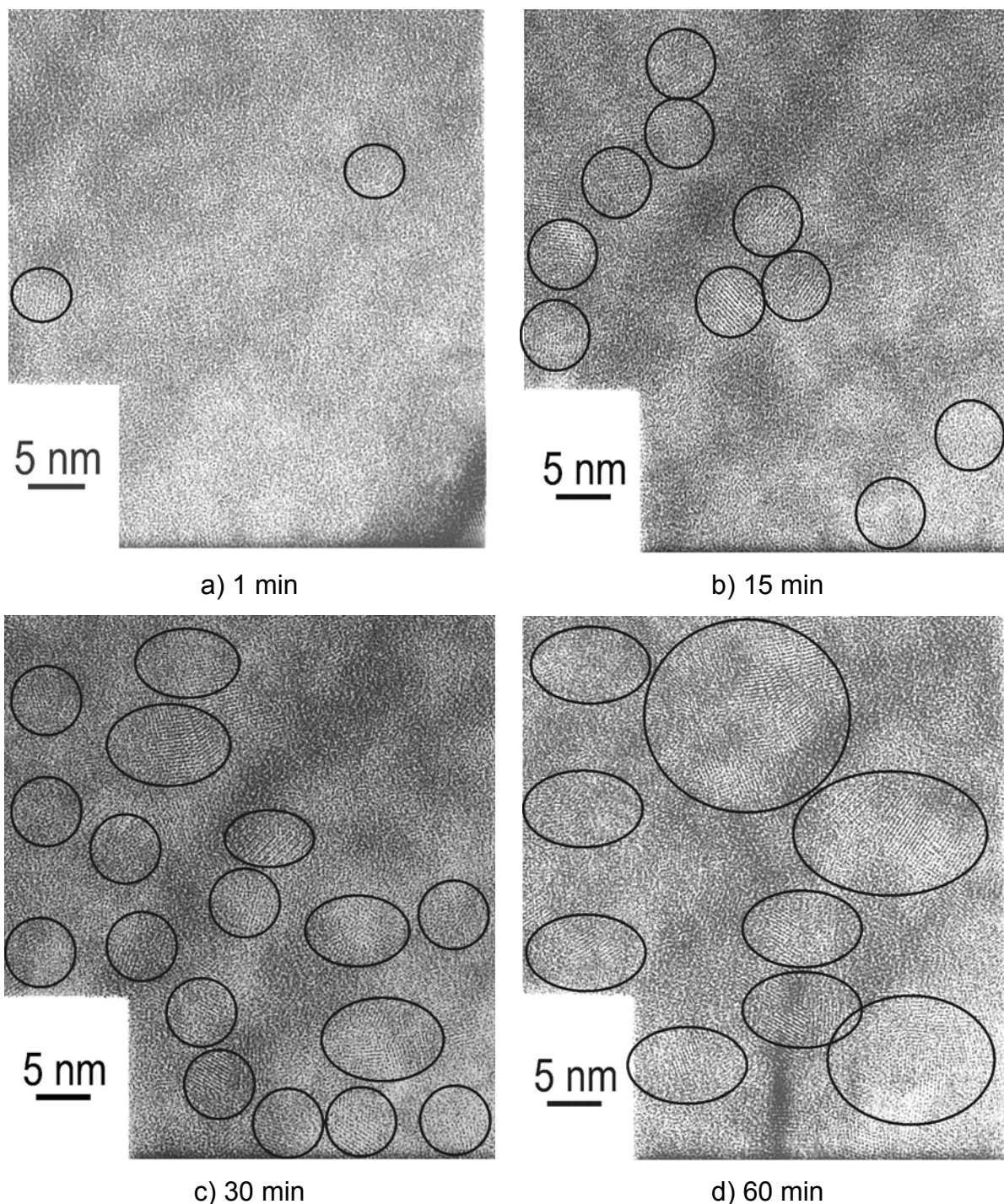


Fig. 4.37 HRTEM images of structural changes in a TiO₂ layer of a Si/(PE/TiO₂)₃ multilayer film (Fig. 4.29) due to the 400 keV electron-beam irradiation after a) 1 min; b) 15 min; c) 30 min; d) 60 min; the circles indicate the position of the formed grains;

After continuously exposing the sample to the electron-beam irradiation (electrons of 400 keV incident energy), increasing crystallization was detected with increasing time (Fig. 4.37 b-d). The number of crystallites and their size increase with irradiation time. After one hour the TiO₂ layers are composed of crystallites with about 10 – 15 nm in size embedded in an amorphous matrix (Fig. 4.37 d).

The electron beam induced crystallization can be explained by the fact that inelastic scattering of the incident electrons with electrons of the specimen are mainly responsible for the radiation damage of the specimen. As a consequence of the energy transfer by inelastic scattering, the change in chemistry and/or structure of ceramic and other materials can occur [1996 WCa].

Electron diffraction patterns of un-irradiated TiO₂ layers show diffuse rings (Fig 4.38 a), whereas electron diffraction patterns taken after 60 min of irradiation reveal a nanocrystalline structure of the TiO₂ layer (Fig 4.38 b). The ring diffraction pattern is identified as polycrystalline anatase (Tab. 4.4).

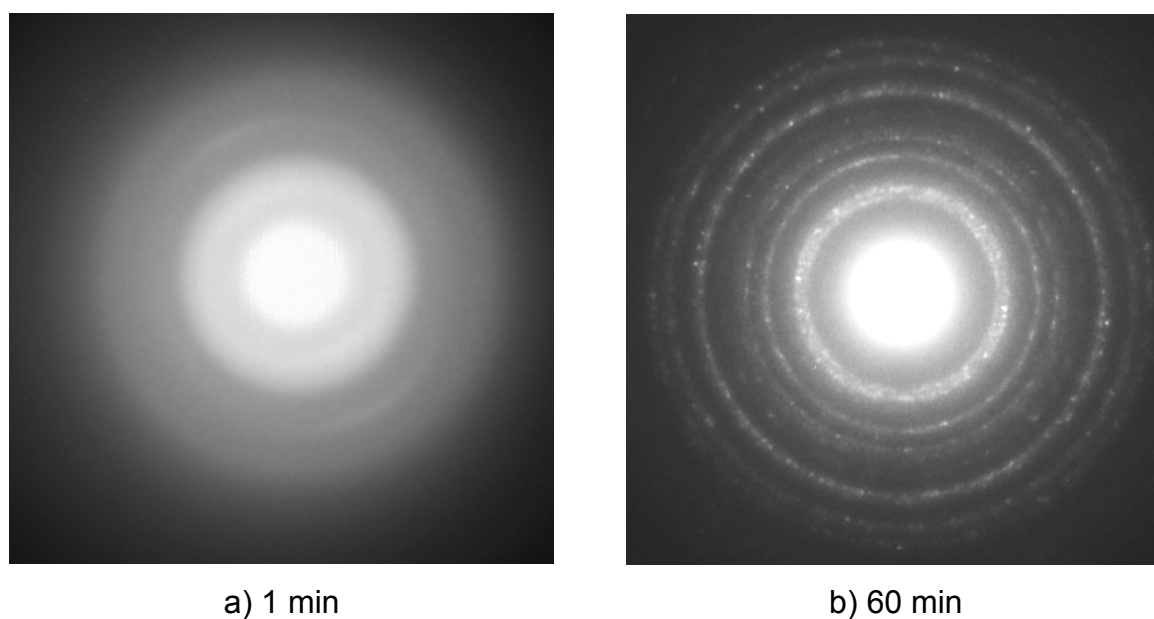


Fig. 4.38 Diffraction patterns of a TiO₂ layer of a Si/(PE/TiO₂)₃ multilayer film irradiated with a 400 keV electron beam for: a) 1 min (beginning of the irradiation); b) 60 min; the TiO₂ films were deposited by SD from an aqueous solution of 10 mM Ti(O₂)²⁺ and 30 mM HCl at 60°C for 1x2 h; the PE layers consist of six cationic/anionic couples ((PEI/PSS)(PAH/PSS)₅); PSS and PAH were deposited from salt solution (0.5 M MnCl₂ for deposition of PSS and 1 M NaCl for deposition of PAH)

Tab 4.4 Electron diffraction pattern (Fig. 4.38 b) analysis of a TiO₂ layer in a Si/(PE/TiO₂)₃ multilayer film irradiated with a 400 keV electron beam for 60 min;

electron diffraction	X-ray powder diffraction pattern of anatase (JCPDS file no. 21-1272)		
measured d (nm)	d (nm)	rel. intensity	h k l
0.356	0.352	100	101
0.246	0.243	10	103
n.a	0.238	20	004
0.225	0.233	10	112
0.187	0.189	35	200
0.169	0.170	20	105
0.164	0.167	20	211
n.a.	0.149	4	213
0.147	0.148	14	204

Electrons of 100 keV incident energy within a VG STEM electron microscope also induce the crystallization of as-deposited TiO₂ films as is shown in Fig. 4.39, 4.40 and 4.41. At the very beginning of investigation again no crystals could be detected, whereas with increasing time of irradiation increased crystallization is visible. After 20 min the structure of the irradiated area is almost completely crystalline, with grain sizes of about 10 nm, as it is shown in dark field HRTEM images (Fig. 4.41).

An explanation why radiation induced crystallization goes more slowly in case of 400 keV irradiation is in accordance with the fact that the probability for inelastic scattering becomes smaller at higher voltage, so the effect of specimen damage can be reduced using higher voltages in order to lower the cross-section of the electron-electron interaction [1996 WCa].

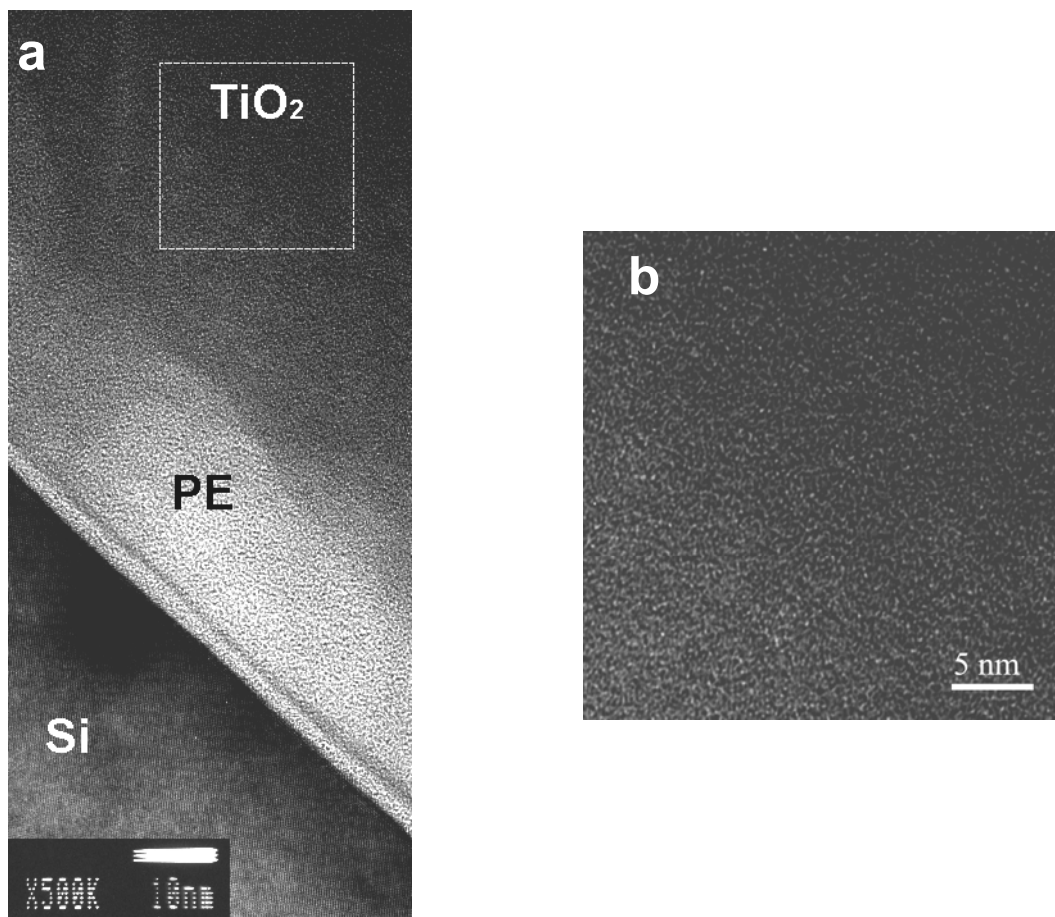


Fig. 4.39 a) HRTEM image of a Si/(PE/TiO₂) layer of a Si/(PE/TiO₂)₃ multilayer film at very short time of irradiation by electron beam; b) enlarged image of the area shown in (a); the PE layers consist of six cationic/anionic couples ((PEI/PSS)(PAH/PSS)₅); PSS and PAH were deposited from salt solution (0.5 M MnCl₂ for deposition of PSS and 1 M NaCl for deposition of PAH); the TiO₂ films were deposited by SD from an aqueous solution of 10 mM Ti(O₂)²⁺ and 30 mM HCl at 60°C for 1x2 h

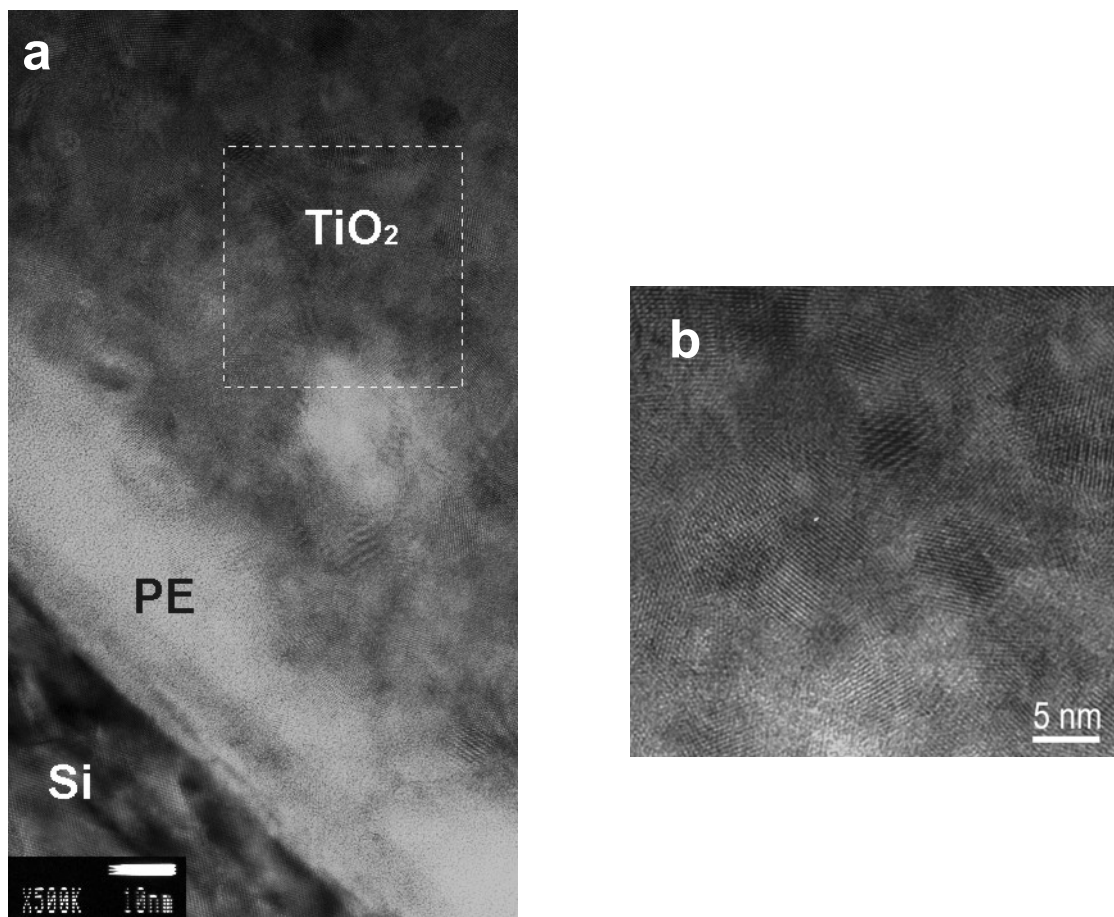


Fig. 4.40 a) HRTEM image of a Si/(PE/TiO₂) layer of a Si/(PE/TiO₂)₃ multilayer film irradiated 20 min by an electron beam (100 keV); b) enlarged image of the area shown in (a); the PE layers consist of six cationic/anionic couples ((PEI/PSS)(PAH/PSS)₅); PSS and PAH were deposited from salt solution (0.5 M MnCl₂ for deposition of PSS and 1 M NaCl for deposition of PAH); the TiO₂ films were deposited by SD from an aqueous solution of 10 mM Ti(O₂)²⁺ and 30 mM HCl at 60°C for 1x2 h

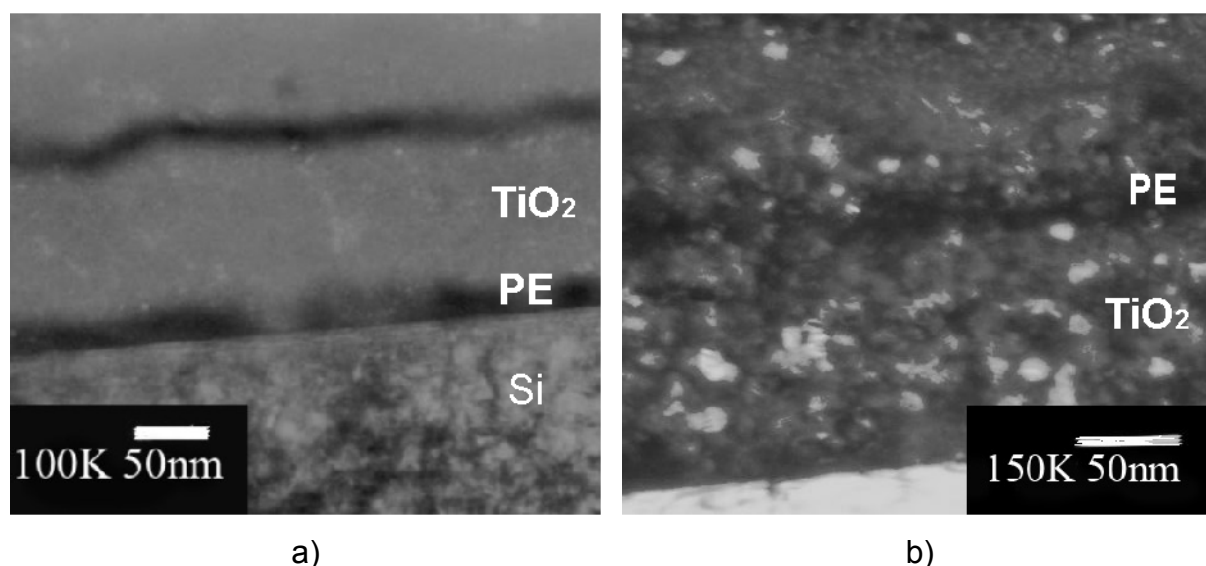


Fig 4.41 Dark field HRTEM images of Si/(PE/TiO₂)₃ multilayer film: a) before irradiation by an electron beam; b) after 20 min of irradiation by an electron beam (100 keV); the PE layers consist of six cationic/anionic couples ((PEI/PSS)(PAH/PSS)₅); PSS and PAH were deposited from salt solution (0.5 M MnCl₂ for deposition of PSS and 1 M NaCl for deposition of PAH); the TiO₂ films were deposited by SD from an aqueous solution of 10 mM Ti(O₂)²⁺ and 30 mM HCl at 60°C for 1x2 h

Crystallization of the amorphous material under the electron beam irradiation in as-grown ZrO₂ films deposited by the CBD was also reported by Roddatis et al. [2002 RSJ]. In this investigation, the irradiation of ZrO₂ films was carried out with 200 and 400 keV incident energy electron beam. The number of crystallites and their size also increase with prolonged irradiation time (up to 10 nm after 20 min). The radiation damage took place more rapidly also under the electron irradiation with the lower (200 keV) incident energy than with the higher one (400 keV), like in this investigation (100 keV compared to 400 keV).

ZrO₂ films are even more electron beam sensitive than the TiO₂ films [2002 RSJ]. They crystallized more rapidly, in less than 1 min of irradiation. In that case HRTEM images of as-deposited state of films can only be obtained if the samples are cooled to 4.2 K during the investigation.

4.5. Mechanical properties of the PE/TiO₂ multilayers

The nanoindentation technique was employed for estimating the mechanical properties of the TiO₂ single layers and PE/TiO₂ multilayers to investigate the influence of incorporation of an organic phase on the mechanical performances of the titania films.

The employment of the technique does not require removing the film from the substrate. It was found that the influence of the substrate is limited to indentation depths larger than 20% of the total film thickness [2000 WLL]. Since the films deposited in the thickness range from 300 to 500 nm, the evaluation of the nanoindentation data, which takes these limitations into account, lay in the indentation depth from ~60 nm for film thickness of 300 nm to ~100 nm for film thickness of 500 nm, which was always fulfilled.

To prove the accuracy of the technique within the required penetration depth, nanoindentation experiments were performed firstly on bare Si substrates. The AFM image of an indentation profile on Si substrate is shown on Fig. 4.41.

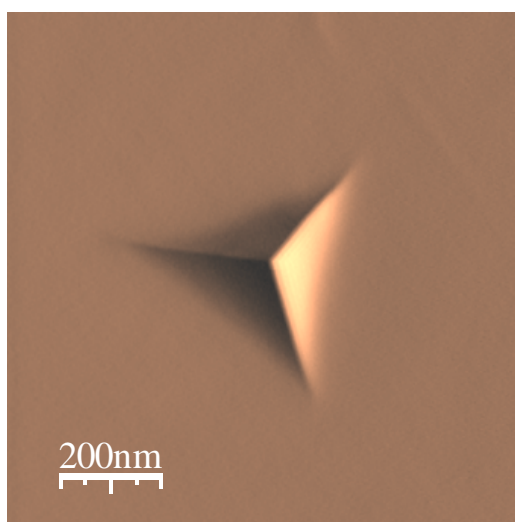
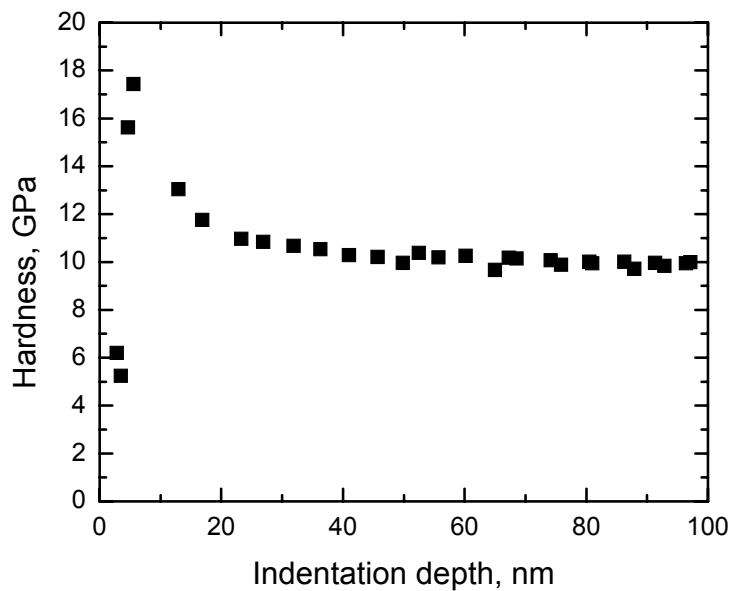


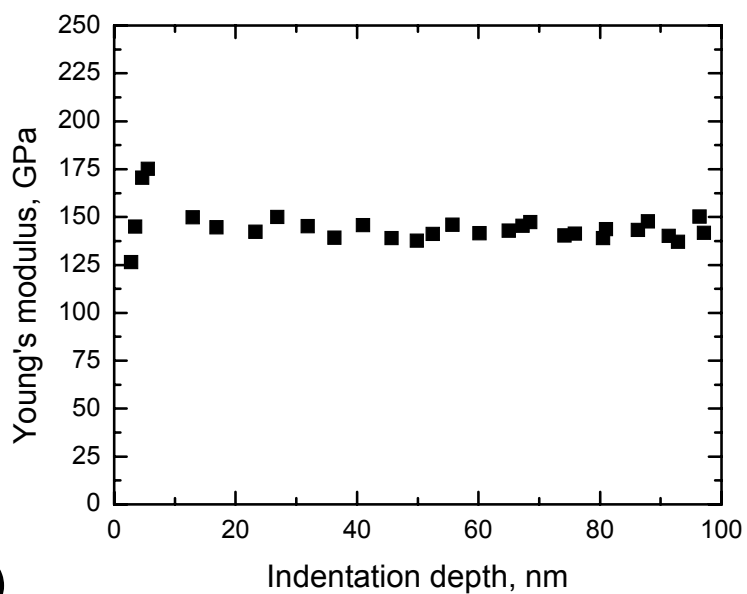
Fig. 4.41 AFM image of indentation profile on a Si substrate

Fig. 4.42 presents the extracted hardness (Fig. 4.42 a) and Young's modulus (Fig. 4.42 b) as a function of the indentation depth for a bare Si substrate. The estimated values of hardness (~10 GPa) and Young's modulus (~140 GPa) are in good agreement with literature data [2000 SWC]. The results show that measurements with penetration depths more than 20 nm are reliable. Deviations for the penetration

depths smaller than 20 nm can be attributed to the roughness effect of indentation size.



a)



b)

Fig. 4.42 Hardness (a) and Young's modulus (b) as a function of the penetration depth calculated from nanoindentation data obtained for a bare Si substrate

4.5.1. Influence of residual water on the mechanical properties of the TiO₂ layers

Due to condensation, films produced by the CBD process contain chemically and physically bound water [2000 PKN, 2001 NDe]. Since such residual water can affect the mechanical properties of the films, it should be removed. As temperatures over 100°C can destroy the polymer interlayers, the films have been dried in air at ambient temperature for 1 month.

TiO₂ single layer films were deposited on a Si substrate, with the thickness of ~300 nm, determined by SEM cross-section (Fig. 4.1). Nanoindentation experiments have been performed on as-deposited films and films aged for 1 month at room temperature.

The AFM image of a typical indentation impression of a single layer dried TiO₂ film with a thickness of 300 nm is shown on Fig. 4.43 a. Indentations in multilayered films look quite similar (Fig. 4.43 b).

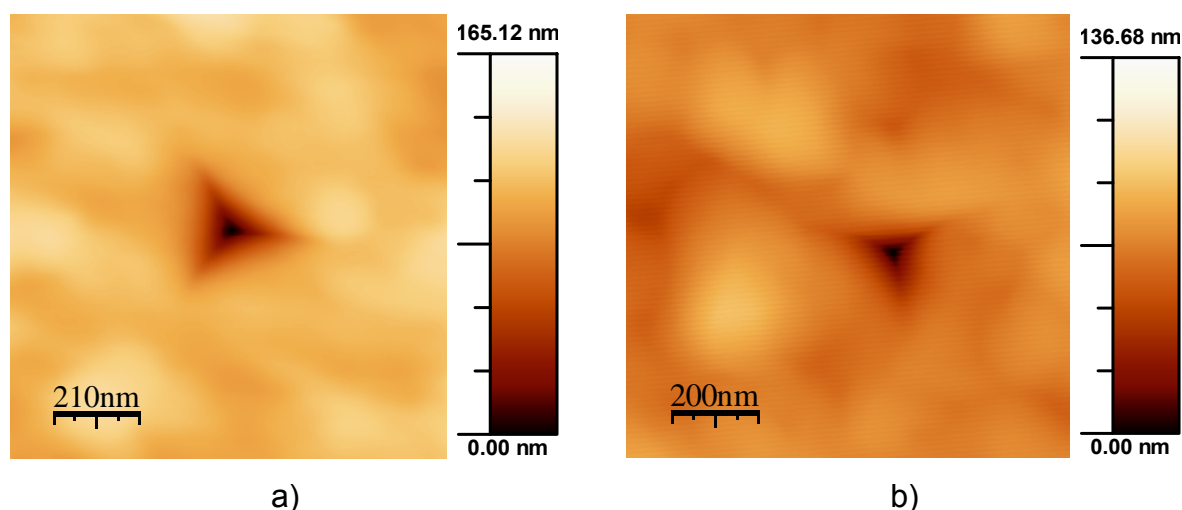


Fig. 4.43 AFM image of indentation impression on a) single-layer TiO₂ film deposited by SD on a Si substrate from an aqueous solution of 10 mM Ti(O₂)²⁺ and 30 mM HCl at 60°C for 3x2 h and b) (PE/TiO₂)₃ multilayer film; the PE layers consist of six cationic/anionic couples ((PEI/PSS)(PAH/PSS)₅) with thickness of 25 nm; the TiO₂ films were deposited by the SD from an aqueous solution of 10 mM Ti(O₂)²⁺ and 30 mM HCl at 60°C for 1x2 h with thickness of 125 nm

Fig. 4.44 presents measured hardness and Young's modulus of as-deposited and dried films as a function of indentation depth. In order to avoid the influence of the surface roughness (up to 20 nm for the present samples) as well as the influence of the substrate, the nanoindentation data were evaluated in the indentation depth range 20 – 60 nm, corresponding to 20% of the film thickness of ~300 nm.

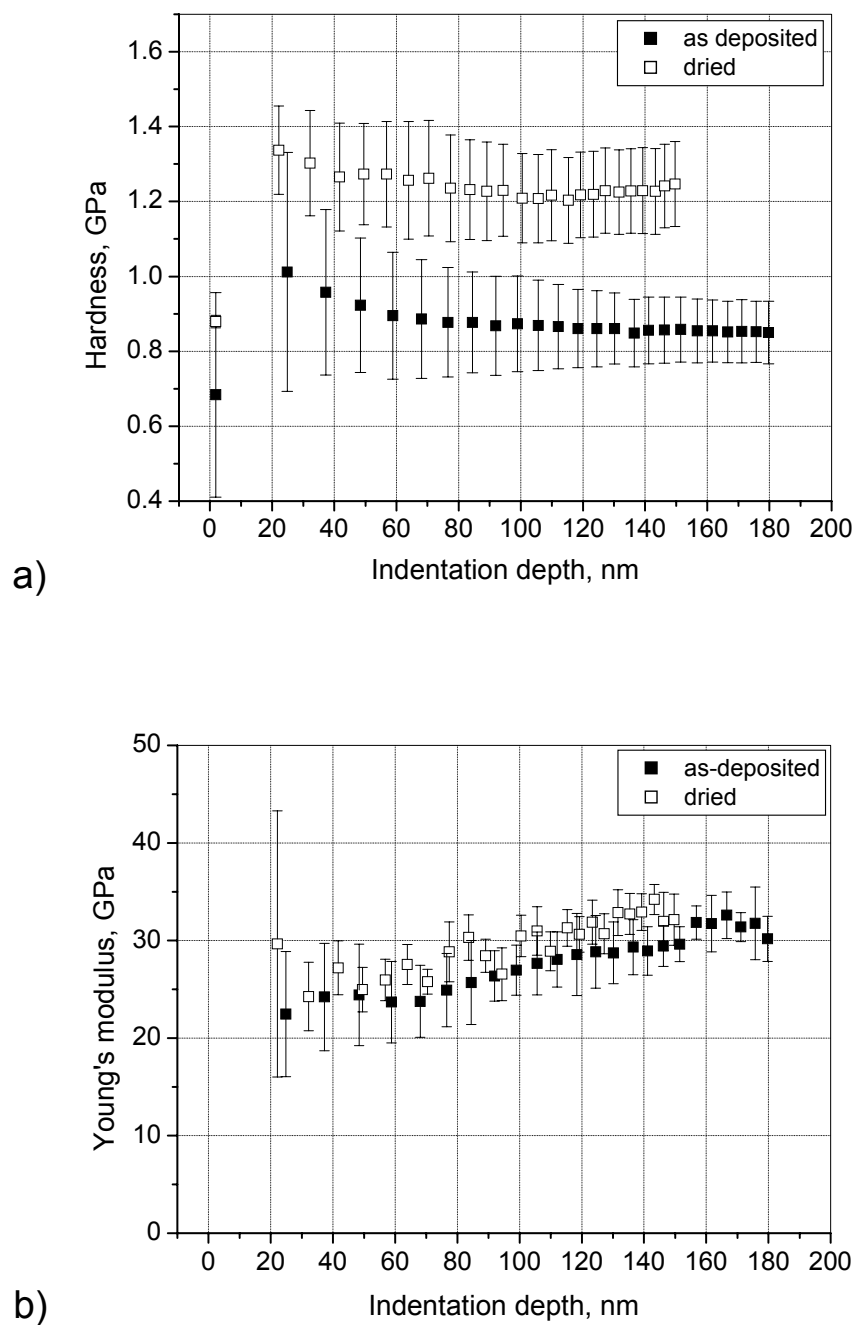


Fig. 4.44 Hardness (a) and Young's modulus (b) as a function of the penetration depth calculated from nanoindentation data obtained for as-deposited and dried TiO₂ films; the TiO₂ films were deposited on a Si by the SD from an aqueous solution of 10 mM Ti(O₂)²⁺ and 30 mM HCl at 60°C for 3x2 h with a thickness of 300 nm

As can be seen, the hardness increased from ~0.9 GPa to ~1.2 GPa, by drying, what can be attributed to the removal of chemically and physically bound residual water from the film during the drying. The Young's modulus seems also to be affected by the drying process, and it increases from 24 to 27 GPa.

The dependence of the hardness on the indentation depth is obviously weaker than that of the Young's modulus. This can be understood from the fact that for the same indentation depth, the elastic field under the indenter extends further into the film than the plastic deformation field [1997 Nix].

The slight hardness decrease observed for both types of film with increasing indentation depth may indicate the presence of a density gradient in deposited films. In the CBD-films, a gradient with density decreasing from the surface toward the interface to the substrate may be formed like in sol-gel derived coatings, i.e., via more restricted shrinkage and slower drying rate at the interface compared with the relative free shrinkage and rapid solvent evaporation at the surface [1997 Fra].

By contrast, the density gradient affects only weakly the Young's modulus.

Both hardness and Young's modulus of the TiO₂ film are inferior to bulk single-crystalline TiO₂ [2000 Ash], due to its structure which is composed of amorphous TiO₂. The mechanical properties however are relatively close to the properties of sol-gel derived TiO₂ films (hardness values of about 1.2 GPa for as-deposited films and 1.5 GPa for films heat-treated at 550°C) [2000 OBJ], despite the lower deposition temperature of CBD technique (Tab. 4.5).

Tab. 4.5 Hardness (H) and Young's modulus (E) of bulk TiO₂ [2000 Ash], sol-gel derived TiO₂ [2000 OBJ] and CBD-derived TiO₂ layers (this work, Fig. 4.44)

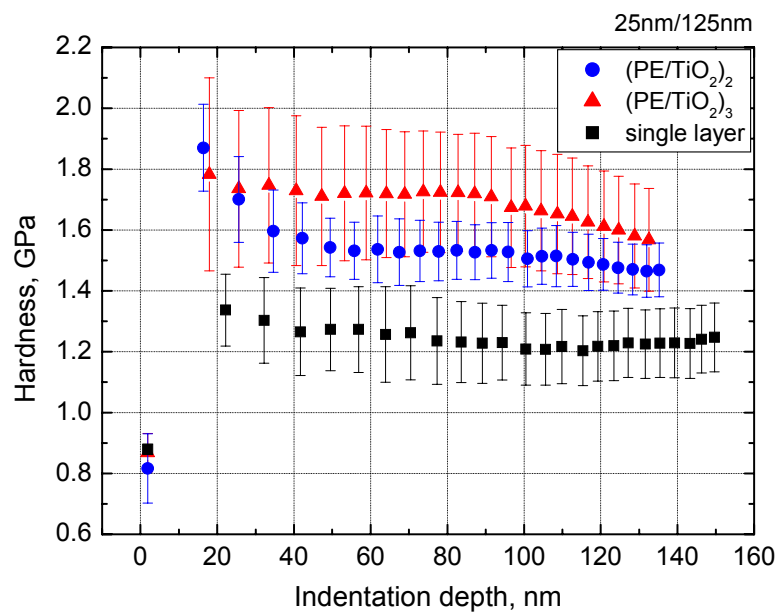
	H, GPa	E, GPa
bulk TiO ₂	11	282
sol-gel derived TiO ₂ :		
as-deposited	1.2	55-65
annealed at 550°C	1.5	85
CBD-derived TiO ₂ (this work):		
as-deposited	0.9	24
dried	1.2	27

4.5.2. Influence of the incorporation of the organic phase on the mechanical properties of the TiO₂ layers

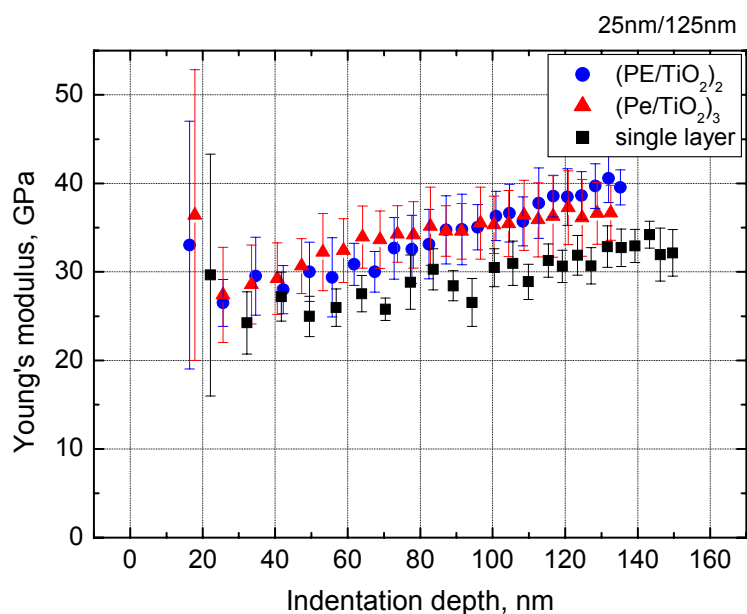
The hardness and Young's modulus of films consisting of two and three PE/TiO₂ couples are shown in Fig. 4.45. The multilayers have a total thickness (determined by the TEM cross-sections) of ~300 nm and ~450 nm, respectively. Also included are data of TiO₂ single layer films taken from Fig. 4.44. The surface roughness of the samples is in the range 20-30 nm (Fig. 4.25). Hence, the nanoindentation data obtained at shallow depth (up to 20 nm) are affected by the surface roughness of the sample. Therefore, the evaluation of the nanoindentation data lay in the indentation depth range between 20 and 60 nm (corresponding up to 20% of the total film thickness).

The incorporation of the organic PE layers causes an increase of hardness from ~1.2 GPa for the hardness of the TiO₂ single layers to ~1.5 and ~1.7 GPa for the hardness of (PE/TiO₂)₂ and (PE/TiO₂)₃ multilayer films, respectively. It can be seen that the hardness increases with increasing the number of bilayers from 2 to 3. This can be explained by the interface effect. In nanoscale materials, the hardness usually increased with increasing interface quantity [1998 HLL]. In comparison, the Young's modulus exhibits a weaker, but noticeable increase from ~27 GPa to ~30 GPa. The weaker influence of the film composition on Young's modulus is in accordance with observation made on other multilayered films composed of tough and more soft materials [2002 MRL]. This finding has been attributed to the fact that the multilayer structure mainly improves the plastic behavior resulting in hardening, whereas the elastic properties are only weakly affected.

It is furthermore noteworthy that the multilayer films exhibit a larger variation in the hardness and Young's modulus from indent to indent than the single layer film. This difference reflects the more inhomogeneous thickness and interfacial roughness originating from the incorporated polyelectrolyte layers (RMS 26 and 29 nm for (PE/TiO₂)₂ and (PE/TiO₂)₃ multilayer films, respectively, Fig. 4.26) compared for the corresponding value of the single layer TiO₂ film (15 nm, Fig. 4.43).



a)



b)

Fig. 4.45 Hardness (a) and Young's modulus (b) as a function of the penetration depth calculated from the nanoindentation data obtained for a single layer TiO₂ and (PE/TiO₂)₂ and (PE/TiO₂)₃ multilayer film; the PE layers consist of six cationic/anionic couples ((PEI/PSS)(PAH/PSS)₅) with thickness of 25 nm; PSS and PAH were deposited from salt solution (0.5 M MnCl₂ for deposition of PSS and 1 M NaCl for deposition of PAH); the TiO₂ films were deposited by the SD from an aqueous solution of 10 mM Ti(O₂)²⁺ and 30 mM HCl at 60°C for 1x2 h with thickness of 125 nm; the single layer TiO₂ film was deposited on a Si by SD from an aqueous solution of 10 mM Ti(O₂)²⁺ and 30 mM HCl at 60°C for 3x2 h

The enhanced performance of the multilayered composites in comparison to the monolithic TiO_2 films can be attributed to two different mechanisms. First, the combination of a soft (PE layers) and a harder (TiO_2 layers) material of different shear modulus results in increased external stresses required to drive the deformation field from one material to another [1970 Koe]. For the polymer layers within the present samples, a shear modulus of approximately 20 MPa can be assumed in accordance with [2000 Ash], while a value of 10.8 GPa is calculated for the TiO_2 layer from measured Young's modulus by using the known relation between Young's modulus and shear modulus. Hardening by differences in shear modulus has also been reported for polycrystalline multilayer coatings, where the movement of dislocations across the interface is blocked [2004 KBK]. Hardness enhancement depends on interface characteristics such as sharpness (or thickness) and homogeneity because the interface is broadened by interpenetration between the two materials comprising the multilayer.

The presence of the hybrid interlayer, where TiO_2 particles are interpenetrated into polymer film (Fig. 4.30), is essential for the second hardening mechanism. In this region, the ionic interaction between those particles and PE provides a stronger bonding than between the TiO_2 particles in oxide layers, where the bonding is predominately of the van der Waals type. Hence, the organic phase in multilayers imparts an increased difference in shear modulus, thus permitting the interfacial region to effectively counteract the propagation of the stress field induced by the applied load. This mechanism is corroborated by recent nanoindentation studies of hybrid thin films composed of SiO_2 particles in a polymer matrix, which clearly demonstrate the importance of interfacial bonding for enhancing the hardness of the inorganic/organic composite material [2005 MBR].

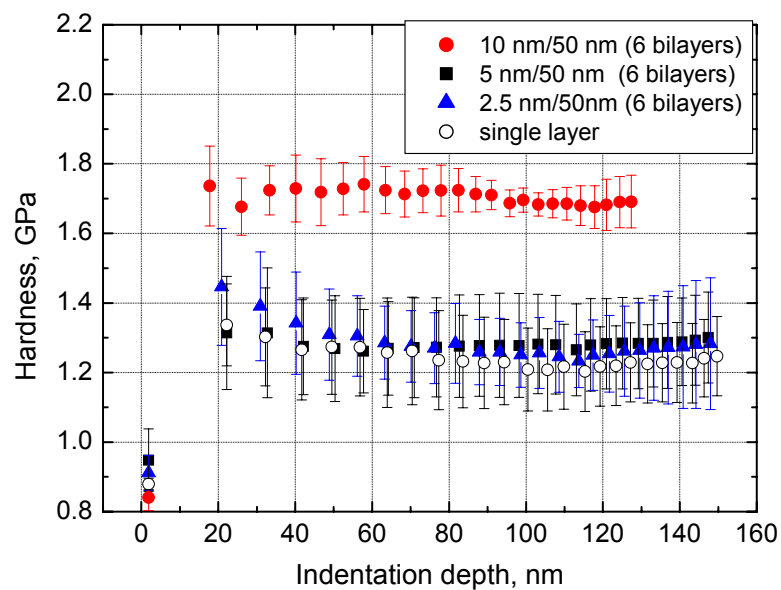
4.5.3. Influence of the organic/inorganic ratio on the mechanical properties of PE/TiO₂ multilayer films

In the last chapter it was shown that the presence of the organic phase in the multilayer structure enhances the mechanical performances of TiO₂ films. In further investigations, multilayer films with variable organic/inorganic thickness ratios were synthesized in order to investigate the influence of this ratio on the mechanical properties of PE/TiO₂ multilayer films.

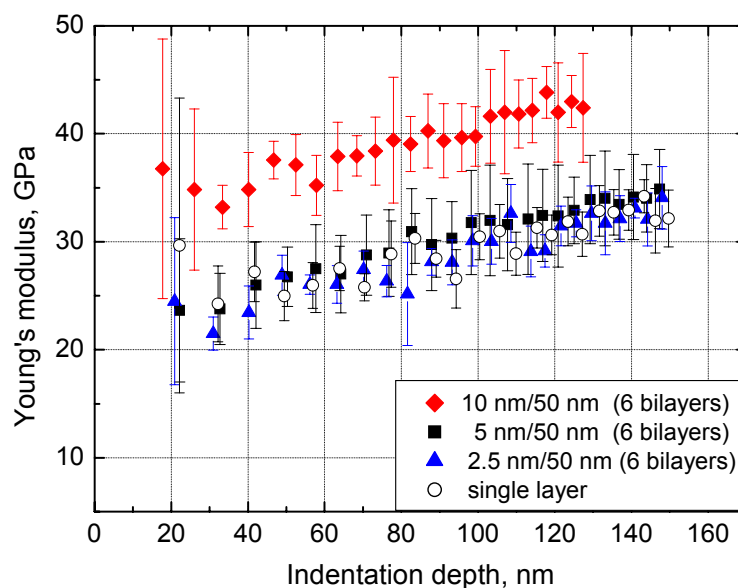
The investigations have been performed on multilayer films with six PE/TiO₂ couples. The film thickness of individual TiO₂ layer has been fixed at around 50 nm, whereas the thickness of the individual organic PE layer was varied by changing the number of cationic/anionic couples, according to the linear relationship between the layer thickness and the number of deposition cycles (Fig. 4.14 and 4.15). With the thickness of organic phase of about 10, 5 and 2 nm, the total thickness of multilayer films is in the range from 300-350 nm. The surface roughness of the films, determined by AFM, is about 20 nm.

Fig. 4.46 plots the extracted hardness and Young's modulus of PE/TiO₂ multilayer films with different ratio of organic and inorganic phase. The nanoindentation data were evaluated in the indentation depth range 20 – 60 nm, as it was explained before.

Evaluations of the nanoindentation data give values of ~1.7 GPa for the hardness of the (PE/TiO₂)₆ multilayer film with an organic/inorganic ratio 10 nm/50 nm. These results are comparable to the hardness values of the (PE/TiO₂)₃ film with the same organic/inorganic ratio of 25 nm/125 nm (Fig. 4.45). In contrast, the hardness values of films with an organic/inorganic ratio of 5 nm/50 nm and 2.5 nm/50 nm (~1.3 GPa) approach the hardness values of the single layer TiO₂ film. The Young's modulus of the (PE/TiO₂)₆ multilayer film with an organic/inorganic ratio 10 nm/50 nm is ~35 GPa which is higher than the one of the (PE/TiO₂)₃ film with the organic/inorganic ratio of 25 nm/125 nm (~30 GPa). A decrease in the thickness of the organic phase in the composite film from the thickness of 10 to 5 and 2.5 nm also decreases the values of the Young's modulus to the values of the single-layer film.



a)



b)

Fig. 4.46 Hardness (a) and Young's modulus (b) as a function of the indentation depth calculated from the nanoindentation data obtained from a TiO_2 single layers and $(\text{PE}/\text{TiO}_2)_6$ multilayer film with different organic/inorganic thickness ratio; the PE layers consist of two cationic/anionic couples $((\text{PEI}/\text{PSS})(\text{PAH}/\text{PSS}))$, 10 nm), where PSS and PAH were deposited from salt solution (0.5 M MnCl_2 for deposition of PSS and 1 M NaCl for deposition of PAH) or one cationic/anionic couple $((\text{PEI}/\text{PSS}))$, 5 nm), where PSS was deposited from salt solution (0.5 M MnCl_2) or one cationic/anionic couple $((\text{PEI}/\text{PSS}))$, 2.5 nm), where PSS was deposited from salt-free solution; the TiO_2 films were deposited by the SD from an aqueous solution of 10 mM $\text{Ti}(\text{O}_2)^{2+}$ and 45 mM HCl at 60°C for 1x2 h, with thickness of 50 nm

The increased mechanical performances of the composite with increasing thickness of the organic layer can be explained by an increasing homogeneity of the distribution of the polymer interlayers.

The STEM cross-section images of ~ 350 nm thick multilayer film consist of six PE/TiO₂ couples and an organic/inorganic ratio 10 nm/50 nm, are presented in Fig. 4.47 a. The STEM images presented in Fig. 4.47 b reveal the presence of homogeneous and continuous PE interlayers, which completely cover the TiO₂ surface, with the thickness of about 10 nm.

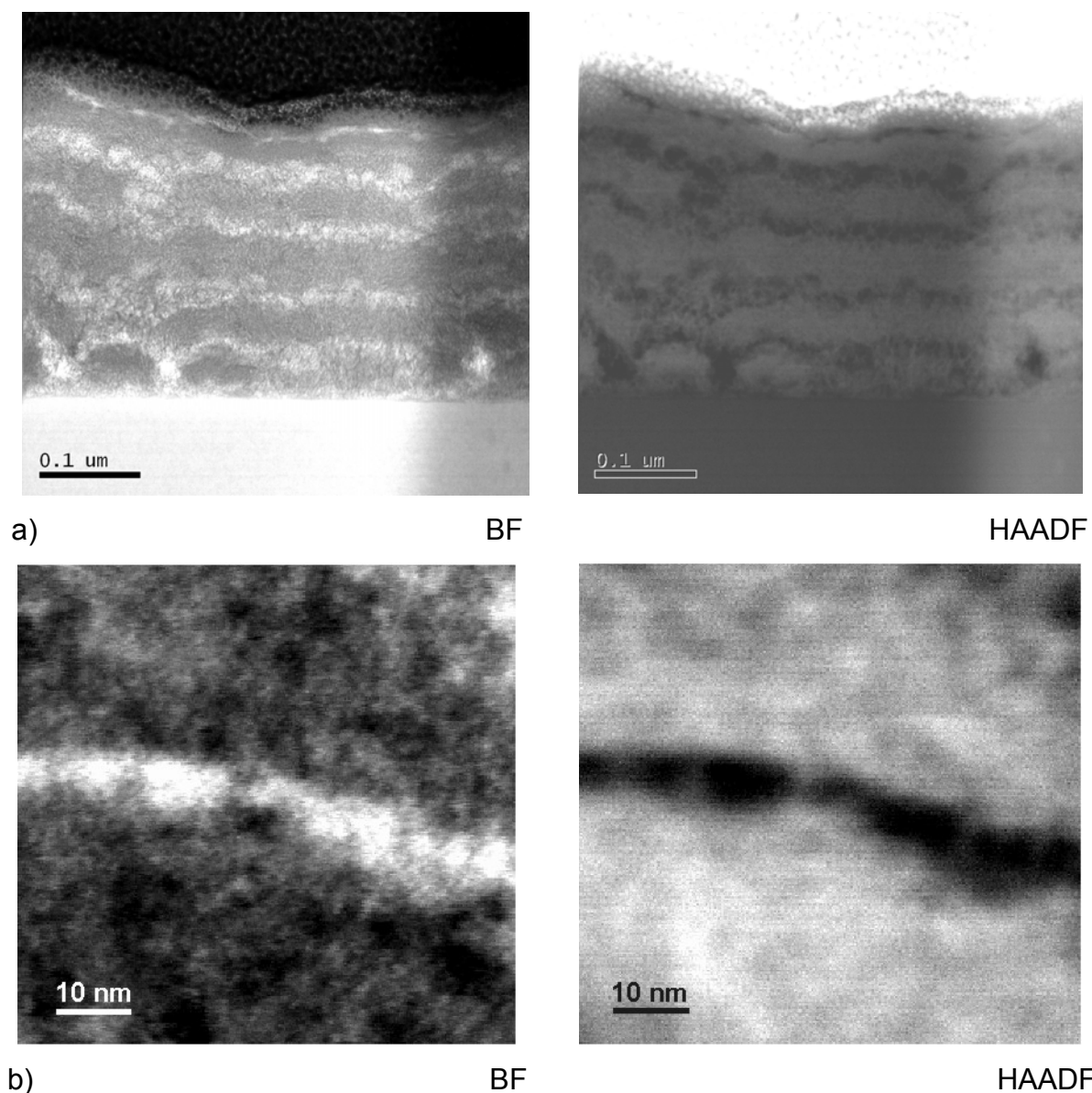


Fig. 4.47 STEM BF and HAADF images of cross-sectional TEM specimen of Si/(PE/TiO₂)₆ multilayer film with an organic/inorganic thickness ratio 10 nm/50 nm: a) the whole multilayer film and b) higher magnification of the PE layers; the PE layers consist of two cationic/anionic couples ((PEI/PSS)(PAH/PSS)); PSS and PAH were deposited from salt solution (0.5 M MnCl₂ for deposition of PSS and 1 M NaCl for deposition of PAH); the TiO₂ films were deposited by the SD from an aqueous solution of 10 mM Ti(O₂)²⁺ and 45 mM HCl at 60°C for 1x2 h.

By contrast, due to the surface roughness of the TiO_2 layers, thinner PE interlayers (5 nm) are blurred and discontinuous, i.e. the coverage of the inorganic layer with polymer is not complete (Fig. 4.48 a HAADF image, arrow marks).

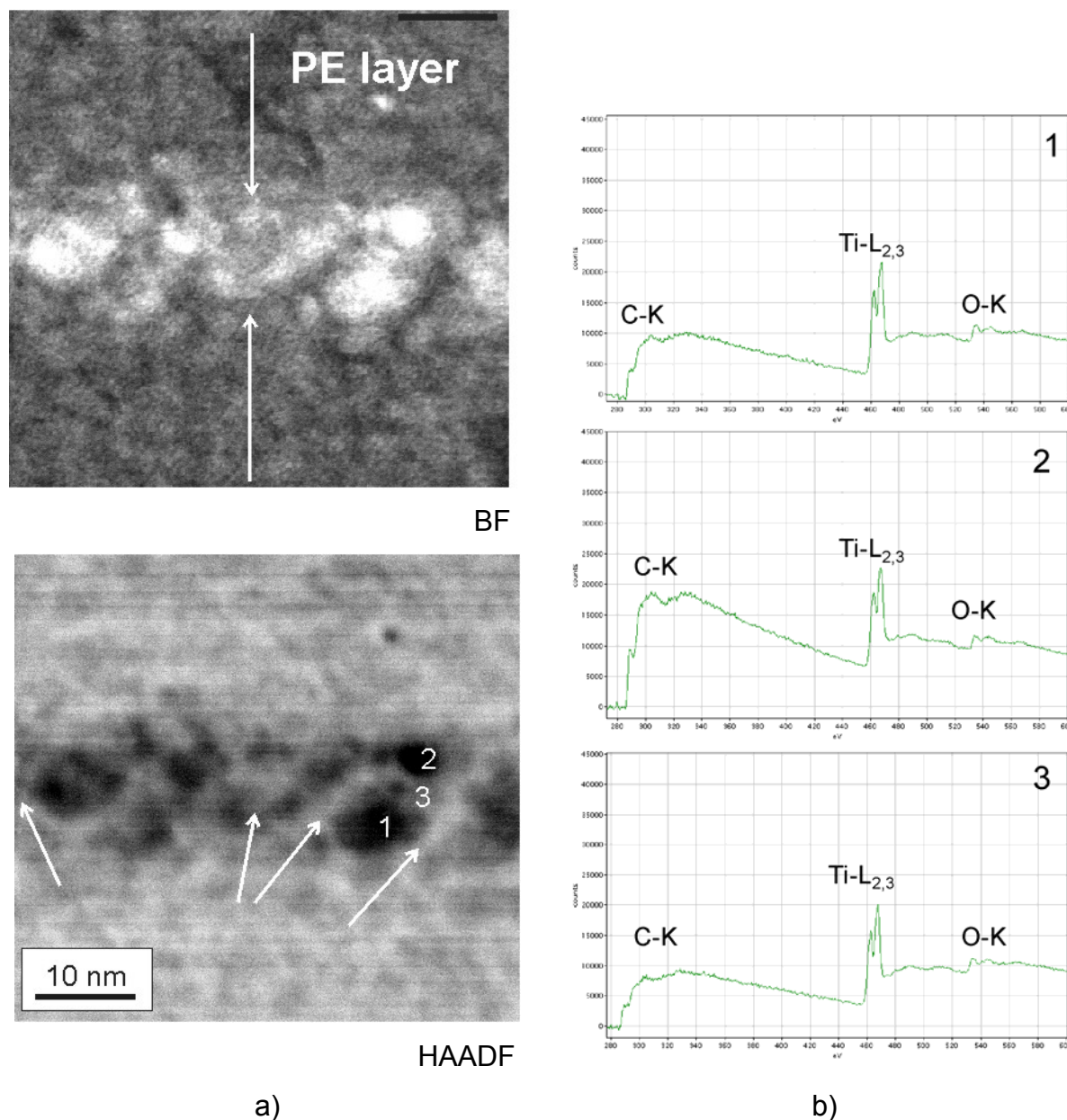


Fig. 4. 48 a) STEM BF and HAADF images of cross-sectional TEM specimen of penetrated PE layer in $\text{Si}/(\text{PE}/\text{TiO}_2)_6$ multilayer film with an organic/inorganic thickness ratio 5 nm/50 nm; b) EEL spectra of C-K, Ti-L_{2,3} and O-K edges recorded in the PE layer; the PE layers consist of one cationic/anionic couple (PEI/PSS); PSS was deposited from salt solution (0.5 M MnCl_2); the TiO_2 films were deposited by the SD from an aqueous solution of 10 mM $\text{Ti}(\text{O}_2)^{2+}$ and 45 mM HCl at 60°C for 1x2 h

Also, from literature it is known [1996 KMö, 2000 KTij] that the permeability of PE multilayer films for ions or molecules decreases with increasing of PE layer thickness because the structure of the initial layers is different from that of the outer layers. The

loops and defects are larger near the surface and the outer layers are more loosely packed than the layers more far from the surface in the film bulk, so penetration into the PE layer near the film surface is higher than the penetration in the PE layer.

For the polymer layers of 5 nm thickness, TiO_2 particles are totally interpenetrated through the all volume of the organic phase, as it's shown in Fig. 4.48 a. This observation is revealed by the EEL spectra presented in Fig. 4.48 b. The spectra show the presence of the C-K edge, as well the presence of the Ti-L_{2,3} and O-K edges through the whole thickness of the PE layer.

Fully interpenetration of TiO_2 into the polymer and discontinuous organic phase lead to dismissing of the PE/ TiO_2 interface which is responsible for the hardening by difference in shear modulus between two phases. That results in weaker mechanical performances of PE/ TiO_2 multilayers with the thickness of the organic PE phase of 5 and 2.5 nm. Therefore, the homogeneity of the organic layers (which can be controlled by their thickness) i.e. the uniform internal composition of the multilayer film is a necessary factor for an improvement of the mechanical performances of the PE/ TiO_2 multilayer films.

The observed increase of the hardness with incorporation of polymer interlayers between TiO_2 layers indicates an enhancement of the strength of the multilayer film, since it's well known that hardness and strength of material are proportional, i.e. the hardness of material is a measure of its strength [2000 Ash]. Furthermore, it can be correlated with an enhancement of the strength of nacre which traces back to the composite organic/inorganic structure (chapter 2.1). Namely, it is shown (Tab. 2.1) that nacre exhibits about 10 time higher strength than monolithic CaCO_3 . Proteins, as the organic constituent of nacre, play an essential role in achieving and maintaining a high strength. Qualitatively, the protein matrix behaves like a soft wrap around the mineral platelets and protects them from the peak stresses caused by the external load and homogenizes the stress distribution within the composites, hence the strength increase.

It is shown that combining CBD for synthesis of inorganic layers and LbL deposition for the organic one yields nanocomposite films with nacre-like structure. In contrast to the structure of nacre, where the inorganic phase consists of crystalline CaCO_3 platelets, the inorganic phase of the PE/ TiO_2 multilayers is mainly amorphous. The bonding between TiO_2 particles in the film is predominately of van der Waals type. In

this case, the hardening effect is attributed, first to the difference in shear modulus of inorganic and organic interlayers and second to the formation of the composite organic/inorganic phase due to the interpenetration of TiO_2 particles into polymer layer, where the electrostatic interactions between these particles and the polymer provides stronger bonding than between TiO_2 particles in the oxide layer. The first mechanism can be correlated to the strengthening mechanism for mineral platelets and protein matrix in the structure of nacre, proposed by Gao (chapter 2.1, Fig. 2.5). Under applied stress, the load is mostly carried by the inorganic TiO_2 layers, like by mineral platelets, while the organic PE layers (like protein) transfer the load from one to the other TiO_2 layer by shear.

5. Literature

- [1959 Sau] G. Sauerbrey, *Physics*, **155** (1959), 206-222
- [1966 Ile] R. K. Iler, *J. Colloid Interface Sci.*, **21** (1966), 569-594
- [1969 NBS] *Natl. Bur. Stand. (U.S.)*, Monogr. 25, vol. 7, page 82 (1969)
- [1970 Koe] J. S. Koehler, *Phys. Rev. B*, **2** (1970), 547-551
- [1983 NSa] L. Netzer, J. Sagiv, *J. Am. Chem. Soc.*, **105** (1983), 674-676
- [1986 DNi] M. F. Doerner, W. D. Nix, *J. Mater. Res.*, **1** (1986), 601
- [1988 Man] S. Mann, *Nature*, **332** (1988), 119-124
- [1989 BSE] R. Brydson, H. Sauer, W. Engel, J. M. Thomas, E. Zeitler, N. Kosugi, H. Kuroda, *J. Phys.: Condens. Matter.*, **1** (1989), 797-812
- [1991 DKK] E. Dalas, J. K. Kallitsis, P. K. Koutsoukos, *Langmuir*, **7** (1991), 1822-1826
- [1992 DHS] G. Decher, J. D. Hong, J. Schmitt, *Thin Solid Films*, **210-211** (1992), 831-835
- [1992 HFL] A. H. Heuer, D. J. Fink, V. J. Laraia, J. L. Arias, P. D. Calvert, K. Kendall, G. L. Messing, J. Blackwell, P. C. Rieke, D. H. Thompson, A. P. Wheeler, A. Veis, A. I. Caplan, *Science*, **255** (1992), 1098-1105
- [1992 OPh] W. C. Oliver, G. M. Pharr, *J. Mater. Res.*, **7** (1992), 1564-1583
- [1993 LDM] Y. Lvov, G. Decher, H. Möhwald, *Langmuir*, **9** (1993), 484-486

- [1994 BRT] B. C. Bunker, P. C. Rieke, B. J. Tarasevich, A. A. Campbell, G. E. Fryxell, G. L. Graff, L. Song, J. Liu, J. W. Virden, G. L. McVay, *Science*, **264** (1994), 48-55
- [1994 DLS] G. Decher, Y. Lvov, J. Smith, *Thin Solid Films*, **244** (1994), 772-777
- [1994 ITa] K. Ito, K. Tamaru, *Solar Energy Mater. Solar Cells*, **35** (1994), 179-184
- [1995 FMe] J. H. Fendler, F. C. Meldrum, *Adv. Mater.*, **7** (1995), 607-632
- [1995 RLD] J. J. Ramsden, Y. M. Lvov, G. Decher, *Thin Solid Films*, **254** (1995), 246-251
- [1995 SAK] *Biomimetics: Design and processing of materials/edited by M. Saraikaya and I. Aksay*, Woodbory, New York, 1995
- [1995 SCD] H. Shin, R. J. Collins, M. R. De Guire, A. H. Heuer, C. N. Sukenik, *J. Mater. Res.*, **10** (1995), 692-698
- [1996 ATM] I. A. Aksay, M. Trau, S. Manne, I. Honma, N. Yao, L. Zhou, P. Fenter, P. M. Eisenberger, S. M. Gruner, *Science*, **273** (1996), 892-898
- [1996 CRi] P. Calvert, P. Rieke, *Chem. Mater.*, **8** (1996), 1715-1727
- [1996 Ege] R. F. Egerton, *Electron Energy-Loss Spectroscopy in the Electronic Microscope*, Plenum Press, New York, 1996
- [1996 HSF] N. G. Hoogeveen, M. A. Stuart, G. J. Fleer, *Langmuir*, **12** (1996), 3675-3681
- [1996 INa] K. Ito, K. Nakamura, *Thin Solid Films*, **286** (1996), 35-36
- [1996 LAO] Y. Lvov, K. Ariga, M. Onda, I. Ichinose, T. Kunitake, *Colloids and Surfaces A*, **146** (1996), 337-346

- [1996 SMD] G. B. Sukhorukov, H. Möhwald, G. Decher, Y. M. Lvov, *Thin Solid Films*, **284-285** (1996), 220-223
- [1996 TRL] B. J. Tarasevich, P. C. Rieke, J. Liu, *Chem. Mater.*, **8** (1996), 292-300
- [1996 VVI] R. P. Vinci, J. J. Vlassak, *Annu. Rev. Mat. Sci.*, **26** (1996), 431-462
- [1996 WCa] D. B. Williams, C. B. Carter, *Transmission electron microscopy; A Textbook for Materials Science*, Plenum Press, New York, 1996
- [1997 ADe] M. Agarwal, M. R. DeGuire, A. H. Heuer, *Appl. Phys. Lett.*, **71** (1997), 891-893
- [1997 ADH] M. Agarwal, M. R. De Guire, A. H. Heuer, *J. Am. Ceram. Soc.*, **80** (1997), 2967-2981
- [1997 CMc] W. Chen, T. J. McCarthy, *Macromolecules*, **30** (1997), 78-96
- [1997 CNF] F. Caruso, K. Niikura, D. Neil Furlong, Y. Okahata, *Langmuir*, **13** (1997), 3422-3426
- [1997 Dec] G. Decher, *Science*, **277** (1997), 1232-1237
- [1997 Fra] L. F. Francis, *Mater. Manufacturing Proc.*, **12** (1997), 963
- [1997 KHT] N. A. Kotov, T. Haratzi, L. Turi, G. Zavala, R. e. Geer, I. Dekany, J. H. Fendler, *J. Am. Chem. Soc.*, **119** (1997), 6821-6832
- [1997 Nix] W. D. Nix, *Mater. Sci. Eng A*, **234-236** (1997), 37-44
- [1997 LAO] Y. Lvov, K. Ariga, M. Onda, I. Ichinoze, T. Kumitake, *Langmuir*, **13** (1997), 6195-6203

- [1997 OLA] M. Onda, Y. Lvov, K. Ariga, T. Kunitake, *Jpn. J. Appl. Phys.*, **36** (1997), L 1608-L 1611
- [1998 LFL] M. Lütt, M. R. Fizsimmons, D. Q. Li, *J. Phys. Chem. B*, **102** (1998), 400-405
- [1998 LLF] D. Q. Li, M. Lütt, M. R. Fizsimmons, R. Synowicki, M. E. Hawley, G. W. Brown, *J. Am. Chem. Soc.*, **120** (1998), 8797-8804
- [1998 OMc] P. O'Brien, J. McAleese, *J. Mat. Chem.*, **8** (1998), 2309-2314
- [1998 SAD] H. Shin, M. Agarwal, M. R. De Guire, A. H. Heuer, *Acta Mater.*, **46** (1998), 801-815
- [1998 YSR] D. Yoo, S. S. Shiratori, M. F. Rubner, *Macromolecules*, **31** (1998), 4309-4318
- [1999 Blm] J. Brandrup, E. Immergut (Eds.), *Polymer Handbook*, Wiley-Interscience, New York, 1999, Part 5
- [1999 FJW] A. Fischer, F. C. Jentoft, G. Weinberg, R. Schlögl, T. P. Niesen, J. Bill, F. Aldinger, M. R. De Guire, M. Rühle, *J. Mater. Res.*, **14** (1999), 3725-3733
- [1999 KFJ] L. Kolarik, D. F. Furlong, H. Joy, C. Struijk, R. Rowe, *Langmuir*, **15** (1999), 8265-8275
- [1999 KSS] [1999 KSS] K. Koumoto, S. Seo, W. S. Seo, W. J. Dressick, *Chem. Mater*, **11** (1999), 2305-2309
- [1999 LAO] Y. Lvov, K. Ariga, M. Onda, I. Ichinose, T. Kunitake, *Colloids Surf. A*, **146** (1999), 337-346

- [1999 SEW] S. Schwarz, K. J. Eichorn, E. Wischerhoff, A. Laschewsky, *Colloids Surf. A*, **159** (1999), 491-501
- [1999 SIH] K. Shimazu, H. Imai, H. Hirashima, *Thin Solid Films*, **351** (1999), 220-224
- [2000 Ash] M. F. Ashby, *Materials selection in mechanical design*, Butterworth-Heinemann, Oxford, 2000
- [2000 BJL] P. Bertrand, A. Jonas, A. Laschewsky, R. Legras, *Macromol. Rapid Commun.*, **21** (2000), 319-348
- [2000 BKA] A. Baba, F. Kaneko, R. C. Advincula, *Colloids and Surf. A*, **173** (2000), 39-49
- [2000 BMT] A. Bendavid, P. J. Martin, H. Takikawa, *Thin Solid Films*, **360** (2000), 241-249
- [2000 JFr] I. Jäger, P. Fratzl, *Biophys. J.*, **79** (2000), 1737-1746
- [2000 Jol] J. P. Jolivet, *Metal Oxides Chemistry and Synthesis*, John Wiley, New York, 2000
- [2000 KSB] S. Kamat, X. Su, R. Ballarini, A. H. Heuer, *Nature*, **405** (2000), 1036-1040
- [2000 KTj] L. Krasemann, B. Tieke, *Langmuir*, **16** (2000), 287-290
- [2000 MLo] R. S. Mane, C. D. Lokhande, *Mater. Chem. Phys.*, **65** (2000), 1-20
- [2000 MMM] R. Menig, M. H. Meyers, M. A. Meyers, K. S. Vecchio, *Acta Mater.*, **48** (2000), 2383-2398
- [2000 OBJ] A. O. Olofinjana, J. M. Bell, A. K. Jämting, *Wear*, **241** (2000), 174-179

- [2000 PKN] B. Pejova, T. Kocareva, M. Najdoski, I. Grozdenov, *Appl. Surf. Sci.*, **165** (2000), 271-278
- [2000 SLS] R. Steitz, V. Leiner, R. Siebrecht, R. v: Klitzing, *Colloids and Surf. A: Physicochem. Eng. Aspects*, **163** (2000), 63-70
- [2000 SDe] S. Supothina, M. R. De Guire, *Thin Solid Films*, **371** (2000), 1-9
- [2000 SWC] S. A. Syed Asif, K. J. Wahl, R. J. Colton, *J. Mater. Res.*, **15** (2000), 546-553
- [2000 WLL] J. Wang, W. Z. Li, H. D. Li, B. Shi, J. B. Luo, *Thin Solid Films*, **366** (2000), 117-120
- [2000 ZSQ] T. Y. Zhang, Y. J. Su, C. F. Qiu, M. H. Zhao, L. Q. Chen, *Acta Materialia*, **48** (2000), 2843
- [2001 IOS] T. Ito, Y. Okayama, S. Shiratori, *Thin Solid Films*, **393** (2001), 138-142
- [2001 Mit] D. B. Mitzi, *Chem. Mater.*, **13** (2001), 3283-3298
- [2001 MSI] Y. Masuda, T. Sugiyama, H. Lin, W. S. Seo, K. Koumoto, *Thin Solid Films*, **382** (2001), 153-157
- [2001 NBA] T. P. Niesen, J. Bill, F. Aldinger, *Chem. Mater.*, **13** (2001), 1552-1559
- [2001 NDe] T. P. Niesen, M. R. De Guire, *J. Electroceramics*, **6** (2001), 169-207
- [2001 SET] T. Sasaki, Y. Ebina, T. Tanaka, M. Harada, M. Watanaka, *Chem. Mater.*, **13** (2001), 4661-4667
- [2001 WZh] M. Wang, L. Zhang, *J. Mater. Res.*, **16** (2001), 765-773

- [2002 BHF] J. Bill, R. C. Hoffmann, T. M. Fuchs, F. Aldinger, *Z. Metallkd*, **93** (2002), 478-489
- [2002 CSF] H. Cölfen, H. Schnablegger, A Fischer, F. C. Jentoft, G. Weinberg, R. Schögl, *Langmuir*, **18** (2002), 3500-3509
- [2002 FHN] T. M. Fuchs, R. C. Hoffmann, T. P. Niesen, H. Tew, J. Bill, F. Aldinger, *J. Mater. Chem.*, **12** (2002), 1597-1601
- [2002 MJY] Y. Masuda, Y. Jinbo, T. Yonezawa, K. Koumoto, *Chem. Mater.*, **14** (2002), 1236-1241
- [2002 MOG] M. Manson, S. Ogueta, P. Garcia, J. Perez-Riguero, C. Jimenez, J. M. Martinez-Duart, M. Langlet, **23** (2002), 349-356
- [2002 MRL] E. Martirnez, J. Romero, A. Lousa, J. Esteve, *J. Phys. D*, **35** (2002), 1880-1886
- [2002 PCI] E. Poptoshev, P. M. Claesson, *Langmuir*, **18** (2002), 2590-2594
- [2002 PSS] H. Pizem, C. N. Sukenik, U. Sampathkumaran, A. K. McIlwain, M. R. De Guire, *Chem. Mater.*, **14** (2002), 2476-2485
- [2002 PSS] H. Pizem, C. N. Sukenik, U. Sampathkumaran, A. K. McIlwain, M. R. De Guire, *Chem. Mater.*, **14** (2002), 2476-2485
- [2002 RSJ] V. V. Rdatis, D. S. Su, F. C. Jentoft, R. Schögl, *Philosophical Magazine A*, **82** (2002), 2825-2839
- [2002 TLS] Y. Tang, Y. Liu, U. Sampathkumarau. M. Z. Hui, R. Wang, M. R. de Guire, *Solid State Ionics*, **15** (2002), 69-78
- [2002 YIm] S. Yamabi, H. Imai, *Chem. Mater.*, **14** (2002), 609-614

- [2003 GJJ] H. Gao, B. Ji, I. Jäger, E. Artz, P. Fratzl, *Proc. Natl. Acad. Sci. USA*, **100** (2003), 5597-5600
- [2003 HJB] R. C. Hoffmann, S. Jia, J. C. Bartolome, T. M. Fuchs, J. Bill, F. Aldinger, *J. Europ. Ceram. Soc.*, **23** (2003), 2119-2123
- [2003 Mit] C. Mitterbauer, *Ph.D. thesis*, Graz, 2003
- [2003 MKP] A. A. Mamedov, N. A. Kotov, M. Prato, G. M. Guld, J. P. Wicksteel, A. Hirsch, *Nature Materials*, **1** (2002), 190-194
- [2003 MTS] Y. Maehara, S. Takenaka, K. Shimizu, M. Yoshikawa, S. Shiratori, *Thin Solid Films*, **438-439** (2003), 65-69
- [2003 OHo] H. Okudera, A. Hozumi, *Thin Solid Films*, **434** (2003), 62-68
- [2003 SDH] S. Supothina, M. R. De Guire, A. H. Heuer, *J. Am. Ceram. Soc.*, **86** (2003), 2074-2081
- [2003 THa] H. Tokuhisa, P. T. Hammond, *Adv. Funct. Mater.*, **13** (2003), 831-838
- [2003 TKM] Z. Tang, N. A. Kotov, S. Magonov, B. Ozturk, *Nature Materials*, **2** (2003), 413-418
- [2003 YYC] J. Yu, H. Yu, B. Cheng, X. Zhao, J. C. Yu, W. Ho., *J. Phys. Chem. B*, **107** (2003), 13871-13879
- [2004 CLR] S. Chowdhury, M. T. Laugier, I. Z. Rahman, M. Serantoni, *Surf. Coat. Technol.*, **177-178** (2004), 537-544
- [2004 CPW] B. Chen, X. Peng, J. G. Wang, X. Wu, *Ceram. Internat.*, **30** (2004), 2011-2014

- [2004 HJW] R. C. Hoffmann, L. P. H. Jeurgens, S. Wildhack, J. Bill, F. Aldinger, *Chem. Mater.*, **16** (2004), 4199-4201
- [2004 JGa] B. Ji, H. Gao, *J. Mech. Phys. Solids*, **52** (2004), 1963-1990
- [2004 KBB] S. O. Kucheyev, T. van Buuren, T. F. Baumann, J. H. Satcher, T. M. Willey, R. W. Meulenber, T. E. Felter, J. F. Poco, S. A. Gammon, L. J. Terinello, *Phys. Rev. B*, **69** (2004), 245102-245111
- [2004 KBK] S. H. Kim, Y. J. Baik, D. Kwon, *Surf. Coat. Technol.*, **187** (2004), 47-53
- [2004 OPh] W. C. Oliver, G. M. Pharr, *J. Mater. Res.*, **19** (2004), 3
- [2004 SSH] B. Schoeler, S. Sharpe, T. Alan Hatton, F. Caruso, *Langmuir*, **20** (2004), 2730-2738
- [2005 BQB] B. J. F. Bruet, H. J. Qi, M. C. Boyce, R. Panas, K. Tai, L. Frick, C. Ortiz, *J. Mater. Res.*, **20** (2005), 2400-2419
- [2005 GKo] Y. Gao, K. Koumoto, *Cryst. Growth and Design*, **5** (2005), 1983-2017
- [2005 HBW] R. C. Hoffmann, J. C. Bartolome, S. Wildhack, L. P. H. Jeurgens, J. Bill, F. Aldinger, *Thin Solid Films*, **478** (2005), 164-169
- [2005 Jia] S. Jia, *Ph.D thesis*, Stuttgart 2005
- [2005 May] G. Mayer, *Science*, **310** (2005), 1144-1147
- [2005 MBR] F. Mammeri, E. L. Bourhis, L. Rozes, C. Sanchez, *J. Mater. Chem.*, **15** (2005), 3787-3811
- [2005 Röh] J. Röhberg, *Diploma thesis*, Stuttgart 2005

CURRICULUM VITAE

Family name: Tucić
Given name: Aleksandar
Date of birth: April 19, 1971
Place of birth: Belgrade, Serbia
Nationality: Serbian
Family status: Single

Education:

1977 – 1985 Primary school, Belgrade
1985 – 1989 10. Gymnasium, Belgrade
1990 – 1997 Faculty of Technology and Metallurgy, University of Belgrade
Dipl. Eng. of Inorganic Chemical Technology
1997 – 2001 Center for Multidisciplinary Studies of University of Belgrade
M.Sc. in Materials Science
Masters Thesis: The Influence of Synthesis Parameters on
Tin(IV)oxide Thin Films Properties
2002 – now Studying for Ph.D in Max-Planck Institute for Metals Research
and University of Stuttgart, Stuttgart, Germany
Ph.D Thesis: Wet Chemical Synthesis and Characterization of
Organic/TiO₂ Multilayers

Working experience:

1997 – 2003 Institute of Technical Sciences of Serbian Academy of Sciences
and Arts, Belgrade
Research-assistant
2006 – now Center for Multidisciplinary Studies of University of Belgrade
Research – assistant

Papers published from this thesis:

Z. Burghard, A. Tucic, L. P. H. Jeurgens, R. C. Hoffmann, J. Bill, F. Aldinger,
Nanomechanical Properties of Bioinspired Organic-Inorganic Composite films,
Advanced Materials, **19** (2007), 970-974